Response of Anionic Lipid Bilayers to Ion-Mediated Annexin II Binding: An X-ray and Neutron Reflectometry Study

Kirstin Fritz

SIGILL·UNIVERSITAT·LUDOVIC·MAXIM

München 2011

Response of Anionic Lipid Bilayers to Ion-Mediated Annexin II Binding: An X-ray and Neutron Reflectometry Study

Kirstin Fritz

Dissertation
an dem Department für Physik
der Ludwig–Maximilians–Universität
München

vorgelegt von
Kirstin Fritz
aus Freiburg im Breisgau

München, den 20.4.2011

Erstgutachter: Priv.-Doz. Dr. Bert Nickel
Zweitgutachter: Prof. Dr. Dieter Braun
Tag der mündlichen Prüfung: 10.7.2014

Summary

Cell membranes consist of a variety of different lipids, showing a rich phase behavior dependent on the surrounding environment and the state of the cell. The structure and physical state of native membranes constantly change due to the binding and unbinding of proteins. Because of this plenitude of factors influencing the structure of cell membranes, a variety of model systems have been established. The basic membrane structure is a single lipid bilayer, which is modeled *in vitro* by a supported lipid bilayer (SLB) on a solid substrate. The self-assembly of a single phospholipid bilayer on hydrophilic solid interfaces is easily obtained by spontaneous fusion of neutral unilamellar vesicles. A remaining and salient challenge, however, is to resolve the substrate influences on vesicle spreading and the structural details of lipid bilayers. There is also still a need to resolve the influence of the substrate on vesicle spreading and the structural details of the obtained lipid bilayers. Such knowledge of underlying interactions is of critical importance in mixed systems containing charged lipids or proteins, where the behavior of a bilayer may be changed due to electrostatic repulsion between substrate and vesicles.

In this thesis, we develop a new method for forming negatively charged SLBs by vesicle spreading on silicon supports. Homogenous and fluid bilayers are formed up to a concentration of 50% negatively-charged lipid by carefully adjusting the buffer conditions inside the vesicle and in the surrounding solution. The influence of the substrate on the distribution of lipids in both bilayer leaflets is resolved with x-ray reflectivity. The use of a brominated lipid derivative reveals an accumulation of negatively charged lipids in the leaflet distal from the surface while the proximal leaflet consists of uncharged lipids. Calcium-containing buffer leads to a densification of the distal leaflet in bilayers containing negatively charged lipids, while the proximal leaflets remain unaffected. Uncharged bilayers do not change their lipid area upon adding calcium. Lipid diffusion is diminished in calcium buffer for negatively charged bilayers compared to neutral bilayers. This behavior is explained by obstructed diffusion, i.e., the formation of negatively charged lipid micro domains with a higher density than the surrounding bilayer matrix.

The protein family of Annexins participate in various cellular processes that occur at or within the lipid bilayer of a cell. Examples include linkages between membrane and cytoskeleton, exocytic and endocytic transport steps and the regulation of ion fluxes across membranes. It was shown that the binding of some Annexins causes the formation of plasma-membrane domains promoting Ca^{2+}-evoked exocytosis. The binding of a protein to a lipid bilayer may directly influence the membrane structure and fluidity through lipid rearrangement. However, due to a multilayered assembly of protein and bilayer, studies of the influence of protein binding on bilayer structure are rare. While common techniques are only able to resolve the surface of the overall structure, only few techniques allow for an disentanglement of mass density and conformation of multilayered structures. In this thesis, x-ray reflectivity reveals that Annexin II tetramer (Anx A2t) binds peripherally to the distal leaflet of the bilayer, leading to a densification of solely the distal leaflet. Careful decomposition of the obtained electron density profiles unveils a densification of about 20%, presumably due to an accumulation and subsequent domain formation of charged lipids underneath the protein. Complementary diffusion measurements reveal a decrease in lipid mobility after protein binding and thus confirm this structural change.

The arrangement of Anx A2t upon binding to a single bilayer is still under vivid discussion today. In this thesis, x-ray and neutron reflectivity measurements clarify the conformation of Anx A2t upon binding to a single lipid bilayer. Two Annexin monomers bind to the surface of the bilayer while a p11 protein resides on top acting as a hinge, facing the buffer solution. This structural arrangement together with the ability to densify only one leaflet of the bilayer provide new molecular insights into the functional role of Anx A2t in regulating vesicular trafficking and endosome fusion.

Zusammenfassung

Zellmembranen bestehen aus einer grossen Anzahl unterschiedlicher Lipide und Proteine, die das Phasenverhalten der Membran bestimmen. Abhängig von Zellzustand und ihrer Umgebung ändern sich die Komposition und damit die biophysikalischen Eigenschaften der Zellmembran. Die Bindung von einigen Proteinen der Annexinfamilie führt beispielsweise zu der Bildung von dichten Phospholipiddomänen, die die kalziumabhängige Endo- und Exozytose begünstigen. Um den Einfluss verschiedener Faktoren auf den Zustand komplexer Zellmembranen zu untersuchen, wurden verschiedene Modellsysteme entwickelt. Die Grundstruktur von Zellmembranen wird meist durch oberflächengebundene Lipiddoppelschichten modelliert, welche durch die Fusion von Lipid-Vesikeln erzeugt werden. Während sich Lipiddoppelschichten aus zwitterionischen Lipiden auf hydrophilen Oberflächen spontan bilden, ist bei Mischungen aus geladenen und ungeladenen Lipiden ein detailiertes Verständnis der Wechselwirkung zwischen Substrat und Vesikel erforderlich, um ein Spreiten zu erreichen.

In der vorliegenden Arbeit wurde eine neue Methode entwickelt, um negativ geladene Phospholipidmembranen auf Silziumoberflächen zu erzeugen. Durch eine genaue Abstimmung der Salzkonzentration in der Lösung und in den Vesikeln konnten homogene Membranen mit einem negativen Lipidanteil von bis zu 50% erzeugt werden. Mit Hilfe von Röntgenreflektivität und bromierten Lipiden konnte die Verteilung der Lipide zwischen beiden Membranschichten aufgelöst werden: Die substratnahe Membranschicht besteht nahezu vollständig aus ungeladenen Lipiden, während sich negativ geladenen Lipide in der substratfernen Membranschicht anreichern. Nach Kalziumzugabe erfolgt eine Verdichtung ausschliesslich der substratfernen Membranschicht, die zu einer Erniedrigung des Diffusionskoeffizienten fluoreszenzmarkierter Lipide führt. Beide Effekte können durch die Entstehung von kalziuminduzierten Mikrodomänen mit erhöhter Dichte erklärt werden.

Die Struktur und Fluidität von Zellmembranen kann auch durch die Bindung von Proteinen beeinflusst werden. Hierzu gibt es jedoch nur wenige Erkenntnisse, da die meisten Messverfahren nur die Oberfläche und nicht die interne Struktur von Systemen mit multiplen Schichten auflösen. Mit Röntgen- und Neutronenreflektivitätsmessungen können hingegen vertikale Dichteprofile erstellt werden, die eine unabhängige Bestimmung von Schichtdichte und -dicke erlauben. In der vorliegenden Arbeit wurde das Bindungsverhalten des Annexin II Tetramer Proteinkomplexes an oberflächengebundene Lipidmembranen mit Hilfe von Röntgen- und Neutronenreflektivität untersucht. Das Protein bindet periphär an negativ geladene Membranen und führt zu einer Verdichtung der proteinzuge-

wandten Membranschicht um ca. 20%. In Diffusionsmessungen mit fluoreszenzmarkierten Lipiden konnte eine weitere Verminderung der Diffusionskonstante nach Proteinbindung nachgewiesen werden. Diese Änderung der Diffusivität und die Verdichtung der Membran kann durch eine Anreicherung von negativen Lipiden unterhalb der Proteinkomplexe erklärt werden.

Neben des Einflusses der Proteinbindung auf die Struktur der Membran konnte die Bindungskonformation des Annexin II Tetramer Proteinkomplexes mit Hilfe von Röntgen- und Neutronenreflektivität geklärt werden: Zwei Annexin Monomere binden an die Oberfläche der Membran, während das p11 Protein in die Pufferlösung ragt. Durch diese Bindungsstruktur und die asymmetrische Verdichtung nur einer Membranschicht können wichtige molekulare Einsichten in die Funktionsweise des Proteins *in vivo*, während z. B. der Regulation des Vesikeltransportes oder der Endozytose gewonnen werden.

Contents

Chapter 1

Introduction

Cells are surrounded by phospholipid membranes protecting the cell from the outside world. At the same time the membrane guarantees the communication and exchange with the environment. Lipid bilayers, which form the structural backbone of membranes, divide the cell's interior into compartments, specific for different tasks of the cell's metabolism. Such compartments include the nucleus where genetic information is stored and the endoplasmatic reticulum where protein synthesis and modification takes place (see figure 1.1). Furthermore, vesicles and liposomes transport a certain set of biochemical substances from one compartment to another [1].

In nature, biomembranes consist of a variety of different lipids that are unevenly distributed among the two leaflets of the bilayer. Proteins constantly bind and unbind from the membrane and change its appearance, sugar moieties protrude from the cells surface and communicate with the cells environment (see figure 1.2 for an illustration).

Diffusion measurements of membrane-bound proteins have shown that the bilayer is not a homogenous fluid but inhabits small domains accomodating proteins for specific tasks [2]. Adhesion proteins like cadherin and certain neural adhesion molecules, for instance, specifically bind to domains that are enriched in sphingolipids and cholesterol, nutrient and growth factor receptors [3]. Ras proteins, which are involved in cell growth and differentiation, are another case in point [4, 5]. Upon activation these proteins are selectively concentrated in nanodomains, facilitating the formation of functional protein clusters. What remains unresolved, however, is whether the formation of these nanodomains is an intrinsic property of the lipid bilayer itself, or, whether the driving force is the binding and unbinding of proteins to certain lipids which are subsequently clustered into lipid domains. For example, the lateral redistribution of anionic and neutral lipids in the mitochondrial membrane is induced by cytochrome c [6]. Other examples for proteins that are involved in lateral redistribution in lipid bilayers are cardiotoxin II [7], certain Annexins [8, 9] and basic peptides [10].

On the other hand, single component bilayers already exhibit a rich phase behavior with multiple phase transitions that depend on the chemical composition of the bilayer lipids, the ionic nature of the surrounding media and on temperature [12, 13, 14]. In lipid mixtures, changes in ionic buffer conditions and temperature may lead to preferential

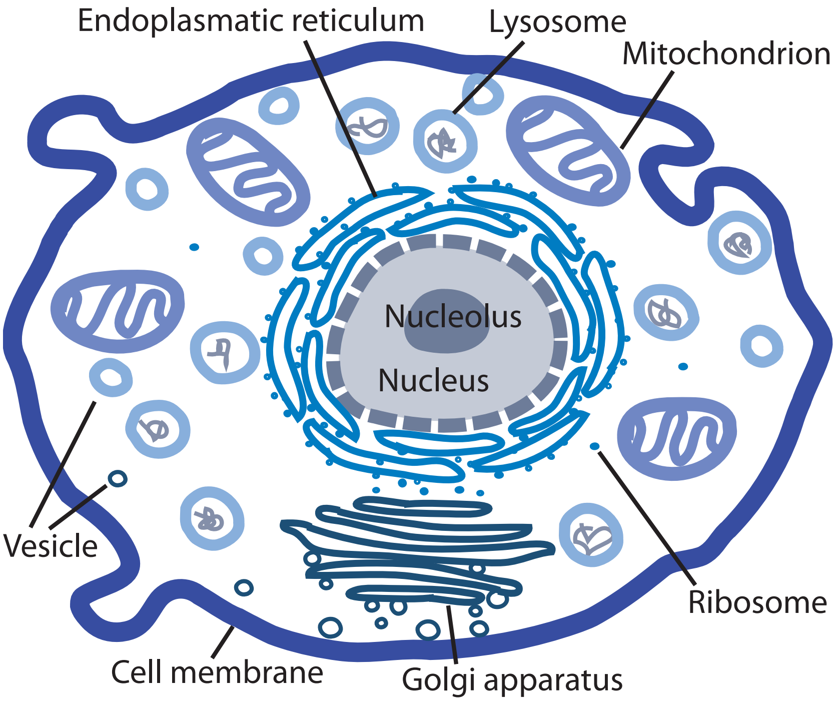

Figure 1.1: Sketch of an eucaryotic cell showing the organelles. Lipid bilayers separate these compartments from the cytoplasm.

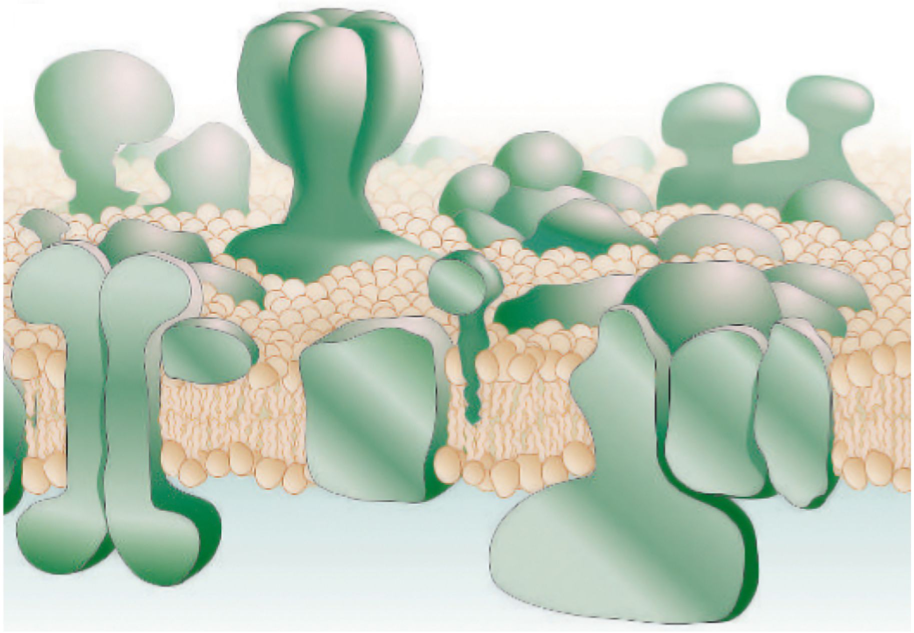

Figure 1.2: Sketch of a cell membrane revealing the complexity and inhomogeneity of a cell's bilayer. Proteins (*green*) are embedded into the bilayer or bind to its surface. Reprinted by permission from Macmillan Publishers Ltd: [Nature] ([11], copyright (2005)).

interactions between certain lipids leading to the formation of lipid domains. Here, we investigate the change in structure of negatively charged bilayers upon binding of Annexin II. The influence of buffer condition on the bilayer conformation is discriminated from structural changes that occur due to protein binding.

Because of the multitude of factors acting on membranes of living organisms, a variety of simplified model systems such as giant unilamellar vesicles (GUVs), lipid bilayer stacks, and black lipid membranes have been established. In particular, solid supported fluid lipid bilayers (SLBs) serve as an important model system for cell membranes. They allow for the application of surface sensitive techniques such as ellipsometry, quartz crystal microbalance or surface plasmon resonant spectroscopy in a highly controlled environment. The surface confines the geometry of the bilayer and allows for mechanical probing techniques like atomic force microscopy (AFM) [15]. However, the quality and appearance of SLBs not only depend on the lipid composition and the protein that binds to the bilayer, but also on chemical and physical properties of underlying solid supports [16, 17] and surrounding buffer solutions. A subtle balance between van der Waals, electrostatic, hydration, and steric forces determines the kinetics of vesicle adsorption and fusion to the underlying support as well as membrane spreading across the surface and its lipid distribution [18, 19]. On titanium and mica, for instance, negatively charged PS lipids are mainly trapped in the leaflet proximal to the surface [20, 21, 22], whereas on silicon oxide lipids labeled by negatively charged dyes tend to accumulate in the distal leaflet [23]. The formation of SLBs on silica is facilitated by the use of buffer solutions with divalent cations, while monovalent cations do not show the same effect [24]. The quality and phase behavior of the SLB is highly sensitive to the cleaning procedure of the surface, which makes it even more difficult to compare different experiments. For example, Seu *et al.* showed that the formation of bilayer domains containing cholesterol is highly dependent on the cleaning procedure used for the glass support [25].

The cell membrane leaflet facing the cytoplasm is negatively charged. Specific proteins bind to the negatively charged lipid entities, and perform their task in the cell's metabolism. Negatively charged surface supported bilayers serve to mimic this environment and provide a template for binding experiments. However, the overall forces between acidic negatively charged vesicles and negatively charged silicon surfaces show a repulsive behavior in pure water [24] and the spreading of such vesicles is hindered. One important part of this thesis deals with the influence of silicon surfaces on bilayers and the manipulation of the forces to form such bilayers in a controlled microfluidic environment.

As discussed before, the role of proteins in lipid domain formation is still under lively debate. One reason might be that common lab techniques like differential scanning calorimetry (DSC) and fluorescence resonance energy transfer (FRET) provide only indirect insights into molecular structures. They detect the change in bilayer conformation upon protein binding by resolving the change in phase transition temperature, or by comparing donor intensities of probes bound to different lipids [6]. Some effort was made to resolve the bilayer's domain structure by AFM measurements [15, 8], with the drawback that structures that are buried below the protein layer are experimentally not accessible. In contrast, neutron and x-ray scattering methods are able to resolve the inner structure of multilayers. The general method to resolve lateral structure in membranes with x-ray scattering, is to use bilayer stacks. However, Horton *et al.* showed for the first time that also a single bilayer and a single protein layer can be resolved by means of x-ray reflectivity [26].

Annexin A2 (Anx A2) is a Ca^{2+} binding protein which binds to acidic phospholipids. It is involved in many cellular regulatory processes, such as the regulation of vesicular trafficking, endosome fusion, insulin signal transduction and RNA binding [27, 28, 29, 30]. Anx A2 may exist in the cell in a monomeric version while a tetrameric version (Anx A2t) is needed to link adjacent bilayers. Controversy remains, however, about the organization of the tetramer when bound to a single membrane and the complex that is formed upon membrane-membrane connection. Former AFM measurements revealed an area of depletion of negatively charged lipids in the surrounding of bound Anx A2, leading to the assumption that the protein plays a role in the formation of phospholipid domains, by accumulating negatively charged lipids below itself [15]. In this thesis, x-ray reflectivity reveals the influence of protein binding in both bilayer leaflets separately, so that the influence of Anx A2t binding on the internal structure of each leaflet is resolved. Our results give an insight on the change in conformation, i.e curvature, of the bilayer upon Anx A2t binding in vivo (see figure 1.3*a*) for a summarizing illustration). A key objective in the present study is to reveal the actual structure of Anx A2t, bound to single bilayers (see figure 1.3*b*).

The structural reorganisation of lipid bilayers in varying buffer conditions and after

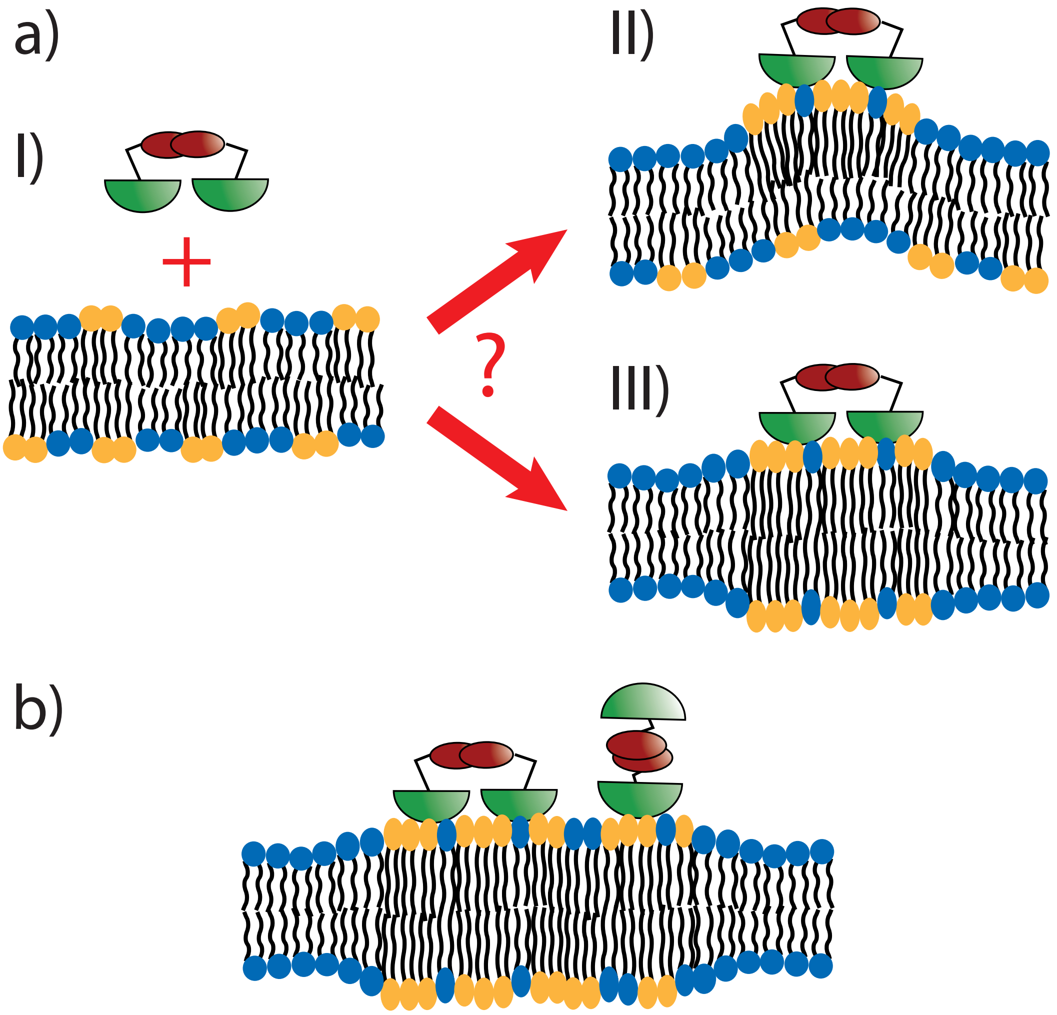

Figure 1.3: (*a*) Sketch of a phospholipid bilayer, containing negatively charged (*yellow*) and neutral (*blue*) lipids, before (*I*), and after Annexin II tetramer binding (*II* and *III*), illustrating the possible restructering of the bilayer. (*b*) Sketch of the possible Annexin II tetramer conformations.

protein binding is commonly accompanied by a change in lipid mobility. Measurements of phase separated bilayers , for instance, revealed different diffusion constants for lipid rafts and the surrounding matrix, as compared to single component bilayers [31, 32, 9]. Another example, is the binding of Annexin V forming assemblies on bilayers with negatively charged lipids in calcium containing buffers. PC lipids below such assemblies exhibit a diffusion constant that is a magnitude lower as compared to PC lipids that are in the bilayer matrix [9]. Since changes in bilayer mobility are thought to play an important role in the cell signaling cascades, diffusion measurements can provide important information about protein function in vivo. Therefore, in order to gain a deeper understanding about the influence of structural bilayer arrangements on lipid mobility, this study complements x-ray reflectivity measurements with diffusion measurements, before and after Anx A2t binding.

Chapter 2

Theoretical concepts and experimental methods

One aim of this work is to study the formation of lipid bilayers on silicon supports and to investigate the influence of the underlying support on the spreading of vesicles, the bilayers' phase behavior and lipid distribution. The following chapter describes the physical concepts and underlying forces that govern the formation and phase behavior of bilayers on surfaces. In section 2.2, a short overview of the main phases of lipid bilayers is given, followed by an introduction to the various theories that explain domain formation in lipid bilayers. A further aim of this work is to investigate the influence of protein binding on the state of each bilayer leaflet. Section 2.3 gives an introduction to today's view about the interplay between membrane-binding proteins and the bilayer. Here, a particular focus is laid on the binding of proteins to negatively charged lipids, which is the central binding mechanism of the Annexin family. In a following part concepts how proteins influence domain formation are explained. Since this work concentrates on a certain lipid binding protein, namely Annexin II, section 2.3.3 deals with the Annexins' protein family. Here, the structure of the Annexin family with a particular focus on Annexin II is presented that is followed by an introduction to the binding mechanism of the protein to negatively charged lipids. The lipid mobility within a bilayer may mirror changes in lateral structure. In section 2.4 the main theoretical concepts of diffusion within a bilayer are introduced, followed by an introduction to the main measurement methods. Since the main part of this work are structural investigation with x-ray and neutron reflectivity, both methods are introduced in section 2.5 and the experimental parameters described.

2.1 Forces between surfaces and lipid bilayers

In chapter 3.1 of this work the spreading of negatively charged lipid bilayers and the influence of the silicon support on the structure of such bilayers is investigated. To choose appropriate experimental conditions, for example, the buffer's salt concentration, type of salt and temperature, leading to the formation of bilayers, one has to be able to estimate the underlying physical forces. When a lipid vesicle or bilayer interacts with a surface in an aqueous environment, there are a number of forces that regulate the spreading of vesicles, the distribution of lipids among the bilayer leaflets and the distance of the bilayer to the surface. The most dominant forces involved in these interactions include van der Waals forces, electrostatic forces and hydration forces, as discussed in the following.

Van der Waals forces. Van der Waals forces are of electrostatic nature and are the result of various dipole-dipole interactions. For instance, the interaction between permanent dipoles (Keesom interaction), between permanent and induced dipoles (Debye interaction) and between two instantaneously induced dipoles (London interaction) all result in the same dependence of the potential $V_{vdw}(r_m)$ from the distance r_m of the molecules [33], i.e.,

$$V_{vdw}(r_m) = -\frac{V}{r_m^6}\,, \tag{2.1}$$

where V is a constant that depends on the type of interaction (Keesom, Debye or London) and on the particular molecules involved. For macroscopic particles and surfaces the interaction energies between all molecules are summed up, in the simplest approximation of nonretarded and additive interaction energies. The obtained potential is dependent on the geometry of the interacting bodies, and includes the so called Hamaker constant A, a material parameter that describes the resultant dipole moments.

$$A = \pi^2 V \rho_{A1} \rho_{A2}, \tag{2.2}$$

where ρ_{A1} and ρ_{A2} are the atomic densities of body 1 and body 2 respectively.

For a bilayer (medium 1) interacting in an aqueous solution (medium 2) with a surface (medium 3) the parameters of three different media have to be taken into account. The non retarded van der Waals forces per unit area are then approximated by [19],

$$F_{vdw}(z_s) = -\frac{A_{123}}{6\pi}\left(\frac{1}{z_s^3} - \frac{2}{(z_s+d_b)^3} + \frac{1}{(z_s+2d_b)^3}\right). \tag{2.3}$$

Here A_{123} is the Hamaker constant between medium 1, medium 2 and medium 3, z_s the distance between the bilayer and the surface and d_b is the bilayer thickness. For surface supported lipid bilayers in salt solutions the Hamaker constant is between 3-4$\times10^{-21}$ J [19]. The van der Waals energy per unit area E_{VWD} is calculated by

$$E_{VWD} = \int V_{vdw} dz_s = -\frac{A_{123}}{6\pi}\left(\frac{1}{2z_s^2} + \frac{1}{(z_s+d_b)^2} - \frac{1}{2(z_s+2d_b)^2}\right). \tag{2.4}$$

For condensed media this approach has been proven to be inaccurate and thus a macroscopic continuum approach was established. In this approach van der Waals forces depend on the difference of polarizability of the interacting media and the distance to each other [34]. The Hamakar constant between lipid bilayers is then calculated to be in the range of $10^{-21} - 10^{-20} J$ [35, 36] and thus in the same range as calculated by the nonretarded approximation.

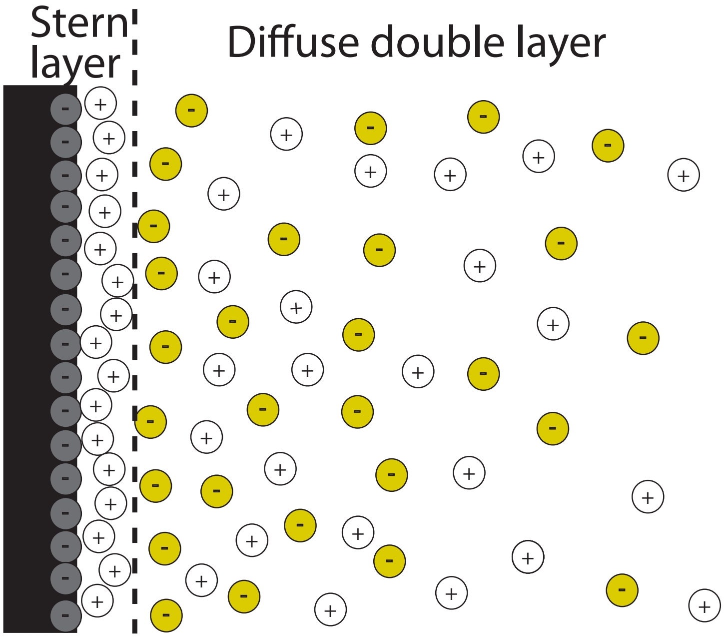

Figure 2.1: Cartoon of the Stern and diffuse double layer as evident at a surface with negative surface charges. Yellow circles represent negatively charged ions, white circles positively charged ions, grey circles represent surface charges. The dotted line represent the border of the Stern layer.

Electrostatic forces. Cell membranes, artificial bilayers as well as the surfaces they interact with, almost always carry charges in aqueous solutions, leading to long range electrostatic forces. These forces are thought to play the major role in the interaction of charged surfaces and charged bilayers as investigated in this work. The surface charges are balanced by an oppositely charged region of counterions. Two regions, shown in figure 2.1 may be distinguished: The so called Stern (or Helmholtz) layer consisting of ions that are bound to the surface and a second region, the so called diffuse electric double layer, consisting of ions that are aligned by the electric potential of the surface, while still being freely diffusible. The overall potential Ψ_E is given by

$$\Psi_E = \Psi_S + \Psi\,, \tag{2.5}$$

where Ψ_S is the potential of the Stern layer and Ψ is the potential of the diffuse double layer. The potential of the Stern layer can be modeled as a capacitor by

$$\Psi_S = \frac{\sigma d_S}{\varepsilon_S \varepsilon_0}\,. \tag{2.6}$$

Here σ is the surface charge density, d_S the thickness of the Stern layer, ε_0 the vacuum permittivity and ε_S the permittivity of the Stern layer.

The potential of the diffuse electric double layer of a surface in a solution that only contains counterions is decribed by the Poisson Boltzmann equation

$$\frac{d^2\Psi(x)}{dx^2} = -\frac{vec_0}{\varepsilon\varepsilon_0} e^{\frac{-ve\Psi(x)}{kT}}\,, \tag{2.7}$$

where c_0 is the concentration of ions at the surface, ε_0 the permittivity of vacuum, ε the permittivity of the (bulk) buffer solution, k the Boltzmann constant, and T the temperature. In an electrolyte solution with ions of valency v the Boltzmann distribution for ions at a distance x is given by

$$c(x) = c_\infty e^{\frac{-ve\Psi(x)}{kT}}\,, \tag{2.8}$$

where $c(x)$ is the concentration of ions at distance x from the surface c_∞ is the concentration of ions in bulk solution, e the elementary charge and $\Psi(x)$ the potential at distance x. At the surface the concentration of ions is

$$c_0 = c_\infty e^{\frac{-ve\Psi_0}{kT}}\,, \tag{2.9}$$

with Ψ_0 the surface potential. In biological systems, there is a variety of ions i with different valency which may lead to a redistribution of ions around charged surfaces and thus to a specific behavior of the system. The concentration of ions of different valency at a surface with charge density σ is given by the Graham equation [37]

$$\sum_i c_{0i} = \sum_i c_{\infty i} + \frac{\sigma^2}{2\varepsilon\varepsilon_0 kT} \tag{2.10}$$

$$\sigma^2 = 2\varepsilon\varepsilon_0 kT(\sum_i c_{0i} - \sum_i c_{\infty i})\,, \tag{2.11}$$

where ε is the permittivity of the buffer, ε_0 the permittivity of vacuum, c_{0i} the concentration of ion i at the surface and $c_{\infty i}$ the concentration of ion i in bulk solution. With Eq. (2.10) it is possible to find the relation between surface charge density σ and the surface potential Ψ_0. For a 1:1 electrolyte such as NaCl the relation between surface potential and surface charge density is given by

$$\frac{\sigma^2}{2\varepsilon\varepsilon_0 kT} = [Na^+]e^{\frac{-e\Psi_0}{kT}} + [Cl^-]e^{\frac{e\Psi_0}{kT}} - [Na^+] - [Cl^-]\,. \tag{2.12}$$

With $[\mathrm{Na}^+] = [\mathrm{Cl}^-]$ Eq. (2.12) is solved for the surface potential Ψ_0 to obtain [38]

$$\psi_0 = \frac{2kT}{e}\mathrm{arcsinh}\left(\frac{\sigma}{\sqrt{8\varepsilon\varepsilon_0[NaCl]}}\right)\,. \tag{2.13}$$

For low potentials ψ_0 the charge density σ can be written as

$$\sigma = \varepsilon\varepsilon_0\kappa\psi_0\,, \tag{2.14}$$

where

$$\kappa = \sqrt{\frac{e^2 \sum_i c_{\infty i} v_i^2}{\varepsilon\varepsilon_0 kT}}, \tag{2.15}$$

describes the inverse Debye length $1/\kappa$. The potential gradient $\frac{d\Psi}{dx}$ at distance x is determined through

$$\sum_i \varrho_{xi} = \sum_i c_{\infty i} + \frac{\varepsilon\varepsilon_0}{2kT}\left(\frac{d\Psi}{dx}\right)^2, \tag{2.16}$$

which is solved to gain the Gouy Chapman equation [38], that is,

$$\psi_x \approx \frac{4kT}{e}\tanh\left(\frac{e\Psi_0}{4kT}\right)e^{-\kappa x}. \tag{2.17}$$

In this work mixtures of zwitterionic and negatively charged lipids are spread on silicon with the aid of osmotic pressure (see section 3.1). During this process the salt condition of the buffer solution changes dramatically. In section 3.2 the structural changes in varying buffer conditions and the influence of salt condition on lipid mobility are investigated. Due to the negatively charged silicon support, electrostatic interactions are expected to be the main force dominating the behavior of the investigated bilayers and hence the Gouy Chapman theory will be used to estimate the potential in our experimental system.

Hydration forces. Experimental investigations of molecules interacting with a surface have shown that van der Waals and electrostatic forces do not explain the interaction of surfaces at small distances [39, 40, 41, 42]. Not only lipid bilayers show the described behavior, but also DNA and such diverse surfaces as silica surfaces, clays and minerals [43, 41, 44, 45]. The similar short range repulsion of such a variety of different surfaces led to the assumption that there is a common underlying origin. Furthermore, the obtained force distance curves for all these surfaces show the same exponential behavior [42, 46]

$$P(d_w) = P_0 e^{-d_w/\zeta}, \tag{2.18}$$

where P_0 is the hydration force in contact, ζ is the so called decay length and d_w the distance between the surfaces. The decay length ranges between 1 and 3 Å for lipids and varies upon surface termination and buffer conditions [47, 48]. A couple of experimental and theoretical studies have dealt with the origin of these force distance curves, however, the physical mechanism is still under debate [43, 49, 42, 46]. Leikin *et al.* postulate that the examined force mainly stems from the ordering of water around hydrophilic surfaces which has to be removed when such surfaces approach each other [45]. This idea is supported by Faraudo *et al.* who have shown with molecular dynamics simulations that the main part of the repulsive hydration force stems from the restructuring of water near the interface [42]. The investigation of interaction of DNA strands in salt solutions, revealed that the addition of divalent and polycationic salts leads to an attractive hydration force [50]. Strikingly, the decay length of the attractive hydration force is half of the repulsive, namely 1.5 Å

[50]. This behavior was explained by a complementary reorganization of water, through the absorbtion of multivalent counterions, compared to the organisation of water on the apposing surface. In the order parameter model the restructuring of water around polar groups is parametrized by a so called solvent order parameter. It predicts a repulsive pressure p_{rep} between two surfaces that disturb the oriental distribution of water, and thus the hydrogen bonding network water prefers. On the other hand if the surfaces structure the adjacent water in a complementary way, the hydrogen bonding network from one surface to the other is enforced, resulting in an attractive pressure p_{attr}. [51, 52, 45], i.e.

$$p_{rep} = \frac{C_{rep}}{\sinh^2(d_w/2\zeta_w)} \tag{2.19}$$

$$p_{attr} = -\frac{C_{attr}}{\cosh^2(d_w/2\zeta_w)}\,, \tag{2.20}$$

where C_{rep} and C_{attr} contain the solvent order parameter at each surface, d_w is the distance between the surfaces and ζ_w is the decay length of the restructering. The latter formula may describe the difference in decay length between PE and PC bilayers, attributed to an attractive hydration force between PE lipids [52], leading to a dehydration of such bilayers. Dehydration has also been observed with acidic phospholipids in buffers containing divalent ions [45, 53, 54].

In this work acidic phospholipids are used to form bilayers on silicon supports. To stabilize the bilayers a buffer containing calcium ions is used and the internal structure is investigated in section 3.2.3 with x-ray reflectivity. The above described theoretical concepts reveal that the short range interplay of bilayer and silicon support is highly dependent on hydration effects in buffers with different ion types and concentration.

2.2 Domain formation in lipid bilayers

Historically, the cells's surrounding bilayer was mainly considered as semi permeable barrier, necessary to maintain conditions that are chemically distinct from the environment. Communication between the two compartments was thought to occur by active transporters and ion channels. In this model the bilayer behaves laterally like a homogenous fluid mosaic without any lateral structure [55]. The discovery of so-called lipid rafts, that are dynamically changing small domains in the cell membrane, enriched in certain lipids and cholesterol, completely changed the picture of lateral homogeneity. Such domains are thought to provide a platform for the functioning of raft-associated proteins and lower the dimensionality of diffusion within the membrane such that the reaction time of certain biochemical processes is efficiently reduced [56, 57].

2.2.1 Lipids and lipid phases

The chemical structure of lipids determines their behavior in the bilayer and with that their tendency to form lipid domains. The chemical structure of the glycerophospholipids

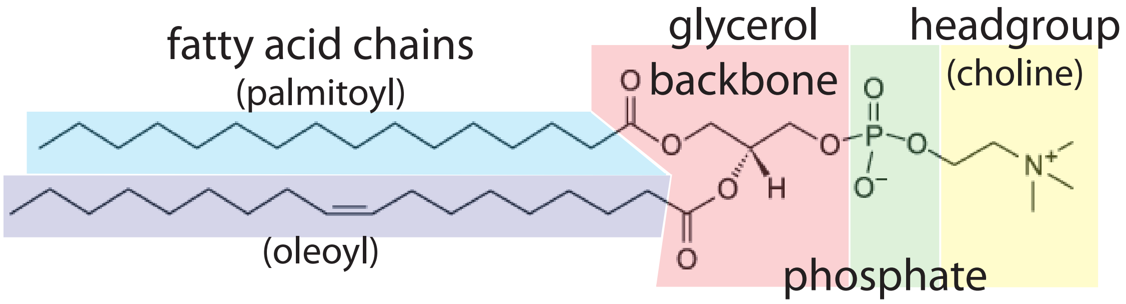

Figure 2.2: Sketch of the structure of a typical phospholipid. Shown are the hydrocarbon or fatty acid chains (palmitoyl, *light blue* and oleoyl, *light purple*), the glycerol backbone (*light red*) the phosphate group (*light green*), and the headgroup (choline, *light yellow*).

(phospholipid hereafter) is shown in figure 2.2. Two fatty acid chains are joined by an ester linkage to a glycerol core. The lipid head is attached by an ester linkage between the head's phosphate group and the glycerol core. The lipid chains are unbranched hydrocarbon chains that are either saturated or exhibit single and double bonds (unsaturated). Examples of fatty acids include palmitoyl, a fully saturated hydrocarbon chain, consisting of 16 carbon atoms (a so called 16:0 chain) and oleoyl exhibiting one double bond within its chain and consisting of 18 carbon atoms (also-called 18:1 chain). The phospholipid headgroups may either be charged, e.g., phosphatidylserine (PS) (figure 2.3*a*) or zwitterionic, e.g., phosphatidylcholine (PC) (figure 2.3*b*) and phosphatidylethanolamine (PE) (figure 2.3*c*) or may be modified by adding phosphate groups, e.g., phosphatidylinositol-bisphosphate (PIP2) (figure 2.3*d*).

Depending on the type of lipid, a bilayer consists of, it may undergo phase transitions at different temperatures T_m. For most phospholipids the low-temperature phase is the so-called subgel $\mathrm{L_c}$ phase, where the hydrocarbon chains exhibit a tilt and are highly ordered (see figure 2.4*a*). An increase in temperature leads to a phase transition to a lamellar gel phase, which is either the L_β phase (see figure 2.4*b*) for example, for phosphatidylethanolamines (PE), or the $\mathrm{L}_{\beta'}$ phase (see figure 2.4*c*) for example, for phosphatidylcholines (PC). Here, the bilayer exhibits a higher hydration and is still highly ordered but to a smaller degree than in the $\mathrm{L_c}$ phase. The hydrocarbon chains are arranged along the bilayer normal in the L_β phase while in the $\mathrm{L}_{\beta'}$ phase the chains are tilted. At higher temperature, the lipids undergo a trans-gauche isomerization of single carbon - carbon bonds leading to the L_α phase with disordered chains (see figure 2.4*e*). This phase is also called the liquid crystalline or fluid phase. The transition from the ordered gel phase to the disordered liquid crystalline phase occurs for some lipids in two steps. In a first step, the gel phase transforms into the rippled phase ($\mathrm{P}_{\beta'}$) (see figure 2.4*d*) followed by a conversion to the liquid crystalline phase [12].

A special phase is the so called liquid ordered phase (L_0) (see figure 2.5). It occurs in bilayers containing cholesterol and/or sphingolipids that are organized in lipid rafts. In

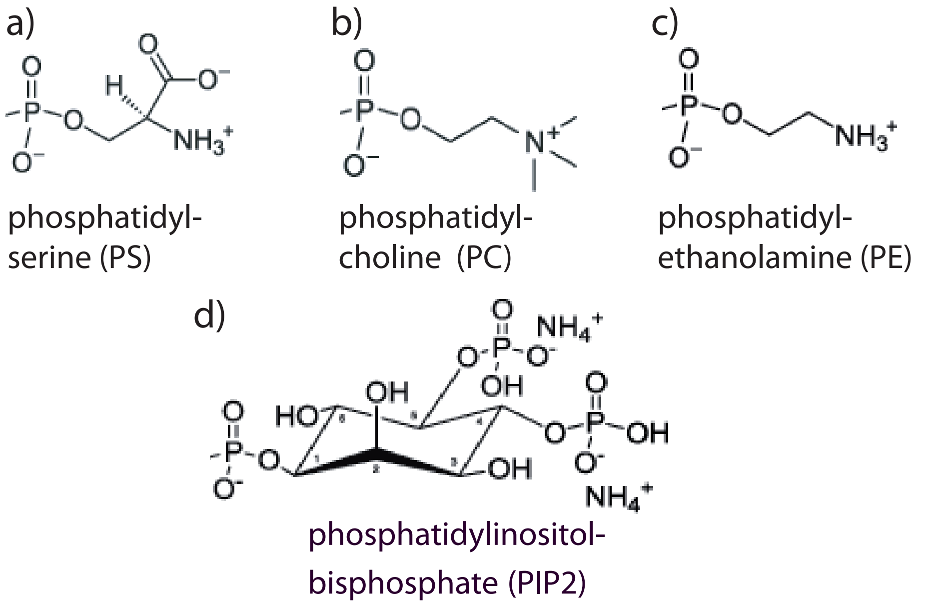

Figure 2.3: Structure of typical phospholipidheadgroups. Shown are phosphatidylserine (*a*), phosphatidylcholine (*b*), phosphatidyletholamine (*c*) and phosphatidylinositil-biphosphate (*d*).

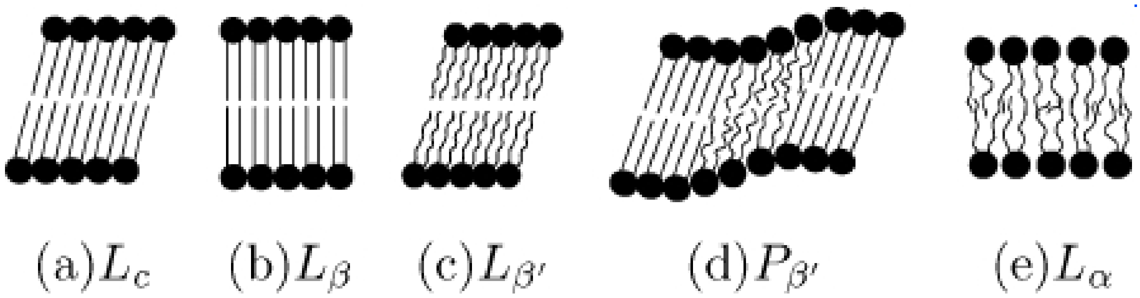
(a)L_c (b)L_β (c)$L_{\beta'}$ (d)$P_{\beta'}$ (e)L_α

Figure 2.4: Sketch of the phases of a phospholipid bilayer. Shown are the subgel phase (*a*), the untilted gel phase (*b*), the tilted gel phase (*c*), the ripple phase (*d*) and the liquid disordered phase (*e*). Reprinted with permission from [12]. Copyright 2005 American Chemical Society.

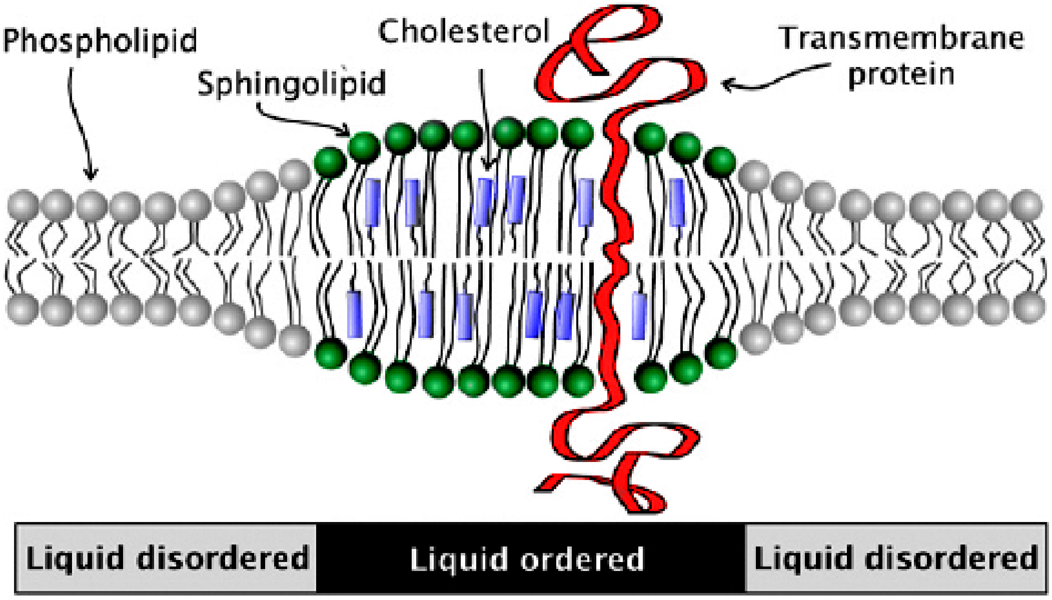

Figure 2.5: Sketch of a lipid raft. Cholesterol (*blue boxes*) is tightly associated with sphingolipids (*green headgroups*), leading to a tightly packed liquid ordered phase with an increased thickness as compared to the bilayer matrix (*grey headgroups*). Furthermore, proteins are specifically bound to the phase (*red ribbon*). [56] Reproduced by permission of The Royal Society of Chemistry.

the L_0 phase the lipids are in a stretched all-trans conformation with cholesterol serving as a molecular spacer, filling any voids between associated sphingolipids (see figure 2.5) [56]. This phase exhibits a fluidity that is about two times lower than the fluidity of the liquid disordered phase and thus may facilitate proteins to find their binding target residing in the lipid raft [56].

2.2.2 Mechanisms of domain formation

Mixtures of lipids may exhibit domain formation depending on the energy differences between distinct lipid/lipid interactions. These differences are described by the so-called unlike nearest neighbor interaction parameter (ω) that corresponds to the difference in interaction energy between lipids of a certain lipid species and the interaction of lipids of different species. The typical value of ω in mixed lipid systems is between -300 kcal/mol and 300 kcal/mol with $\omega < 0$ describing a situation of lipids favoring interactions between lipids of different species and $\omega > 0$ describing the situation of lipids favoring interactions between lipids of the same species. The parameter does not stand for a certain physical effect but rather includes all effects significant for nearest neighbor interaction. The underlying physical forces are for example, van der Waals forces, hydrogen bonds, the conformational entropy of acyl chains, hydrophobic interactions and electrostatic repulsion as apparent between charged lipids [13]. This may explain for example that in two component systems, containing lipids with higher and lower melting temperature, the solid and liquid disordered phase may exist at the same time, leading to the formation of solid domains in a fluid matrix due to the preferred interaction of lipids corresponding to the same phase [56]. Another example is the formation of lipid rafts due to a preferred interaction of cholesterol with sphingomyelin and ordered alkyl chains [13]. The addition of calcium to mixtures of zwitterionic PC lipids and negatively charged PS lipids may render the interaction of PS lipids with themselves favorable, leading to the formation of PS domains in a PC matrix [58] [15].

Different lipid phases often show a difference in height, leading to a height mismatch at the domain edge. Thus, lipids have to deform at the domain interface to avoid exposure of their hydrocarbon chains to water. Furthermore, the difference in lipid chain conformation leads to unfavorable steric interactions. Both effects lead to an energy cost at the domain boundary that is called line tension. Hence, minimal energy is obtained for minimal perimeter of the domain, leading to a circular domain shape, and/or budding out of the bilayer plane. A domain develops as follows: Upon a change in state (for example a change in temperature, ion concentration or curvature) the homogenous phase may be supersaturated by certain lipids that have to convert to a new phase to restore equilibrium. Concentration fluctuations within the homogenous phase lead to the nucleation of lipid clusters that grow by merging with either individual lipids or mobile domains. The size of the domains is governed by an interplay of entropy and line tension: Entropy favors a large number of small domains while line tension favors a single large domain [59]. Furthermore, the rate at which domains merge may be influenced by repulsive interaction due to their phase boundary. Domains may be relatively stable depending on their size and the value of the line tension [60]. Apart from these purely physical mechanisms in biological systems domain size is regulated by lipid recycling and energy barriers provided by transmembrane proteins that hinder domain merging [61].

2.3 Mechanisms of protein-bilayer interactions

Most research on domain formation in model membranes has been performed in the absence of membrane-associated proteins. However, biomembranes contain proteins, and these do affect the formation of membrane domains. The next section of this thesis will give an overview of the mechanisms involved in protein binding to lipid bilayers and the influence of protein binding on domain formation. In section 2.3.3 an introduction to the binding mechanism and proposed structure of the protein Annexin II is given, whose binding structure and influence on domain formation is investigated in this work.

2.3.1 Mechanisms of lipid binding

The cell membrane consists of a variety of different lipid species that can be classified in two groups. The first group are bulk lipids whose concentrations are relative constant and who mainly serve as structural backbone. Examples of such lipids are phosphatidylserine (PS), phosphatidylcholine (PC), cholesterol, sphingomyelin and phosphatidyletholamin (PE) . The second group are low abundance lipids which are thought to function as signaling molecules and thus their concentration fluctuates and depends on cell stimuli. Examples of such signaling lipids are: diacylglycerol, phosphatic acid, ceramide and phosphoinositide [62]. The type of lipid a protein binds to significantly influences its binding mechanism and the tendency to form lipid domains. Proteins that interact with signaling lipids respond spontaneously to the appearance of their ligands. In contrast, proteins that interact with bulk lipids must be triggered in their active state by specific signals. For example changes in Ca^{2+} level or phosphorylation of the protein lead to conformational and/or electrostatic changes of the protein. In addition, some proteins bind to signaling lipids leading to conformational and/or electrostatic changes that allow for their binding to bulk lipids. Furthermore, the location of the protein within the bilayer is also a critical factor that influences its binding mechanism. In general, there are three different classes of membrane binding proteins: S-type proteins that are located at membrane surfaces above the phosphate group and interact with the polar headgroup, I -type proteins that penetrate significantly into the interfacial region (i.e into the phosphate headgroup) and H-type proteins that interact with the lipids' headgroup and the hydrocarbon core region of the bilayer [62]. In this thesis the interaction of the protein Annexin II is investigated, which binds to anionic phospholipid headgroups bilayers via calcium bridging. Since today it is thought that the protein only interacts with the bilayers headgroup [63], Annexin II can be classified as a typical S-type protein.

Todays view of a protein binding to a bilayer is as follows: First, the protein approaches the membrane by diffusion. Charged residues on the protein surface exhibit an electrostatic interaction with the bilayer and thereby increase the association rate (k_a) of the protein to the membrane. The electrostatic interaction may be enhanced by phosphorylation of the protein or by calcium binding. In a second step, specific interactions, like hydrogen bonding, electrostatic or hydrophobic interactions, lower the dissociation constant (k_d) and tightly bound protein complexes are formed [62, 64]. Membrane insertion may then take place by conformational changes of the protein exposing hydrophobic side chains that are otherwise buried in the protein's interior [64]. For the binding to zwitterionic bilayers, aromatic side chains (Trp and Tyr aminoacid) are necessary due to the absence of electrostatic interactions. They are thought to affect both the association and dissociation rate to zwitterionic membranes.

To form tightly bound protein layers and to guarantee specificity for certain lipids, the following general mechanisms are used. (i) In the conformational switch mechanism, peripheral proteins undergo conformational changes after ligand binding or (de)phosphorylation. For example, lipid binding of epsin's ENTH domain causes the formation of a n-terminal domain that is necessary for membrane penetration [62]. Ca^{2+} binding to synaptotagmin's C2A domain causes the rotation of side chains of the calcium binding domain and the dephosphorylation of multiple sites in the C-terminal tail of PTEN cancels intermolecular electrostatic interactions and exposes cationic residues that bind to anionic phospholipids. (ii) In the electrostatic switch mechanism, the affinity of the proteins for their target is increased by increasing the electrostatic potential at the membrane binding site. Proteins that use this mechanism are for example S-/I type C2A domains of synaptotagmin or Annexins. Here, Ca^{2+} binds to the C2 domain of the Annexin repeat, increases the electrostatic potential at the membrane binding surface, and thus increases the proteins affinity for anionic membranes. In summary, unspecific interactions increase the rate of diffusive target location, while specific interactions lead to tightly bound proteins performing their task at or within the lipid bilayer.

2.3.2 The influence of protein binding on domain formation

The ongoing quest of domain formation in lipid bilayers has led to a variety of theories about the underlying mechanism. However, the role proteins may play is still lying in the dark, as well as the explanation of the fact that model systems exhibit a different behavior than cell membranes in vivo. In fact domains in vivo exist, if at all, only at the microscale. In living cells certain immobile proteins interact preferentially with domain walls. These proteins act as surfactants and reduce lipid phase separation by decreasing the critical temperature of the system.Thus, the binding of proteins may lead to a hinderance of domain formation in vivo even in lipid systems that are immiscible in model systems at physiological temperatures [65]. However, other theoretical concepts see protein lipid interaction as the main mechanism behind lipid raft formation. In this setting, protein-protein and protein-lipid interaction may stabilize small domains to form larger platforms [13]. Certain proteins interact with raft lipids, then cluster and bring the lipids together for raft formation [66, 67]. In contrast, May *et al.* propose that preferential interactions of certain lipids in the bilayer may already lead to domain formation in the absence of lipid binding proteins. In this view, preferential interactions between proteins and certain lipids may lead to a redistribution of these lipids to the interaction zone and thus to an additional mechanism for domain formation [57, 68]. Lipid demixing is then governed by the gain in the proteins' absorbtion energy and the loss in entropy through lipid redistribution. The large variety of membrane binding proteins, with all their different tasks already demonstrates the complexity of protein bilayer interaction and their role regarding domain formation. It is still a matter of lively debate and research whether there is one summarizing theory or if each individual protein has its own underlying physical and chemical mechanism that influences the bilayer structure.

2.3.3 Calcium dependent binding of Annexin to negatively charged phospholipids and the structure of Annexin II

Annexins belong to the class of calcium regulated proteins. They bind to acidic lipids and are characterized by the unique architecture of their calcium-binding sites. An important feature of their binding mechanism is that these proteins bind to the surface of the bilayer, and the bound lipids remain embedded in the bilayer matrix [8, 69, 70]. Annexins play a role in various cellular processe that occur at or within the lipid bilayers of cells. Examples are membranecytoskeleton linkages, exocytic and endocytic transport steps, and the regulation of ion fluxes across membranes [63]. It was shown that the binding of some Annexins, namely Annexin I, II and IV plays a role in the formation of phospholipid domains, presumably due to a segregation of negatively charged lipids accumulating underneath the proteins [63, 8]. However, for Annexin II (Anx A2) this could only be shown indirectly. Atomic force microscopy measurements on model bilayers revealed an area of depletion of negatively charged lipid in the surrounding of bound Annexin II [15]. One part of this work is to investigate the binding of the protein to surface supported bilayers and to prove the hypothesis of domain formation. In all Annexins the conserved core domain promotes the calcium dependent reversible attachment of the proteins to acidic lipids. The domain consists of approximately 300 amino acid residues and has the appearance of a slightly curved disc that embodies four annexin repeats. Hydrophobic interactions between repeat 1 and 4, and 2 and 3 stabilize a cyclic arrangement of these domains. Each Annexin repeat is composed of five α-helices (named A-E). Short loops or turns intercalate the helices and inhabit the calcium binding sites of the protein (for graphic illustration please see figure 2.6). The binding to phospholipids is mediated by a calcium bridge in which the calcium ion is simultaneously coordinated by ligands of the protein and polar moieties of the phospholipid.

Originally, Annexins were thought to bind solely by nonspecific electrostatic interaction. However, they exhibit a preference for certain lipids (for example PS lipids bind with a higher affinity to Anx A2 than PE lipids) which is not explained by simple electrostatic interaction [63]. X-ray crystallography of Annexin II and Annexin V with its bound ligands uncovered two different Calcium binding sites: a double binding site at the loop between the A and B helices (called AB loop hereafter), and a single binding site at the

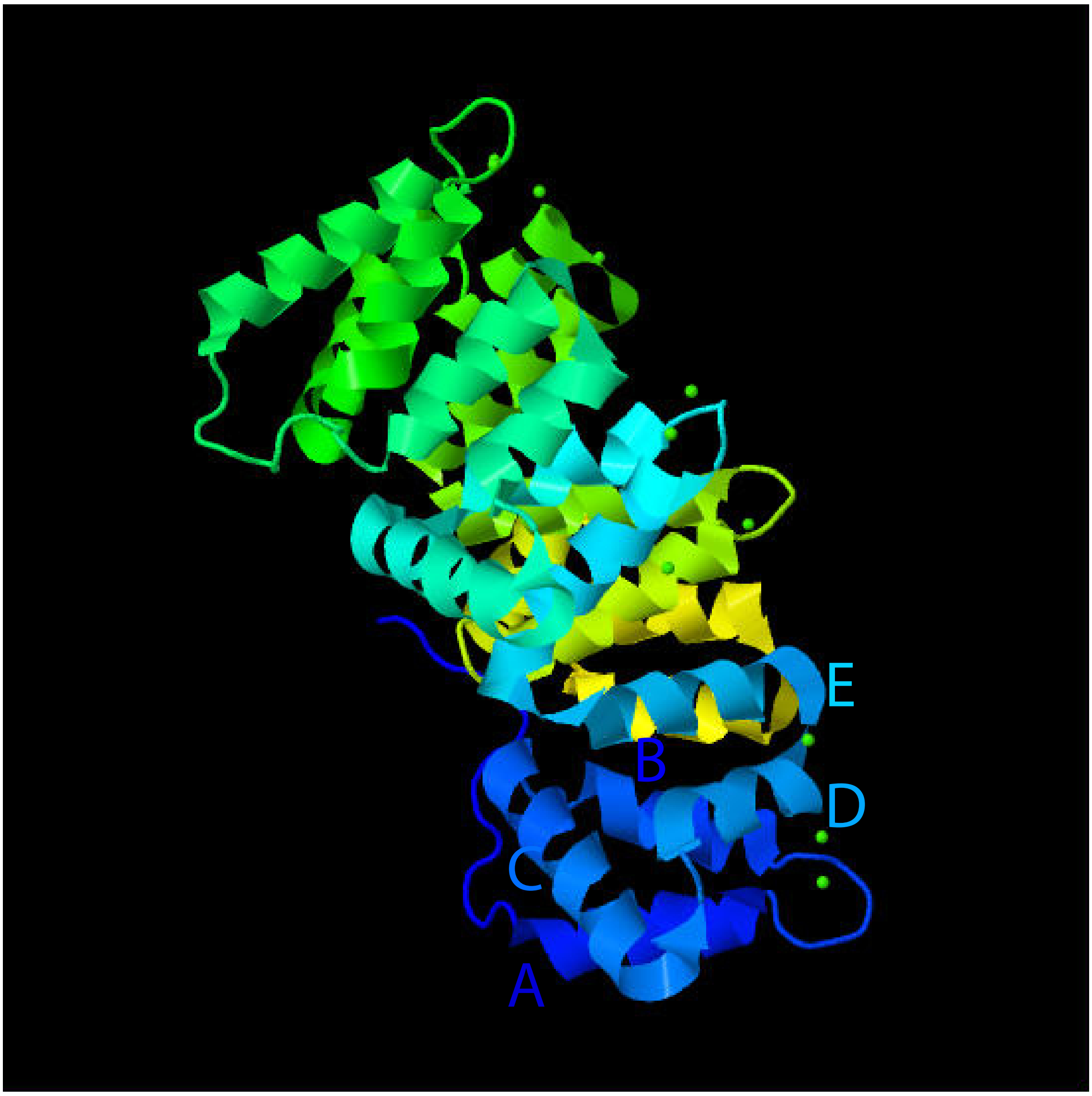

Figure 2.6: Structural model of an annexin core (Anx A5). Shown are the four Annexin repeats with bound calcium (*green spheres*). For repeat I helices A to E are marked. Each Annexin repeat exhibits two different calcium binding sites, a double binding site between helices A and B and a single calcium binding site between helices D and E. The figure was taken from [71].

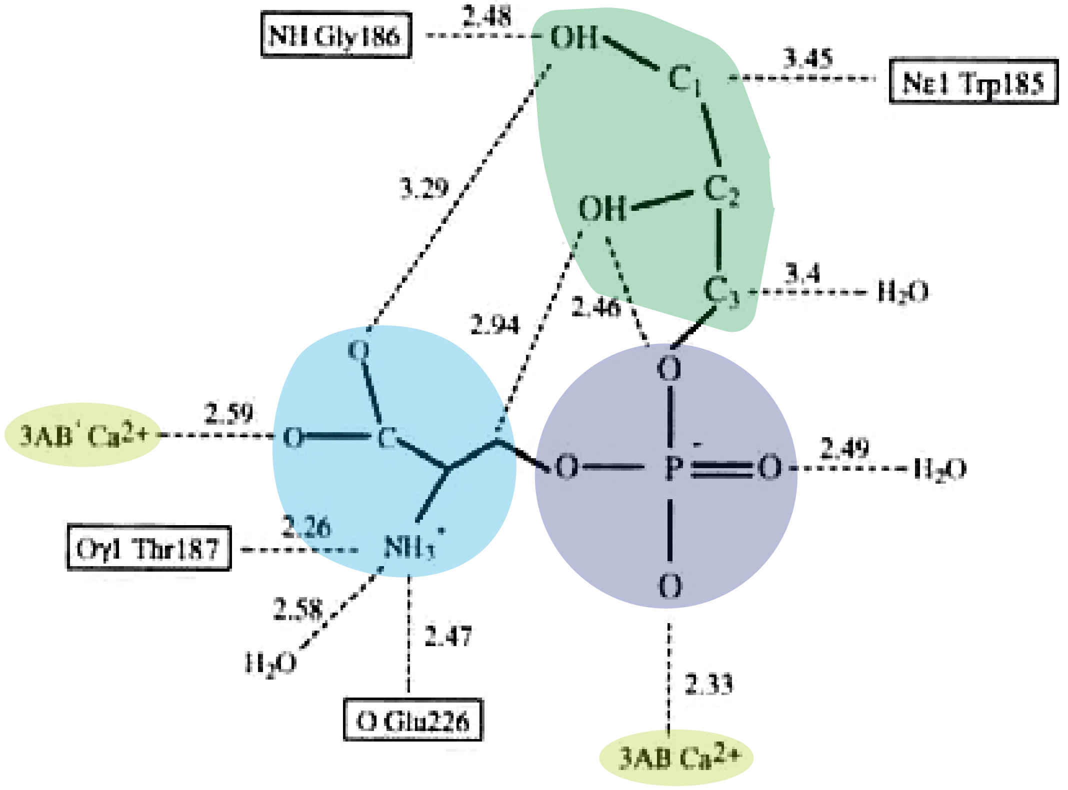

Figure 2.7: Binding conformation of a PS derivative without hydrocarbon chains when bound to Annexin V. Shown is the lipids serine group (*light blue*), phosphoryl group (*dark blue*) and glycine backbone (*dark green*). Dotted lines represent hydrogen bonds of the lipid to chemical groups of amino acid residues (*boxes*), water or by the protein coordinated calcium ions (*light green*). The length of the hydrogen bond is given in Angstrom. Reprinted by permission from Macmillan Publishers Ltd: [Nature Structural Biology] [70], copyright (1995).

loop between the D and E helices (called DE loop hereafter) (see figure 2.6) [70, 72]. Both binding sites reside at the protein surface facing the membrane. Genetic manipulation of the protein revealed that the AB loop calcium binding sites are required for membrane attachment, while the DE binding site "only" increases the binding affinity [72]. The binding of phospholipid analogues without phospholipid chains revealed that only the lipid's phosphoglycerol backbone and headgroup are necessary for lipid binding. However, they have to be oriented as if aligned in a lipid bilayer. In principle all four domains of Annexin are able to proceed in calcium bridging of the bilayer. The investigation of Annexin V showed that the protein flattens on membrane surface so that all calcium binding sites of all domains are accessible for the membrane interface. The binding of PS lipids to Annexin V is as follows: A glycine residue at position 186 of the protein coordinates the calcium ion in the AB loop with its carbonyl oxygen whereas its amide group interacts with the glycerol group of the phospholipid. The second calcium ion is coordinated by an oxygen

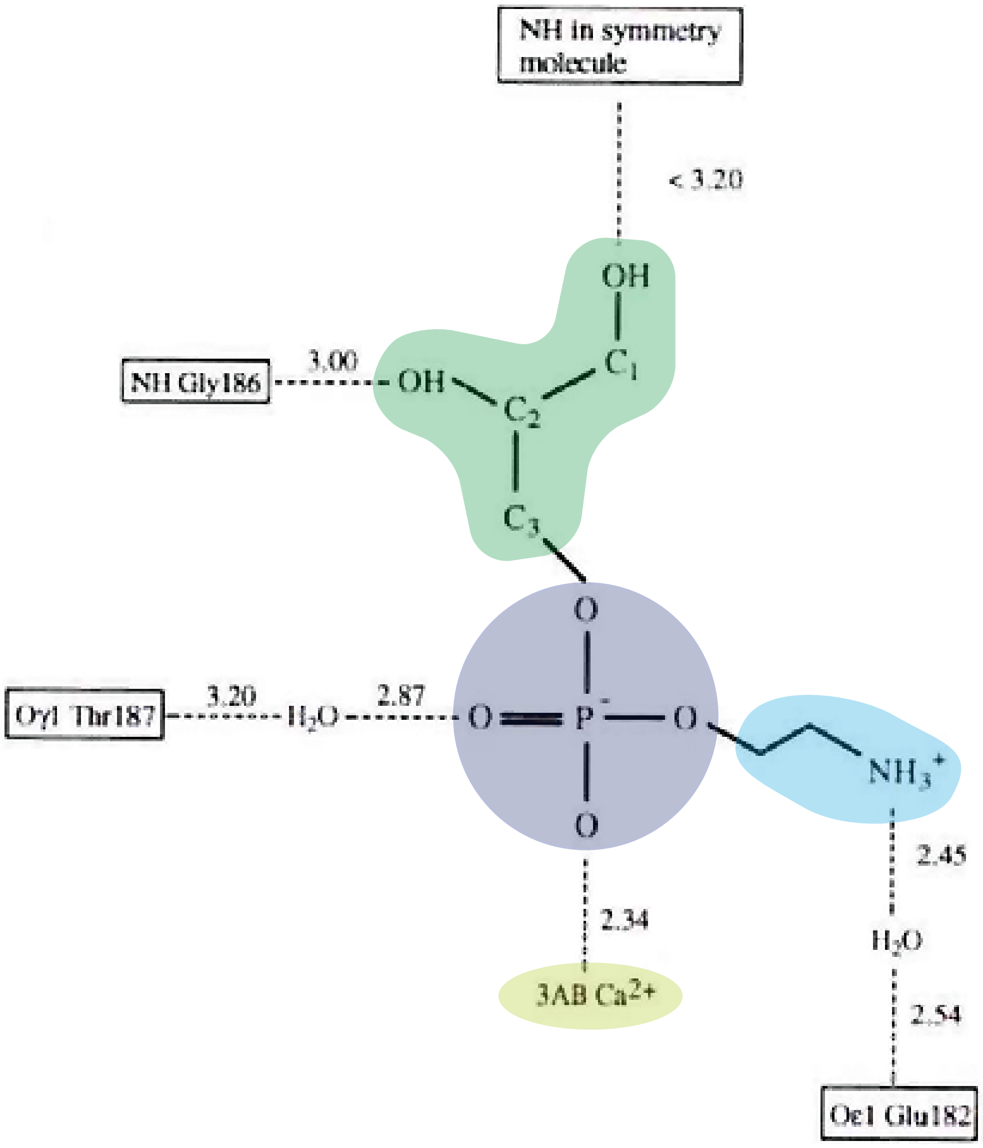

Figure 2.8: Binding conformation of a PE derivative without hydrocarbon chains when bound to Annexin V. Shown is the lipids etholamine group (*light blue*) that forms a hydrogen bond to a water molecule, the phosphoryl group (*dark blue*) and glycine backbone (*dark green*). Dotted lines represent hydrogen bonds of the lipid to water, by the protein coordinated calcium ions (*light green*) or chemical groups of amino acid residues (*boxes*). The length of the hydrogen bond is given in Angstrom. Reprinted by permission from Macmillan Publishers Ltd: [Nature Structural Biology] [70], copyright (1995).

atom of a carbonyl group of a threonine residue at position 187 and a hydrogen bond is formed between the amino group of the serine head and threonine's hydroxyl group (see figures 2.7). Apart from that, for PE and PS lipids, the oxygen atom of the lipids' phosphoryl backbone displaces one water molecule and coordinates with the first calcium ion of the AB loop (see figure 2.7 and 2.8).

The main binding mechanism between PE lipids and Annexin V is a hydrogen bond between the amino group of PE and the carboxylate oxygen of a glutamine residue at position 182 (see figure 2.8). Furthermore, the threonine residue at position 187 forms a hydrogen bond to one water molecule that forms a hydrogen bond to the phosphoryl oxygen of the lipid (see figure 2.8) [70]. This implies that phospholipids with chemical groups prone to hydrogen bonding at positions similar to the nitrogen of the etholamine group may also bind to the protein. Since PC lipids lack a chemical group, able to form hydrogen bonds at this position they do not bind to Annexin V in a calcium -dependent manner.

The difference in binding affinity of PS and PE lipids to Annexin V is explained by a different conformation of the etholamine headgroup. It extends in the opposite direction than the serine headgroup and shows less complementarity with the proteins surface [70]. As a summary, the high structural complementary between the lipid headgroup of PS lipids and the Annexin surface explains their selectivity as compared to other acidic lipids.

The structure of Annexin II. Annexin II is a member of the Annexin family that may exist in a monomeric (Anx A2m) or a heterotetrameric form (Anx A2t). Like other members of the Annexin protein family, it consists of two domains: the conserved core domain harboring the Ca^{2+} binding sites and a variable N-terminal domain exposing interaction sites for other protein partners. The heterotetrameric complex (Anx A2t) is formed via its N-terminal with S100A10 (p11). S100A10 belongs to the S100 protein family, although it is distinct from the other members of this family as it does not undergo Ca^{2+} dependent conformational changes. Even in the absence of Ca^{2+}, S100A10 is in the active state and, like most other S100 proteins, forms an antiparallelly packed non-covalent homodimer [73]. To date, no experimentally resolved high-resolution structure of the full length complex of Anx A2t is available. However, data of the Anx A2 monomer missing the first 19 amino acids [74, 75], as well as of the complex between dimeric p11 and two synthetic N-terminal fragments composed of the first 11 amino acids of Anx A2 exist [73]. Based on these data, a structural model of the Anx A2t complex has been created by computational modeling [76]. Yet, there is still a controversial discussion about the organization of Anx A2t when bound to a single membrane and the complex that is formed upon membrane-membrane connection.

On the one hand, when binding to a single surface supported membrane, the thickness of an Anx A2t layer obtained from scanning force microscopy experiments suggested that two Anx A2 monomers are connected by a p11 dimer in a side-by-side configuration to the membrane interface [69], see figure 2.9. It has frequently been proposed that the contact between membranes may then be mediated via the interaction of two opposing Anx A2t

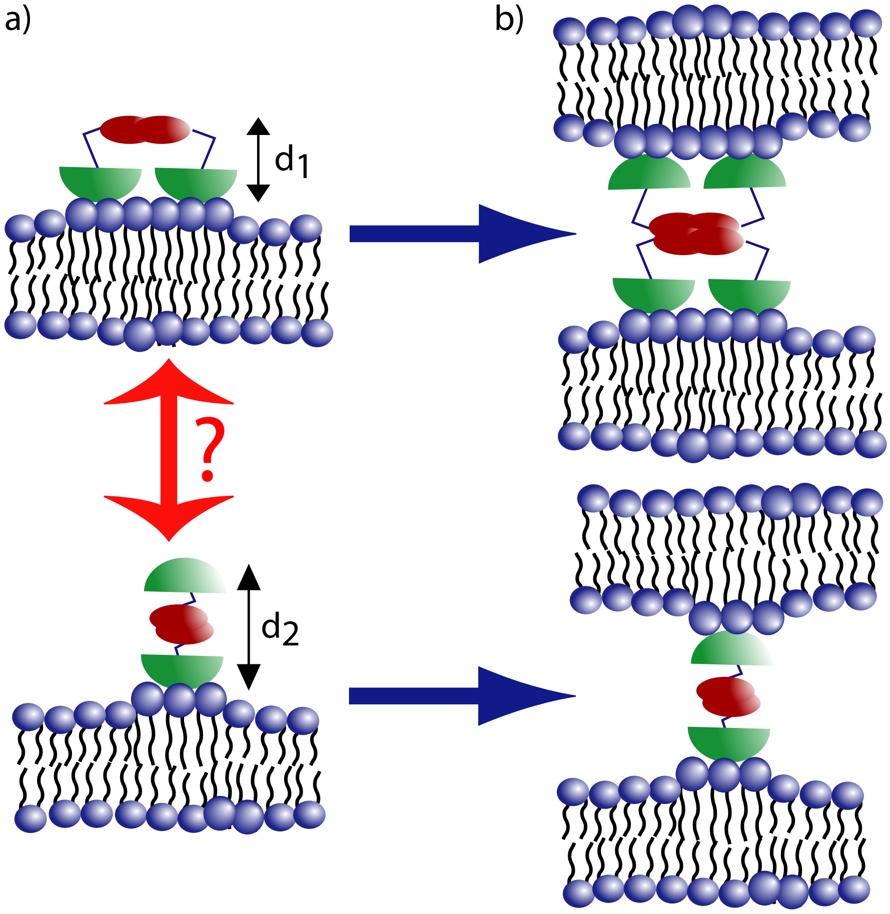

Figure 2.9: Cartoon of the molecular arrangement of Anx A2t when bound to a single bilayer (*a*) and the resulting conformation when bound to two bilayers (*b*). Anx A2 monomers are represented by green half spheres the p11 dimer is represented by red ellipsoids.

complexes by formation of a heterooctameric structure [69, 77, 78]. On the other hand, based on cryoelectron microscopy results on Anx A2t-connecting vesicles, it was proposed that the Anx A2t complex bridges membranes in a vertical configuration [79], in which each Anx A2 monomer binds to one of the membranes while the p11 dimer is located in between (see figure 2.9) [76]. From these measurements the same, albeit hypothetical, structure was proposed for the protein when binding to a single bilayer [69]. Importantly, the vertical configuration of Annexin A2t, as obtained from membrane-membrane junctions, is predicted to result in a larger thickness of the protein layer than the side-by-side configuration [76, 78, 80, 81]. However, during atomic force microscopy (AFM) experiments as described in ref.[69] a certain force is exerted on the soft protein layer and therefore its thickness might be underestimated. Hence, to date, it cannot be excluded that Anx A2t also binds to a single lipid bilayer in the vertical arrangement. One task in this work was thus to examine Annexin II structure when bound to a single solid supported bilayer.

2.4 Diffusion of lipid bilayers

The bilayer of a living cell is a constantly changing structure, since thermal agitation induces lateral movement of the lipids and proteins. Here an overview over the theoretical description and the experimental methods to scrutinize the mobility of lipids will be presented.

2.4.1 Theory of Diffusion

The movement of a particle in time and space is described by the diffusion equation

$$\frac{\partial c(\vec{r},t)}{\partial t} = D \cdot \nabla^2 c(\vec{r},t). \tag{2.21}$$

Here, $\vec{r}$ is the location in space, D is the diffusion constant, ∇^2 is the Laplace operator and $c(\vec{r},t)$ is the particle concentration at location $\vec{r}$ and time t. In a homogenous, two-dimensional system as a bilayer membrane, Eq. (2.23) is solved by

$$c(\vec{r},t) = \frac{1}{4\pi Dt} e^{-\frac{r^2}{4Dt}}. \tag{2.22}$$

From this equation, a simple relation between the mean square displacement $\langle r^2 \rangle$ and the diffusion constant D can be derived

$$\langle r^2 \rangle = 4Dt. \tag{2.23}$$

In homogenous lipid fluid phases, the diffusion of lipids can be derived from free volume theory [82]. For diffusants that are comparable to the size of the lipids, the surrounding matrix is treated as a quasi-crystalline liquid. A diffusive step happens if a free volume large enough and adjacent to the molecule exists. Free volume in the matrix is formed by density fluctuations. Since molecules possess a kinetic energy, the diffusant moves into the adjacent free space. If another density fluctuation closes the free space left by the molecule, before it can reenter the hole, the diffusive step is completed [83, 84]. Within this model the diffusion constant in a two dimensional system is defined by [85, 86]

$$D = \int_{a_0}^{\infty} D(a_s)p(a_s)da_s, \tag{2.24}$$

with $D(a_s)$ the diffusion constant inside the free space, and $p(a_s)$ the propability of finding a free area of size a_s. All free areas that are smaller than the critical free area a_0 do not contribute and are ignored. The probability of finding a free space is given by

$$p(a) = \frac{\gamma}{\langle a_f \rangle} e^{-ba_s/\langle a_f \rangle}, \tag{2.25}$$

where the average free-area $\langle a_f \rangle = a_t - a_0$, with a_t the average area per molecule. The constant b is between 0.5 and 1 and accounts for overlap of free area. Almeida and MacCarthy have argued that the critical area a_0 is defined by the closed packed area of the lipids in the solid phase, leading to $\gamma = 1$ [85, 87, 88]. Inserting Eq. (2.25) into Eq. (2.24) leads to

$$D = D(a_0)e^{-ba_0/\langle a_f \rangle}. \tag{2.26}$$

It was proposed that in lipid bilayers the rate of diffusion is limited by the separation of the neighboring lipid headgroups [84]. Furthermore, it is required that the diffusant has enough energy E_a to break its bonds with the neighboring lipids. With these assumptions Eq. (2.26) is modified to [86]

$$D = D(a_0)exp\left(\frac{-ba_0}{\langle a_f \rangle} - \frac{E_a}{kT}\right), \tag{2.27}$$

with k the the Boltzmann constant and T the temperature.

For molecules larger than the bilayer lipids, the free space diffusion model does not explain experimental observations [82]. If the diffusing molecules are large enough, the surrounding lipid solvent can be treated as continuum, where motion is provided by collision with the lipids and opposed by frictional forces, with frictional coefficient f of the solvent. The diffusion constant is then given by:

$$D = \frac{kT}{f}. \tag{2.28}$$

For spherical particles this leads to the Stokes-Einstein equation for the diffusion in a three dimensional viscous fluid:

$$D = \frac{kT}{6\pi\eta R_D}. \tag{2.29}$$

Here, R_D is the radius of the diffusant and η the viscosity of the lipid matrix. Saffman and Delbrück solved the Navier Stokes equation for the case of a bilayer, assuming that a bilayer with viscosity η and thickness d_b is bounded by a fluid on both sides with much lower viscosity η_1. In this case the frictional coefficient f in Eq. (2.28) becomes

$$f = 4\pi\eta d\left(\ln\frac{\eta d_b}{\eta_1 R_D} - \gamma\right)^{-1}, \tag{2.30}$$

where $\gamma = 0.5772$ is Euler's constant.

2.4.2 Anomalous diffusion

Diffusion studies in cell membranes revealed that Eq. (2.23) does not always describe the mobility of tracer molecules in the lipid bilayer. In some cases diffusion is better described by

$$\langle r^2\rangle = 4Dt^{\alpha}. \tag{2.31}$$

Here α is called anomalous exponent. For $0 < \alpha < 1$ the diffusion is slower than free diffusion and is called anomalous diffusion [89]. Correlation between diffusing particles, lipid-protein interactions or lipid microdomains in the bilayer are among the reasons that lead to anomalous diffusion. The characteristic length scale of the measurement and its relation to the domain size has a strong influence of the obtained diffusion mode and coefficient. For length scales small compared to the size of the obstacles the tracer molecule may diffuse freely. For measurements with intermediate length scales it may exhibit anomalous diffusion, while on large length scales it may follow free diffusion with a reduced effective diffusion coefficient D_{eff}. Mobile obstacles have a less pronounced effect on the diffusion than immobile ones, and the transition to free diffusion shifts to larger observation length scales the larger the area occupied by obstacles [89]. In the case of impermeable obstacles the fraction of surface area occupied by the obstacles a, can be related to the effective diffusion coefficient D_{eff} and the diffusion coefficient in the absence of obstacles D_0 [89]:

$$D_{eff} = D_0(1-2a)\,. \tag{2.32}$$

2.4.3 Experimental methods to quantify lipid diffusion

FRAP. Studies of the mobility of lipids and proteins within lipid membranes have provided the basis for understanding the dynamics and lateral structure of the cell's bilayer [90]. Early fluorescence recovery after photobleaching (FRAP) investigations, gave the first hints that a cell's lipid bilayer is not a homogenous fluid but consists of domains with different diffusivity [91]. Variation of the bleached spot size revealed an increase in immobile fraction of the observed diffusant, leading to the assumption that the membrane consists of protein rich and protein poor domains. In FRAP experiments an intense laser beam irreversibly photobleaches fluorophores in a small area of the membrane. The level of fluorescence recovery over time into the bleach spot is recorded at low laser power. With adequate mathematical models information about the diffusion constant D and the mobile fraction are obtained from the recovery data [92, 93, 94]. A drawback of this method is that various processes, like molecular interactions, membrane flow or directed movement by transport processes all contribute to the obtained data. Thus, different diffusion modes are not directly visible [92, 95].

SPT. Single particle tracking methods (SPT) on the other hand, directly visualize the movement of single tracer molecules in the bilayer. The motion of tracer molecules is captured with the microscope camera and the sampling rate has to be adapted to the investigated system. Trajectories in time and space of individual molecules are obtained. The analysis of these trajectories may reveal different diffusion modes and diffusion coefficients. For example, SPT revealed two different diffusion modes on different time scales of gold-labeled DOPE molecules in cell membranes, a short time confined diffusion in compartements and a long term “hop diffusion” between the compartements [96]. SPT has also revealed the mechanism and time scale of domain formation in lipid bilayers [97], the origin of the slow diffusion of protein clusters as compared to single proteins or the compartement sizes in cell membranes of different mammalian cell types [96]. However, the method requires a profound knowledge of the investigated system to adapt the sampling frequency and trajectory anaylsis [95]. Furthermore, the tracing of single molecules requires a tracking software that is able to identify the investigated molecule even when it changes its shape and contrast due to out-of-focus movement or changes in illumination [92].

FCS. Fluorescence Correlation Spectroscopy (FCS) is another tool to investigate diffusion of proteins and membrane lipids. One of the first FCS experiments in two dimensional bilayer systems was performed by Schwille et al. who examined the diffusion of labeled lipids in rat cell membranes [98]. FCS revealed deviations from free diffusion in these cell membranes, while in GUVs with only one lipid phase the diffusion could be well described by one-component Brownian diffusion [98]. FCS statistically analyszes time traces of the intensity of a fluorescence signal $I(t)$ in a confined volume. Diffusion of fluorescent tracer molecules in and out of the detection volume causes intensity fluctuations, that are in the millisecond regime and can thus well be separated from photochemical processes that occur on faster time scales. Normalized autocorrelation functions $G(\tau)$ of the intensity time traces are obtained by [98]:

$$G(\tau) = \frac{\langle I(t)I(t+\tau)\rangle}{\langle I(t)\rangle^2}. \tag{2.33}$$

The autocorrelation functions are analysed by appropriate theoretical models. Information about the average number of particles in the detection volume and the diffusion time τ_D are gained [99]. With such an analysis, it is even possible to separate the fitting function into diffusion of species that follow different diffusion modes and times. For example, the influence of poly-lysine on the diffusion and structure in free standing bilayers was revealed [100]. The results indicated the formation of nanodomains in both bilayer leaflets that are sandwiched between two poly-lysine molecules [100]. A critical factor to obtain reasonable values is the form and size of the detection volume, which is defined by the focus of the confocal microscope. This is especially important in the case of planar lipid bilayers where the detection volume is defined by the intersection of the focus with the plane of the bilayer. The intersection changes its size at different focus depths [101]. Z-Scan FCS that measures the sample at varying defined sample positions is a callibration-free single focus method that overcomes this problem [89]. Z-scan FCS revealed that in DOPC SLB's the diffusion constant is more than two fold slower than in GUV's under the same buffer conditions - a difference which was attributed to the interplay between substrate and bilayer [102].

The above described methods all lead to the estimation of diffusion constants in lipid bilayers. For instance, FRAP experiments measure diffusion on the micrometer scale, while the characteristic length scale in FCS is in the range of 500nm [95]. In SPT experiments the spatial resolution is given by the localization of the tracer molecule and is today in the range of nm to a few tens of nm. However, the characteristic length scale of a SPT measurement is related to the time interval of the measurment t_m via the diffusion coefficient D of the studied tracer molecule $t_m \sim 1/(4D)$ [89]. This discrepancy between the measurement methods has a profound influence on the obtained diffusion constants. Guo *et al.* compared the diffusion in fluid POPC SLBs on glass by FRAP, various FCS techniques and SPT [95]. FCS yielded an about two fold larger diffusion constant than FRAP measurements while the diffusion constant obtained from SPT measurements was in the same range as obtained in FCS experiments but with a large standard deviation. They attributed this large standard deviation to a broad distribution of diffusion rates in the system, also explaining the differences among the other methods based on their different spatial and temporal resolution. Thus, the decision for one or another method depends mainly on the time scale of the process under study and on the spatial resolution required.

Continous bleaching. All methods to quantify lipid diffusion described so far, have the drawback of a costly instrumental setup. On the other hand, standard fluorescence microscopy is an investigation method that is widely used in biological experiments. A common nuisance of this method is the photobleaching of the fluorescence sample during investigation. Yet, it turned out that this bleaching can also be exploited to gain information of the mobility of the fluorescent label [103]. If a mobile two-dimensional sample is bleached inside the aperture of a microscope, a bright rim develops at the boundary of the illuminated area (see figure 2.10a). Qualitatively, the characteristic width ξ of this rim is determined by an interplay of fluorophore-bleaching *inside*, and diffusion of unbleached fluorophores *into* the illuminated area. Hence, the width of the rim together with the bleaching rate k of the dye holds information about the diffusion constant D of the sample. For the ideal scenario of an evenly illuminated slit aperture, Dietrich *et al.* [103] developed a simple analytical approximation of the one-dimensional reaction-diffusion equation in the long-term limit and, in fact, identified $\xi = \sqrt{D/k}$ as the characteristic decay-length of the rim. Under laboratory conditions, however, one is faced with less ideal conditions. Typically, the lamp of the microscope produces a curved illumination profile, resulting in complications: First, even for a homogeneous distribution of dyes across the sample, areas with higher illumination appear brighter and are thus interpreted as regions of higher

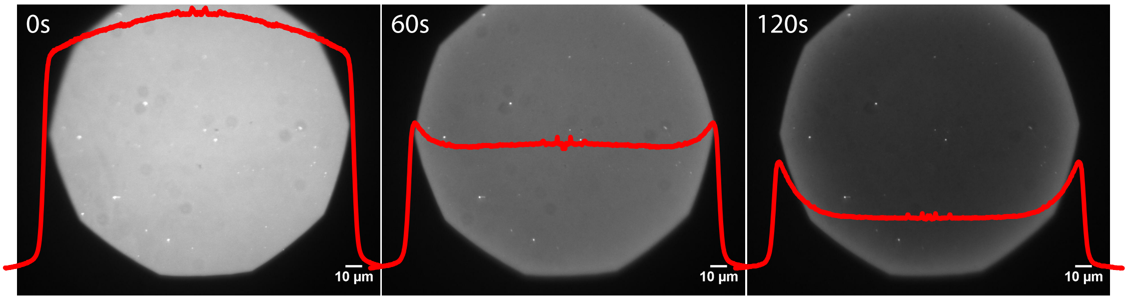

Figure 2.10: Fluorescent microscopy time series of a mobile lipid bilayer and corresponding radial intensity profile (*red line*).

concentrations. Yet, if the illumination profile is known, this can be easily corrected for by standard image processing techniques. The second effect is more severe, as the regions of higher intensity are exposed to higher rates of photobleaching, resulting in bleaching profiles that depend heavily on the lamp-profile in the experimental setup. Moreover, in typical light microscopes the aperture is circular rather than rectangular. To the best of our knowledge, there exists no analytical solution of the reaction-diffusion equation for arbitrary bleaching profile and for a circular aperture.

In section 3.2.4, a tool is presented for the faithful extraction of diffusion constants by continuous bleaching under typical laboratory conditions. The method solves the reaction-diffusion equation in a numerical way and therefore allows the versatile prescription of any experimentally measured illumination profile. While the diffusion constant was previously estimated from a single concentration profile after prolonged exposure [103], with this approach a whole *timeseries* of concentration profiles is fitted. The additional information contained in those time-resolved measurements enables the rapid extraction of diffusion constants within observation times as short as 30 seconds. This is particularly useful, since prolonged irradiation can heat the probe and induce structural changes in the lipid membrane. Hence, minimal exposure times are highly desired for noninvasive mobility determinations.

2.4.4 Microscope setup

SLBs were controlled by fluorescence microscopy using a transportable Zeiss Axiotech vario fluorescence microscope (Oberkochen, Germany) equipped with 10x (NA 0.3) and long-distance 63x (NA 0.75) Plan- Neofluar objectives (see figure 2.11). Images were captured with an ORCA C4742-95 CCD camera and WASABI imaging software from Hamamatsu Photonics (Tutzing, Germany). For continuous bleaching experiments, a 120 W mercury short arc reflector lamp (HXP-R120W) was used.

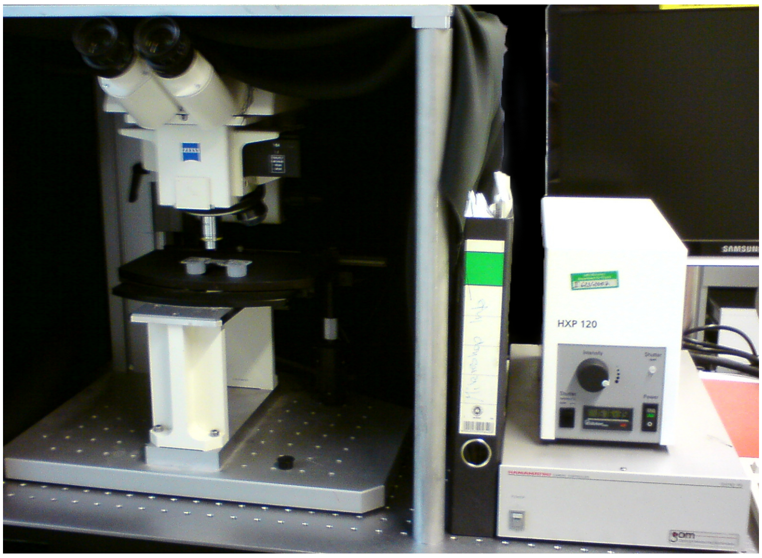

Figure 2.11: Microscopy setup.

2.5 The investigation of bilayer structure with x-ray and neutron reflectometry

In recent years, x-ray and neutron reflectivity have become a valuable tool to study phenomena at interfaces in nanometer resolution. Today's high brilliance synchrotron radiation sources provide electromagnetic waves in the keV regime. X-ray reflectivity using this radiation allows for the determination of electron density depth profiles with Angstrom resolution. Complementary information is obtained by neutron reflectivity . Neutron reflectivity allows for the determination of the scattering length density depth profile with nm resolution. The lower resolution is due to reduced flux at neutron sources. However, isotopes of the same atom interact differently with neutrons. Therefore contrast variation may be performed to emphasize specific parts of the sample. For example, deuteration of certain lipids permits the determination of the transmembrane location of labeled groups within lipid bilayers [104]. The structure and dimension of the subunits of the enzyme methyltransferase could be solved by deuterating certain units and using different solvent contrasts [105].

2.5.1 Theoretical background

When neutrons or electrons impinge on a surface, they are either reflected or refracted (figure 2.12). The incoming beam can be described as plane wave traveling in a medium with complex refractive index of refraction,

$$n = 1 - \delta + i\beta \,. \tag{2.34}$$

For x-rays, δ is given by

$$\delta = \frac{r_e}{2\pi}\lambda^2\rho_e\,, \tag{2.35}$$

where λ is the wavelength of the incident wave, r_e is the classical electron radius and ρ_e is the electron density of the medium. For x-rays the electron density of a molecule with different atoms i can be transformed to a scattering length density, approximated by [106]

$$\mathrm{SLD}_e = \frac{\sum_{i=1}^{n} Z_i r_e}{V_m}\,, \tag{2.36}$$

where Z is the atomic number and V_m is the volume of the molecule. The imaginary part β is given by,

$$\beta = \frac{\lambda}{4\pi}\mu\,, \tag{2.37}$$

where μ is the linear absorption coefficient. For neutrons δ and β are given by

$$\delta = \frac{Nb}{2\pi}\lambda^2\,, \tag{2.38}$$

and

$$\beta = \frac{\lambda\sigma_a N}{4\pi}\,. \tag{2.39}$$

Here, N is the atomic number density, b is the bound coherent scattering length, σ_a is the adsorbtion cross section and λ is the wavelength of the neutron beam. The scattering length density of a material interacting with neutrons is given by [106]

$$\mathrm{SLD}_n = \frac{\sum_{i=1}^{n} b_i}{V_m}\,, \tag{2.40}$$

where b_i the tabulated coherent scattering length of the i^{th} atom in the molecule.

For most media the refractive index is smaller than unity and on the order of 10^{-6}. Therefore, x-rays or neutrons impinging with small angles on a surface are totally reflected. The angle of total reflection θ_c, can be calculated from Snell's law

$$n_0 \cos\theta_0 = n_1 \cos\theta_1\,. \tag{2.41}$$

With $\theta_1 = 0$, θ_c is given by $\cos\theta_c = n_1/n_0$. From Eq. (2.41) one can write

$$n_1 \sin\theta_1 = (n_1^2 - n_0^2\cos^2\theta_0)^{1/2}\,. \tag{2.42}$$

For incident angles below θ_c, $n_1^2 \leq n_0^2\cos^2\theta_0$ and thus $n_1\sin\theta_1$ is fully imaginary, corresponding to an evanescent neutron or x-ray wave.

The reflected intensity for incident angles $\theta_0 > \theta_c$ for two media, as shown in figure 2.12a, is given by Fresnel's law

$$R = \left|\frac{n_0\sin\theta_0 - n_1\sin\theta_1}{n_0\sin\theta_0 + n_1\sin\theta_1}\right|^2 \equiv |r_{01}|^2, \tag{2.43}$$

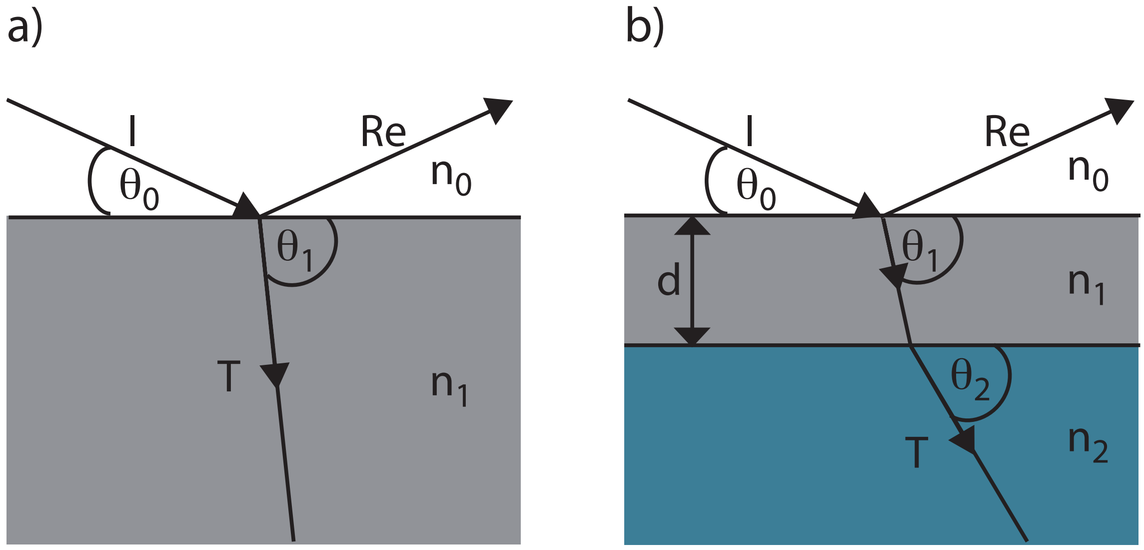

Figure 2.12: a) Sketch of the interface between two media with refractive index n_0 and n_1 with the incident (I) and reflected wave (Re) with angle θ_0 and the transmitted wave (T) with angle θ_1. b) Situation with a film with refractive index n_1 and thickness d between two media with refractive index n_0 and n_2.

where r_{ij} is the Fresnel coefficient at the ij interface. For a single film on a substrate (see figure 2.12*b*) the reflectivity is given by [106]

$$R = \left| \frac{r_{01} + r_{12}e^{2i\phi}}{1 + r_{01}r_{12}e^{2i\phi}} \right|^2 , \tag{2.44}$$

where $\phi = (2\pi/\lambda)n_1 d \sin\theta_1$ is the optical path length (or phase factor) in the film and d the thickness of the film (medium 1).

While Eq. (2.44) holds for idealized media in which the index of refraction n changes discontinuously from one medium to the other, in real systems a continuous variation in the scattering length density (SLD) profile perpendicular to the sample surface gives rise to a gradual change of n (cf. Eqs. (2.35) and (2.38)). Nevertheless, the interfacial structure can often be well approximated by a slab model with layers of thickness d_i, scattering length density $\mathrm{SLD_i}$ and roughness $\sigma_{i,i+1}$ at the interface between slab i and $i+1$ [107]. In this case the roughness modulates the Fresnel coefficient between layers i and layer $i+1$ in Eq. (2.43) according to

$$r_{i,i+1} = \frac{n_i q_i - n_{i+1}q_{i+1}}{n_i q_i + n_{i+1}q_{i+1}} \exp\left(-\frac{q_i q_{i+1}\sigma^2_{i,i+1}}{2}\right) , \tag{2.45}$$

where in each layer the momentum transfer q_i perpendicular to the surface is defined as

$$q_i = \frac{4\pi}{\lambda} \sin\theta_i \, . \tag{2.46}$$

The thickness of each layer d_i causes a phase factor $\phi_i = n_i q_i d_i/2$ (see above) and a characteristic matrix in terms of phase factors and Fresnel coefficients for each layer is defined as [107]

$$\mathbf{C}_i = \begin{pmatrix} \exp(i\phi_i) & r_i \exp(i\phi_i) \\ r_i \exp(-\phi_i) & \exp(-\phi_i) \end{pmatrix} . \tag{2.47}$$

The matrix elements M_{21} and M_{11} of the product of the characteristic matrices of all slabs $\mathbf{M} = \prod \mathbf{C}_i$ give the reflectivity [107]

$$R = \left| \frac{M_{21}}{M_{11}} \right|^2 . \tag{2.48}$$

This formalism is called Abeles formalism and is used in the program motofit ([107]), which was leveraged to fit reflectivity data throughout this thesis.

2.5.2 Instrumentation

In this thesis, surface supported bilayers of different composition were investigated with x-ray reflectivity at the beamline D4 at the Hamburger Synchrotronstrahlungslabor (HASYLAB) at the Deutsches Elektronen Synchrotron (DESY), Hamburg, Germany, and at the beamline ID01 at the European Synchrotron Radiation Facility (ESRF) in Grenoble, France. Neutron reflectivity experiments were performed at the instrument AMOR at the Paul Scherrer Institut (PSI), Villingen, Switzerland.

As an example of an x-ray reflectometer, the setup of the instrument D4 at HASYLAB is shown in figure 2.13. D4 is a bending magnet x-ray scattering instrument. It may be used in different operation modes, serving for diffraction and scattering investigations of solid-states to liquids. In this thesis, all measurements at D4 were performed in the reflectometer mode in horizontal scattering geometry. The beam impinges from the short side of the microfluidic chamber (please see figure 2.14 for an illustration of the chamber). The incoming beam is fixed and the sample is tilted to set an incident angle θ. The detector is at the same time tilted by an angle 2θ to maintain reflection condition. All components of the instrument in figure 2.13 serve the purpose of creating a monochromatic beam of a given size centered on the sample's rotation axis. The mirror in the mirrorbox reflects low energy x-ray beams while high energy x-ray beams pass through the mirror and are absorbed i. e.it acts as a filter. A monochromator crystal is then set to a certain angle, selecting the desired x-ray energy band by Bragg reflection. The monochromatic beam passes through an evacuated flight tube. At the end of the flighttube a slit defines the beam height and width. Furthermore, parts of the incident beam are scattered into a detector (the so called monitor) to correct for intensity variations during the measurement. The beam impinges on the sample and the reflected beam passes through a second flighttube and is collected by a detector. A large momentum transfer range can be gained by changing the incident angle up to values of 2 degrees.

An example of a neutron reflectometer is the instrument AMOR at the Paul Scherrer institut (PSI). It is a time of flight (TOF) neutron reflectometer, receiving its neutrons

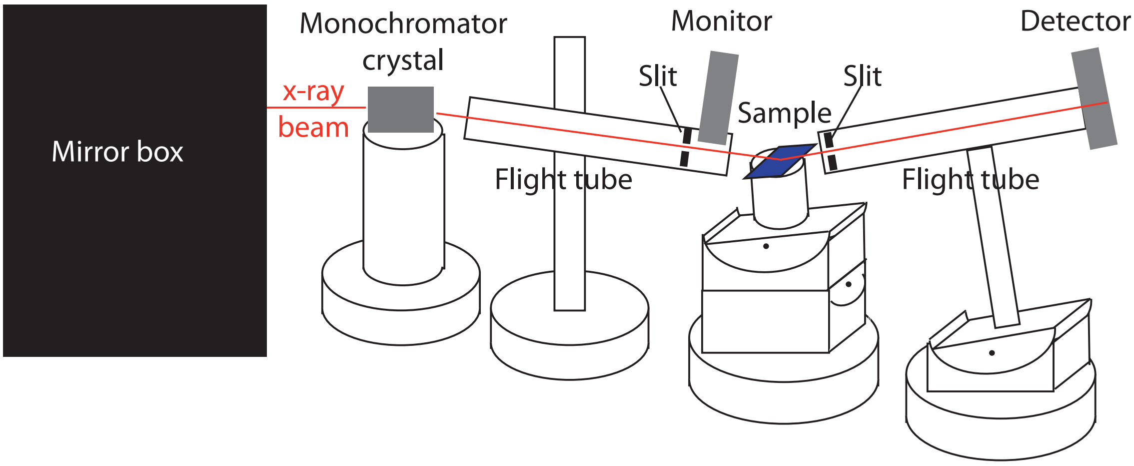

Figure 2.13: Setup of the reflectometer D4 at Hasylab.

from the continuous spallation source SINQ. A cold moderator of liquid deuterium (cold source) slows the neutrons down and shifts their spectrum to lower energies. The neutron beam then passes a double chopper system, defining the wavelength band. The two chopper discs have two slits each with variable opening. They are phase-coupled with a maximum speed of 6000 rpm leading to a maximal burst rate of 200 Hz. The distance between the chopper and the detector can be set between 3.5 and 10 m and the chopper frequency can be varied. The resolution can be optimally adapted to the experiment, ranging from $\delta q/q = 1\%$ to 10% [108]. A momentum transfer range is achieved by neutrons with different wavelengths, defined by the chopper setting, and a changing of the incident angle θ. The wavelength of each neutron hitting the detector is calculated from the time t_{tof} it travels from the chopper system to the detector

$$\lambda = \frac{h t_{tof}}{m_n L}, \tag{2.49}$$

where h is the Planck constant, m_n the mass of a neutron and L the distance between detector and chopper system. Alternatively measurements may be performed in monochromatic mode. A monochromatic beam is obtained by a thin film Ni/Ti multilayer stack, consisting of 1500 layers with a bilayer period of 5.2 nm [108]. In this mode, a momentum transfer range is obtained by varying the incident angle.

2.5.3 Experimental setup

X-ray reflectivity. For x-ray experiments, an energy of 19.75 keV was chosen to maximize the reflectivity signal while minimizing the beam damage in the microfluidic environment [109]. Sample chambers were mounted in a horizontal scattering geometry as described previously [26, 109]. Briefly, the incident beam enters the microfluidic chamber through a topas foil and passes through a 200 μm water-filled channel before hitting the sample. Reflected intensities were collected by tilting the sample between incident angles of $\theta = 0.02°$ and 2° with 142 steps at ESRF. For data collected at HASYLAB the sample was tilted between $\theta = 0.026°$ and 1.51° with 243 steps. This leads to a momentum transfer range q normal to the surface up to $q = 0.53$ Å^{-1} at HASYLAB and $q = 0.71$ Å^{-1} at ESRF. Here q is defined by $q = 2\pi \sin\theta/\lambda$, where λ is the wavelength of the incoming beam and θ is the incident angle. The beam cross section was defined by a presample aperture of 80 µm horizontal and 100 µm vertical at D4 and 250 µm horizontal and 1000 µm vertical at ID01. Evacuated beam guides with Kapton windows were positioned close to the sample chamber to minimized air scattering. The reflected intensity was collected with a NaI (cyberstar) detector. For each data point, the reflected intensity was integrated for one second. Automatic attenuators in front of the sample were used in order to reduce exposure to the full beam intensity. Furthermore, the sample was protected by a fast shutter system during motor movement. To control for radiation damage of bilayer and protein the samples were measured at the same sample position for a second time. No change in reflectivity signal of bilayer and protein layer was observed during this procedure. By detuning from the reflection condition, the background was determined and subtracted. The remaining reflection signal was corrected for illumination (footprint correction) and normalized to a reflectivity of one in the total reflection region. For graphical presentation, the data were multiplied by q^4, to compensate for the overall decay of the reflectivity signal.

Neutron reflectivity. For neutron reflectivity measurements the chopper was set to $f = 1400$ 1/min, an opening of 13.8 degrees and a phasing of 166.5 degrees, leading to a wavelength distribution from 1.5 Å up to 11 Å. Data binning was set to constant q binning so that a wavelength resolution between 3.8% and 4.5% was reached. The sample was measured at four angles, namely 0.5, 1.0, 1.5 and 2 degree, leading to a momentum transfer up to q $\approx$0.15 Å^{-1} before the signal vanishes in the background. The beam cross section was defined by three slits, S1, S2 and S3, before the sample, leading to a footprint smaller than the surface of the block. A fourth slit, S4, in front of the detector reduced the neutron flux into the detector. For incident angles 0.5, 1 and 1.5 degrees, the slit openings of S1, S2, S3 and S4 were set to 2 mm 0.3 mm, 1 mm and 4 mm, respectively. For the highest angle the slit opening of S3 before the sample was set to 1 mm and the slit opening of S4 before the detector to 3 mm. This leads to an overall angular resolution of 2.4%. The reflectivity data were normalized by the direct beam measurement and directly used for fitting.

2.5.4 Data evaluation

X-ray data evaluation. All reflectivity data were fitted with the program motofit that uses the Abeles algorithm [107]. For x-ray measurements, two different fitting strategies were performed: In a first model, a relatively small number of layers were chosen each layer representing different regions of the bilayer [110, 111]. In this model, thickness and electron density were chosen as fitting parameters. In a second approach, a high number of layers (slabs) was chosen and only the electron density set as free fitting parameter. In this case the thickness of each layer was set to the value equivalent to the resolution of the measurement [112]. The layer roughness was set to zero in both approaches. The fifteen best fits of both models were used to calculate the average electron density profile.

In the first model, for measurements performed at ID01, the electron density of the bilayer was calculated with two slabs for each lipid headgroup to allow for phase separation due to calcium binding [110, 111], and three slabs for the hydrophobic core of the bilayer [113]. Due to the lower resolution at D4 the bilayer data was fitted with only one slab for each phospholipid headgroup and three slabs for the hydrophobic core of the bilayer. In both measurements, an additional layer was added to account for the substrate roughness and hydration of the headgroup proximal to the silicon substrate. In the second approach the maximum thickness resolution in a reflectometry experiment can be calculated by π/q_{max}, where q_{max} stands for the maximum q value before hitting the background. This leads to a minimum slab thickness of 7 Å and 5 Å for data for data obtained at D4 and ID01, respectively. In this case, for data from ID01, thirteen layers, and ten layers for data from D4 were chosen to represent the bilayer. The same strategies were chosen to gain the electron density profile of the protein layer. In the first model six slabs were chosen and the electron density and thickness set as parameter. In the second approach the thickness of each layer was set to the minimum resolution and only the electron density was set as parameter. In the second case the number of slabs was set to eighteen slabs for the protein layer for 5 Å resolution and thirteen slabs for 7 Å resolution data. The roughness was set to zero and kept constant in both approaches. Further layers did not change the quality of the fit. A fit family was created by restarting the Abeles formalism with random starting parameters. From N final fits with electron densities $\rho_i(z)$ and χ_i^2 a weighted average electron density profile was calculated by

$$\langle\rho(z)\rangle = \frac{\sum_{i=1}^{N} \rho_i(z) e^{-\chi^2/2}}{\sum_{i=1}^{N} e^{-\chi^2/2}} \,. \tag{2.50}$$

Neutron data evaluation. Due to the lower q resolution of neutron measurements the neutron data was fitted with one slab for the silicon oxide layer, one slab for the bilayer and one slab for an Annexin layer. For all neutron measurements the thickness, the scattering length density and the roughness of each slab were set as fitting parameters.

2.5.5 Sample chamber

For microscopy and x-ray measurements microfluidic chambers made of COC (Topas, IBIDI, Munich, Germany) were used [109] and modified by drilling a cavity above the microfluidic channel (see figure 2.14). Silicon surfaces were glued with a two-part polymer (Microset Products Ltd, Warwickshire, UK) into the cavity. In figure 2.14 the setup of the chamber is shown. Before usage, the chamber was thoroughly rinsed with ultrapure water. For neutron measurements, a new microfluidic chamber was designed, as described in chapter 3.

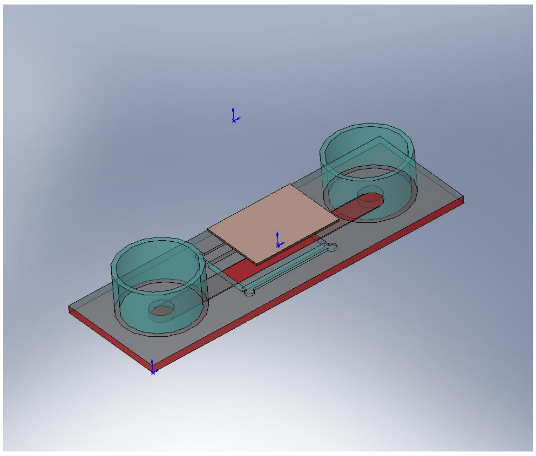

Figure 2.14: Modified IBIDI chamber used for x-ray and microscopy measurements. A cavity is drilled into the microfluidic chamber above the microfluidic channel (*red*) that holds the silicon surface (*ocre*). The figure was kindly provided by Martin Huth.

2.5.6 Calculation of theoretical electron density profiles

The overall volume of a POPC lipid is assumed to be 1257 Å^3 as described in [114]. With a bilayer thickness of 40 Å and thus 20 Å for each leaflet this leads to an average lipid area of 63 Å^2. The volume fractions of the lipid components obtained from molecular dynamics simulations of POPC are as described in [114]: the volume for the carbonyl and glycerol group is 149.3 Å^3, the volume for the phosphate and choline group is 172.8 Å^3, each methylene group has a volume of 28.24 Å^3 and the methyl termini have a volume of 50.4 Å^3 each. Counting the number of electrons per group leads to the following electron densities: 0.561 e$^-$/Å^3 for the phosphate and choline group 0.4486 e$^-$/Å^3 for the carbonyl and glycerol group 0.283 e$^-$/Å^3 for the methylene chain and 0.179 e$^-$/Å^3 for the methyl termini. To obtain the thickness of each chemical group in z-direction, the volume of the group was divided through the lipid area. For pure PCb bilayers the width of the attached bromine label is estimated to be 4 Å [115]. The area per lipid chain is 31.5 Å^2, leading to a volume of 125.7 Å^3 for the chain part with attached bromine label. With these assumptions the electron density of the bromine label is calculated to be 0.652 e$^-$/Å^3. With an electron density of 0.283 e$^-$/Å^3 of the pure methylene chain, the overall electron density is calculated as $\rho_{\mathrm{chainBr}} = (0.283 + 0.652)/2$ e$^-$/Å^3 = 0.4675 e$^-$/Å^3. The electron density profile of a 75 % PCb and 25 % POPS containing bilayer is calculated by: $\rho_{\mathrm{mix}}(\mathrm{z}) = 0.75 \times \rho_{\mathrm{PCb}}(\mathrm{z}) + 0.25 \times \rho_{\mathrm{POPS}}(\mathrm{z})$. Here, z describes the distance perpendicular to the bilayers surface, $\rho_{mix}(z)$ describes the mixed electron density profile, $\rho_{PCb}(z)$ the electron density profile of a pure PCb containing bilayer and $\rho_{POPS}(z)$ the electron density profile of a pure POPS containing bilayer. All simulations are perfomed with Matlab (MATLAB, The MathWorks, Inc.).

2.5.7 Decomposition of electron density profiles

To extract quantitative information about the spatial dimensions of the protein layer and to study possible changes in the SLB, the electron density profiles were analyzed in more detail. To this end, the electron density profiles were divided into several component groups of the lipid bilayer and the Anx A2t complex, similar to [116, 117]. These groups contribute additively to the total electron density: two Gaussian functions were used for the headgroup (phosphate + Ca^{2+} + serine/choline) and the backbone (glycerol + carbonyl group), two error functions were used for the alkyl chains and one Gaussian function for the chain termini (methyl groups) of both leaflets. The areas of all groups were fixed to the stoichiometric ratios of their electron numbers, such that only the total area per lipid of each leaflet, the width and the position of each group were fitting parameters. In addition, the area per lipid of each leaflet was constrained to values above 40 $Å^2$/lipid, since film balance measurements of PS lipids in calcium buffer revealed this value as an empirical minimum for their area fraction. Silicon substrate and water are each represented by an error function. The silicon substrates roughness was adjusted to the value of 4 Å obtained by independent measurements of the bare wafers and was kept constant during the fitting process. Anx A2t is represented by 6 error functions, where 2 error functions represent the p11 dimer and 4 error functions account for the hydrophilic and hydrophobic domains of the Annexin monomer, respectively. The thickness of the protein layer was calculated by the half-maximal width of the two enveloping error functions.

The parameters of the decomposition are estimated by using a trust-region reflective Newton method (MATLAB, The MathWorks, Inc.) to minimize the total χ^2. To quantify the uncertainty in the estimated parameters, 10 000 independent fits are performed with randomly chosen initial parameter sets (within their physiological ranges). This implies the constraint that the spatial order of the components has to be maintained, i.e., permutation of the individual groups are not allowed. The errors with respect to the optimal parameters are computed as described in ref. [118]. The squared error for parameter τ_k is calculated using the following equation:

$$\sigma_k^2 = \frac{\sum_{\tau_{k,i}} (\tau_{k,i} - \tau_k^{opt})^2 e^{-\chi_i^2/2}}{\sum_{\tau_{k,i}} e^{-\chi_i^2/2}} \,. \tag{2.51}$$

Here $\tau_{k,i}$ is the value of parameter τ_k in the i_{th} fit, τ_k^{opt} is the value of τ_k in the fit with the lowest value of χ^2, and χ_i^2 is the value of χ^2 for the i^{th} fit. In using the likelihood function $e^{-\chi^2/2}$, it is assumed that the errors in the measurements are independent and normally distributed with widths equal to the standard error of the mean.

2.5.8 Calculation of the volume fractions of mixed layers

The overall electron density or scattering length density (SLD) of a mixed layer can be written as weighted sum of the electron or SLDs of its single components, that is,

$$\rho_{mix} = \sum_i x_i \rho_i \,. \tag{2.52}$$

Here ρ_i is the electron density or SLD of the single components and x_i the volume fractions of the single components. With Eq. (2.52) the electron density of the total protein layer ρ can be written as a weighted sum of the electron densities of pure protein ρ_{prot} and pure water ρ_{H_2O}, i.e., $\rho = x\rho_{prot} + (1-x)\rho_{H_2O}$ where x and $(1-x)$ are the volume fractions of the protein and water, respectively. As approximation for the total protein layer coverage the maximal electron density in the Anx A2 signature is used and compared to the electron density of the pure protein. The electron density of the pure protein is calculated from the chemical sum formula obtained for Anx A2t bovine with ExPASy Proteomics Server [119]. The mass density of Anx A2 is given by $\rho_m = [1.41 + 0.145e^{(-M/13)}]$ g/cm^3, as described in ref. [120]. Here M is the molecular mass of Anx A2 in kDa, leading to a mass density of $\rho_m = 1.418$ g/cm^3. With this, the electron density of Anx A2 is obtained as $\rho_{prot} = 0.458$ e$^-$/Å^3 while the electron density of bulk water is given by $\rho_{H_2O} = 0.336$ e$^-$/Å^3. For neutron scattering a SLD of 1.88 10^{-6} Å^{-2} for Anx A2t is obtained.

2.6 Sample preparation

Chemicals. 1-Palmitoyl-2-oleoyl-sn-glycero-3-phosphocholine (POPC), 1-palmitoyl-2-oleoyl-sn-glycero-3-[phospho-L-serine] (Sodium Salt) (POPS) and 1,2-distearoyl (dibromo)-sn-glycero-3-phosphocholine (PCb) were bought from Avanti Polar Lipids Inc.(Alabaster USA) and used without further purification. In figure 2.15 the structure formular of the used lipids is shown. Texas Red 1,2-dihexadecanoyl-sn-glycero-3-phosphoethanolamine, triethylammonium salt (Texas Red DHPE) and Oregon Green 488 1,2-dihexadecanoyl-sn-glycero-3-phosphoethanolamine (Oregon Green 488 DHPE) were bought from Invitrogen Molecular Probes (Eugene USA). Chloroform, methanol ethanol and acetone were bought at HPLC grade from Carl Roth GmbH & Co (Karlsruhe, Germany). Tris-(hydroxylmethyl)-aminomethane (TRIS), phosphate buffer saline (PBS) $CaCl_2$, NaCl, ethylene- diamine-etraacetic- acid (EDTA), ethylene glycol-bis(2-aminoethylether)-N,N,N',N'-tetraacetic acid (EGTA), DL-dithiothreitol (DTT), hydrogen peroxide, and NH_4OH were bought from Sigma Aldrich (Taufkirchen, München) at a purity of 99.5 %. Only freshly bidistilled water (18.2 MOmega Millipore, Billerica, USA) was used. Silicon wafers cut into pieces of 20x15 mm^2 and an oxide thickness of 20, 50 and 100 nm were bought from CrysTec GmbH (Berlin, Germany) Silicon blocks of size 200x150x100 mm^3 were bought from Siliciumbearbeitung Andrea Holm (Gigerenz, Germany) and oxidised to an oxide thickness of 100nm in an rapid thermal anneal (RPT) oven.

Wafer cleaning. In a first step the wafers were ultrasonicated for at least three minutes, first in aceton then in ethanol followed by three minutes ultrasonification in ultrapure water. Subsequently, a mixture of 1:1:5 (HCl:H_2O_2:H_2O) was prepared and the wafers were boiled in this solution on a hot plate, set to 150 °C. Afterwards, the wafers were rinsed with ultrapure water and heated in a 1:1:5 (NaOH: H_2O_2:H_2O) solution for two hours while the hotplate was set to 90 °C. The silicon surfaces were thoroughly rinsed with ultrapure water and directly used for vesicle spreading.

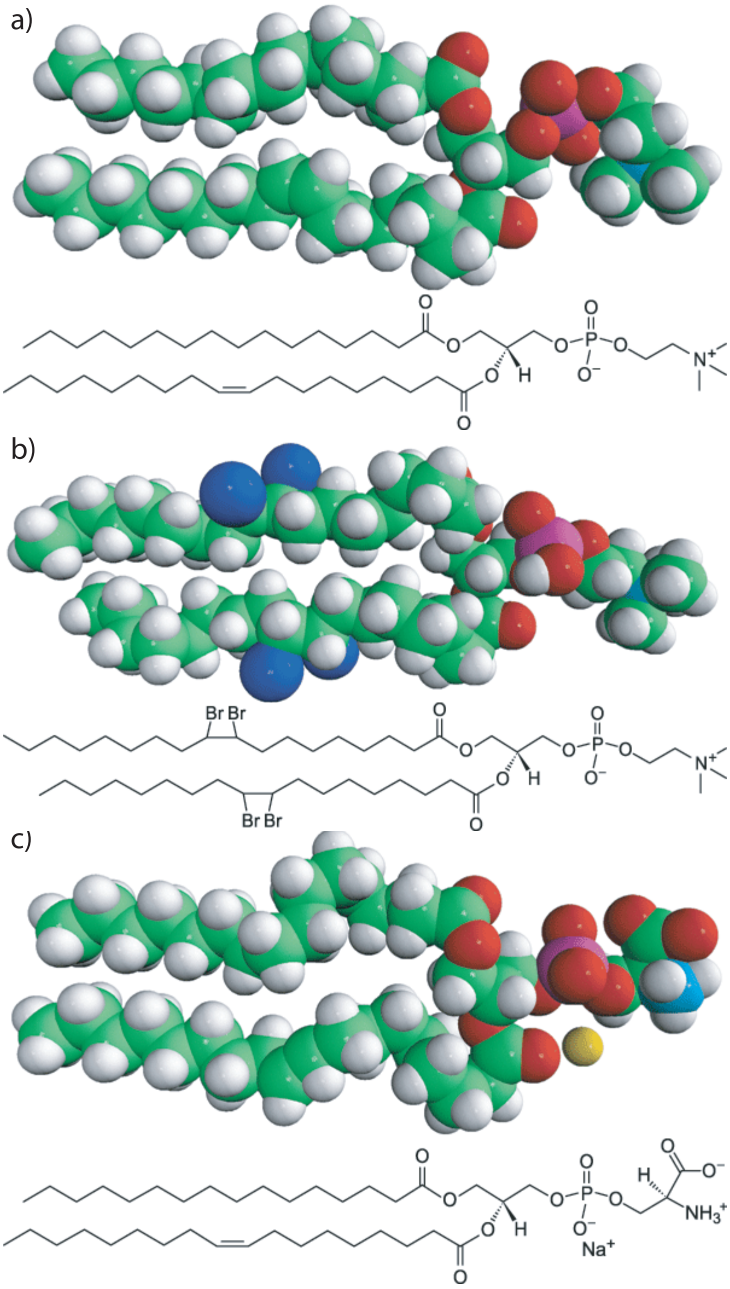

Figure 2.15: Structure formula of (*a*) POPC (*b*) PCb and (*c*) POPS.

Buffers. All buffers were sterilised by autoclaving or filtering through sterile filters with a pore size of 20 µm before usage.

- *Buffer A:* 100mM PBS 1M NaCl at pH 7.4
- *Buffer B:* 20mM TRIS HCl 100mM NaCl 0.5mM DTT 1mM $CaCl_2$ at pH 7.4
- *Buffer C:* 20mM TRIS HCl 100mM NaCl 10mM EGTA at pH 7.4
- *Buffer D:* 20mM MES, 100mM NaCl 0.5mM EGTA at pH 6

Vesicle spreading. Surface supported bilayers of varying molar composition of POPC and POPS or DiBrPC and POPS were prepared on the silicon substrate by the following procedure, appropriate amounts of lipids were dissolved in Chloroform and filled in a clean glass vial. For fluorescence microscopy, 0.5 mol% fluorescent dye Texas Red DHPE or Oregon Green 488 DHPE were added to the mixture. The solvent was evaporated by a nitrogen flow while rotating the glass vial, so that a thin lipid film formed on the glass. After additional overnight evaporation in a dessicator connected to a rotary vacuum pump, the mixture was dispersed in buffer A to a lipid concentration of 1 mg/ml and was vortexed to a milky solution. This solution was kept at 40 °C for two hours. Small unilamellar vesicles were obtained by extrusion through 100 nm filters using an Avanti Extruder. The microfluidic chamber was first rinsed with buffer A and 150 µl of the vesicle solution were injected into the microfluidic chamber covering the silicon. The sample was incubated for at least three hours at room temperature. Then the sample was rinsed intensively with the same buffer to remove excess vesicles, and controlled with fluorescent microscopy for homogenous vesicle coverage. At this stage of sample preparation the surface is covered by lipid vesicles which do not spread spontaneously due to their high PS content. In a following step the buffer was carefully exchanged with deionized pure water, injected into one of the two outlets. The surface was controlled with fluorescent microscopy. When homogenous bilayer coverage was reached, buffer C was injected. Surface supported bilayers to a concentration of 50 mol % POPS could be gained by this method.

Protein incubation. The protein Annexin II Tetramer (A2T) was stored in buffer D at -20 °C. Before usage, the protein solution was carefully heated onto 4 °C in an ice bath and 1 ml of buffer B was carefully added to the protein solution. The solution was further diluted to a concentration of 3 to 6 µM protein concentration. Surface supported bilayers were incubated by injecting 150 µl of the protein solution into the microfluidic chamber. The bilayers were incubated for at least three hours at room temperature. Afterwards the samples were rinsed with buffer B to remove excess protein.

Chapter 3

Results

In pure water, the spreading of negatively charged lipids on silicon supports is hindered by electrostatic repulsion between the support and the lipid bilayer. Thus, in this thesis a new method to form bilayers inhabiting negatively charged PS lipids is developed and introduced in section 3.1. Electrostatic forces may influence bilayer structure and lipid distribution among the leaflets. One aim of the following experiments is to reveal the influence of buffer condition and surface on the structure and lipid distribution of surface supported lipid bilayers (SLBs). In section 3.2.2 neutral and negatively charged SLBs are investigated in water with means of x-ray reflectivity. Furthermore, lipid derivatives with an attached bromine label allow to directly visualize the lipid composition in each bilayer leaflet. It is known that divalent salt ions have a profound influence on the physical state of PS containing bilayers. In section 3.2.3 the structural changes of zwitterionic and negatively charged bilayers upon adding calcium are examined. These x-ray investigations are complemented in section 3.2.4 by a comparison of lipid diffusion in neutral and zwitterionic bilayers. Protein binding may lead to changes in the phase behavior of lipid bilayers. In section 3.3, the influence of the binding of the protein Annexin II on bilayer structure and mobility is investigated. Furthermore, the arrangement of the bound tetrameric and monomeric complex is resolved from the density profile of the attached protein layers.

3.1 Vesicle spreading of negatively charged lipids on silicon supports

Since the overall forces between acidic negatively charged vesicles and negatively charged silicon surfaces is repulsive in pure water, a method to shield the electrostatic repulsion has to be used to induce spreading. The standard method to form such bilayers is to use calcium-containing buffers [24]. Calcium leads to the formation of domains of PS lipids that differ in height from the surrounding PC lipids, and thus increases the hydrophobicity of the vesicles. This leads to the opening of phospholipid vesicles in contact with silicon supports [121]. Furthermore, calcium dehydrates the phosphate group of phospholipids (see also chapter 2.1) and thus leads to a close contact of the bilayer with the silicon oxide

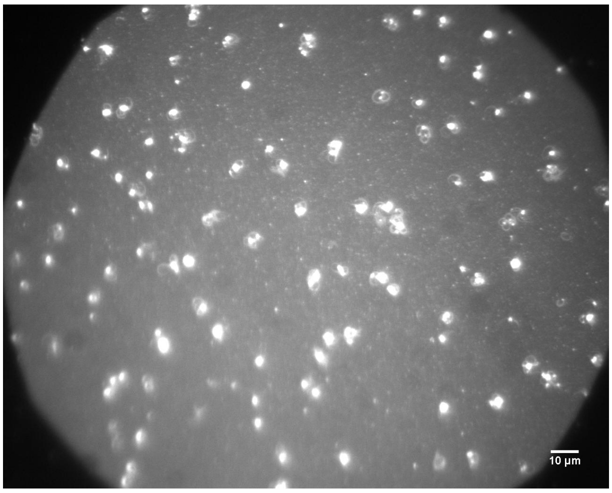

Figure 3.1: Lipid multilayers on negatively charged surface supported bilayers in calcium containing buffer.

surface [122], [123]. However, fluorescence microscopy and x-ray reflectivity revealed the formation of multilayers on top of the bilayer upon using calcium-containing buffer. In figure 3.1 the fluorescence microscopy image of a bilayer, formed from negatively charged phospholipid vesicles in calcium-containing buffer is shown. The white structures on top of the bilayer are lipid multilayers that cannot be removed even through excessive rinsing with pure water.

It is known that calcium bridges POPS lipids [110]. The multilayers on top of the bilayer are presumably due to POPS lipids forming calcium bridges among themselves. To circumvent this problem, a new method to form single supported negatively charged bilayers on silicon supports is developed described in the following section.

3.1.1 Vesicle spreading of negatively charged phospholipids

To screen the electrostatic repulsion between silicon surface and negatively charged POPS /POPC lipids, a buffer with high monovalent salt concentration is chosen. An exact description of the used buffer is given in section 2.6 (buffer A). Figure 3.2*a* shows a fluorescence microscopy image of a silicon support after incubation with negatively charged vesicles in buffer solution. Vesicles that are prepared in 1M sodium-containing buffer settle onto the silicon surface and form a homogenous vesicle film. However, they do not open to form a fluid bilayer, as revealed by the homogenous intensity profile developing upon continuous photobleaching (see figure 3.2*b*, *c*).

To open up the vesicles and form a homogenous bilayer, an additional force has to be applied. Reimhult *et. al.* have shown that vesicle spreading is facilitated by osmotic pressure [124]. To apply an osmotic pressure onto the vesicle film, the samples are rinsed with pure water. The high osmotic pressure between buffer inside the vesicle and water

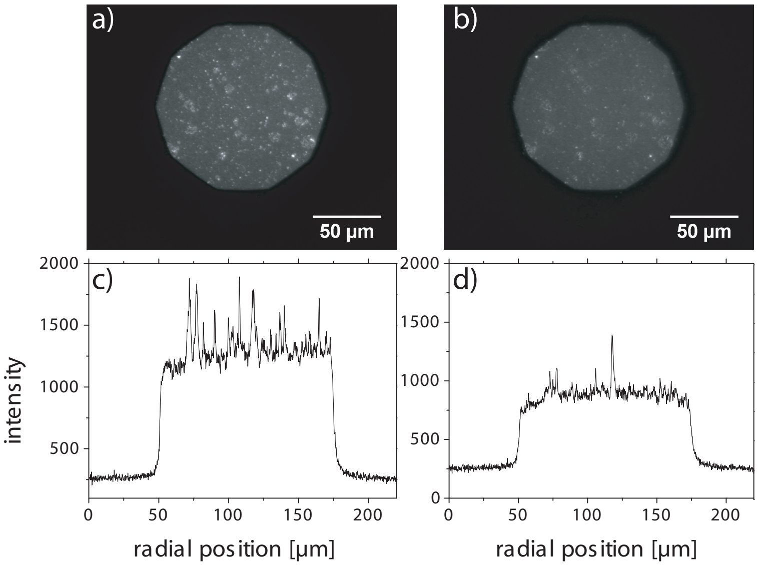

Figure 3.2: Fluorescence microscopy image of a homogenous layer of negatively charged lipid vesicles on silicon before (*a*) and after continuous bleaching (*b*). The corresponding linear intensity profiles are shown in (*c*) and (*d*).

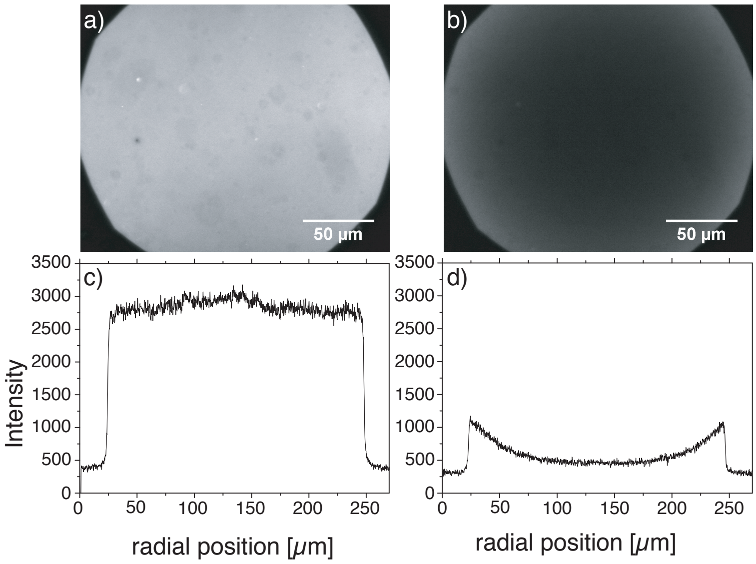

Figure 3.3: Fluorescence microscopy image of a negatively charged surface supported membrane formed by vesicle spreading with osmotic pressure, before (*a*) and after continuous bleaching (*b*). The white rim in (*b*) indicates fresh unbleached lipids diffusing into the aperture area. The corresponding linear intensity profiles are shown in (*c*) and (*d*).

outside the vesicle leads to an opening of the vesicles. Figure 3.3 shows the fluorescence microscopy image of such a membrane before (figure 3.3*a*) and after bleaching (figure3.3*b*) of the fluorescent dye in the aperture area. The white rim, developing upon bleaching as well as the higher intensity of the line profile (see figure 3.3*c* and *d*), indicate freshly unbleached fluorescent labeled lipids diffusing into the aperture area [103].

With the method of vesicle spreading by osmotic pressure, a coverage of the silicon surface with defect-free and fluid surface supported negatively charged bilayers up to a concentration of 50 mol% of negatively charged lipid is obtained.

3.2 Structure and mobility of negatively charged bilayers

The method of vesicle spreading with osmotic pressure leads to defect-free fluid supported bilayers. However, the structure of the bilayer and the distribution of negatively charged lipid in both leaflets may be influenced by the forces between surface and bilayer that are described in chapter 2.1. In the following section the influence of the surface, buffer solution and charge of the bilayer on the structure and mobility of the bilayer is investigated with x-ray reflectivity (XR) and fluorescence microscopy. With XR, information about the electron density profile perpendicular to the surface is obtained. A major advantage of XR is that also electron density profiles of buried structures, for example the profile of the leaflet of the bilayer proximal to the silicon, remains experimentally accessible.

The diffusion of lipid probes in a bilayer may reveal the change in the physical state of the bilayer. Therefore, the method of continuous bleaching is used to identify changes in lipid mobility upon adding calcium (see section 3.2.4) and binding of the protein Anx A2t (see section 3.3). For data evaluation a new tool is introduced in section 3.2.4

3.2.1 Theoretical electron density profiles of surface supported bilayers

To clarify the influence of instrumental resolution and thermal undulation on electron density profiles of lipid bilayers, a simulation of the used bilayers is performed. Of particular interest is, whether a brominated POPC derivative (PCb) allows for the detection of structural asymmetries between both bilayer leaflets. Such asymmetries may be induced by an enrichment of negatively charged POPS in one of the leaflets. It has been shown before that PCb lipids form bilayers in water [115]. Furthermore, PCb was used to resolve the binding sites of membrane proteins in x-ray scattering experiments [125]. In these experiments it was shown that PCb does not influence protein binding. For the chemical composition of the molecule please refer to figure 2.15. The following simulation clarifies the available information about the distribution of the bromine label in both bilayer leaflets.

At room temperature thermal agitation of lipid bilayers stacks may lead to an undulation amplitude up to 10 Å [126]. To simulate the effect of undulation, all electron density

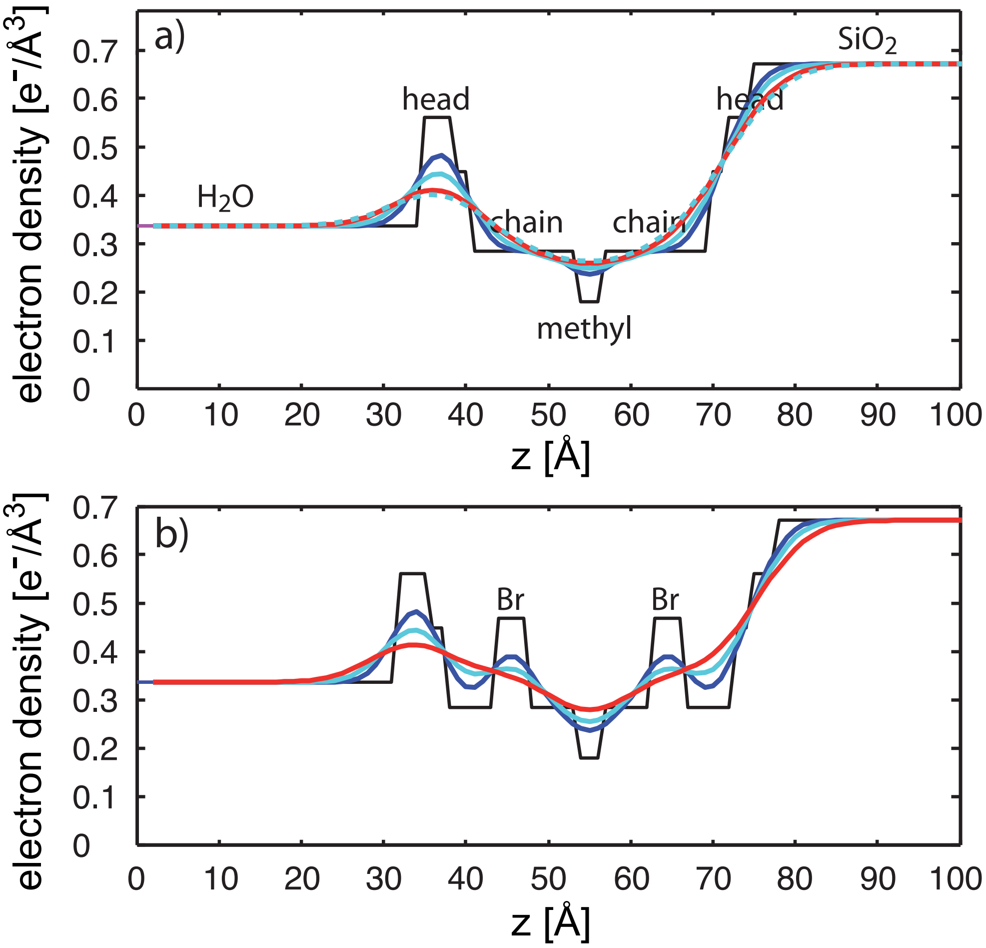

Figure 3.4: Calculation of the electron density profile of a POPC (*a, black curve*) and a PCb bilayer (*b, black curve*) exhibiting a bromine group volume of 125.7 Å^3 corresponding to a bromine width of 4 Å. The theoretical electron density profiles are convolved with a gaussian of width 10 Å (*red curves*) or a gaussian of width 5 Å (*blue curves*), to account for thermal undulation. In a subsequent step both profiles are convolved with a gaussian of 5 Å width (*a, cyan curves*) to account for instrumental resolution. In (*b*) only the profile, accounting for a thermal undulation of 5 Å amplitude (*blue curve*) is convolved with the instrumental resolution in a subsequent step.

profiles (*black curves*) in figure 3.4 and figure 3.5 are convolved with a gaussian of 10 Å width (*red curves*). For surface supported bilayers the undulation amplitude is lower due to the binding potential of the substrate [127]. Therefore, all theoretical profiles are also convolved with a gaussian of 5 Å width (*blue curves*) for comparison. At ID01 the maximum momentum transfer of the measurement leads to an instrumental resolution of 5 Å. Thus, the obtained profiles are convolved with a gaussian of 5 Å width (*cyan curves*), in a subsequent step.

In figure 3.4 the theoretical electron density profile of a surface supported POPC bilayer (*a, black curve*) and the profile of a PCb bilayer (*b, black curve*) with a bromine width of 4 Å as described in [115] are shown (for details please refer to section 2.5.6). Thermal agitation leads to a smearing out of the profiles, which is more pronounced for an undulation amplitude of 10 Å (*red curves*) as compared to an undulation amplitude of 5 Å (*blue curves*). Experimental uncertainty leads to a further smearing out of the profiles (*cyan curves*). However, in the case of a high undulation (10 Å) amplitude the uncertainty due to instrumental resolution does not change the profiles to an appreciable degree (see figure 3.4*a, cyan dotted curve*). Therefore, in all following simulations it is omitted. In all final profiles, the phospholipid headgroup distal to the silicon surface is clearly visible, while the headgroup proximal to the silicon surface is hidden in the decrease of the silicon density to the density of the methylene chain region. In the case of 5 Å thermal undulation, resulting in the electron density profile shown in figure 3.4 (*blue curves and cyan curves*), the methylene chain region is clearly distinguishable from the low electron density of the methyl ends of the lipid chain region. In contrast, at 10 Å thermal undulation, resulting in the electron density profiles in figure 3.4 (*red curves and cyan dotted curve*), the methylene chain region exhibits a smooth descent to the methyl ends and is inseparable from the methyl ends of the lipid chains. The theoretical electron density profile of a PCb bilayer (figure 3.4*b, black curve*) exhibits an increase in electron density in the methylene chain region as compared to the theoretical profile of the POPC bilayer (figure 3.4*a, black curve*). This change in electron density is due to the attached bromine label. The final electron density profiles of a PCb bilayer (figure 3.4*b, cyan and red curve*) exhibit for both undulation amplitudes a higher electron density in the methylene chain region than the pure POPC bilayer and a less steep decrease from the headgroup to the methyl ends of the bilayer. This change in electron density as compared to the POPC bilayer, is due to the attached bromine label. Both simulations thus indicate that the label is visible in the formed bilayers.

In figure 3.5 the effect of an asymmetric distribution of brominated lipid is simulated as compared to a symmetric 25% POPS 75% PCb bilayer (*a*). In figure 3.5*b, black curve*, the theoretical electron density profile of a bilayer consisting of pure PCb in the distal leaflet and pure POPS in the proximal leaflet is shown. In figure 3.5*c, black curve* the theoretical electron density of a bilayer consisting of pure PCb in the proximal leaflet and pure POPS in the distal leaflet is shown. Again instrumental resolution and thermal agitation lead to a smearing out of the theoretical profiles, more pronounced for an 10 Å undulation amplitude (*red curves*) as compared to an undulation of an amplitude of 5 Å (*cyan* and *blue curves*). The bromine label in only one leaflet leads to a distinct increase in electron density in the methylene chain region of the bromine containing bilayer leaflet

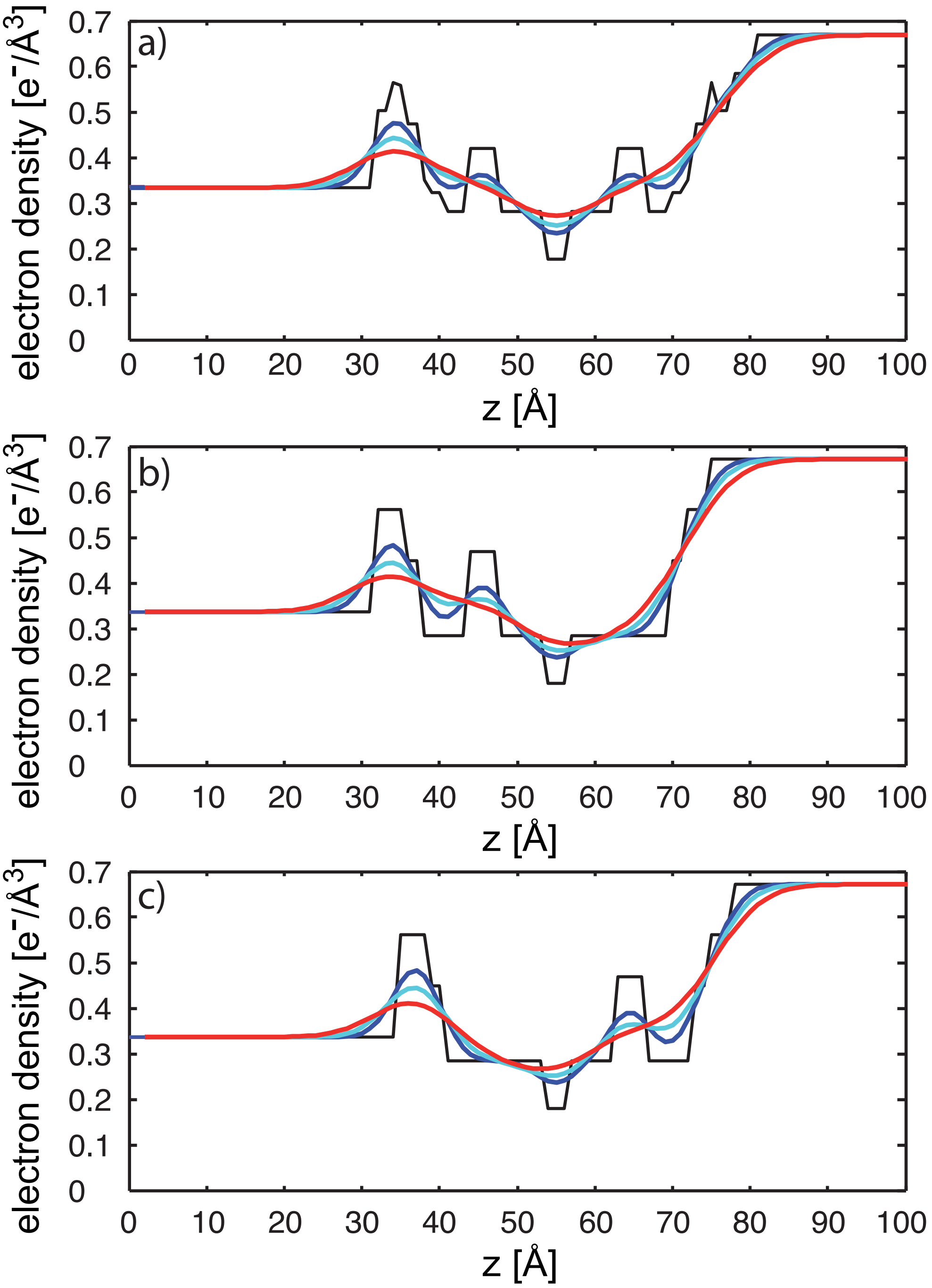

Figure 3.5: Theoretical electron density profile of a symmetric bilayer with an amount of 75% PCb and 25% POPS in both leaflets (*a, black curve*), a bilayer consisting of pure PCb in the distal leaflet and pure POPS in the proximal leaflet (*b, black curve*) and a bilayer consisting of pure PCb in the proximal leaflet and pure POPS in the distal leaflet (*c, black curve*). The theoretical electron density profiles are convolved with a gaussian of width 10 Å (*red curves*) or a gaussian of width 5 Å (*blue curves*) to account for thermal undulation, and a gaussian of width 5 Å (*cyan curves*), to account for instrumental resolution.

in all resulting curves (*cyan* and *red curves*). The simulation reveals that it is possible to resolve the bromine label independently in both leaflets. Thus, it is possible to estimate the amount of brominated lipid as compared to the amount of POPS lipid in both bilayer leaflets independently.

3.2.2 Structure of lipid bilayers in water

In the following the structure of bilayers with different composition of negatively charged lipids in pure water is investigated with x-ray reflectivity. Figure 3.6 shows the reflectivity data of a pure POPC bilayer (*I*) and a 25% POPS 75% POPC containing bilayer (*II*) in MilliQ water. Furthermore, the reflectivity data of a pure PCb containing bilayer (*III*) and a 75% PCb 25% POPS containing bilayer (*IV*) is shown. The increase in intensity for $q \leq 0.02$ Å^{-1} is due to total reflection at the silicon surface and a q^4 correction, as described in section 2.5.3. The rapid intensity oscillations (Kiessig fringes) show a periodicity of $\Delta q = 0.016$ Å^{-1}. These narrow fringes stem from the interference between the reflections at the silicon oxide layer and the silicon substrate. In contrast, the broad Kiessig fringes with $\Delta q = 0.16$ Å^{-1} for the pure POPC bilayer and $\Delta q = 0.14$ Å^{-1} for the 25% POPS containing bilayer have been shown to result from the Surface supported bilayer (SLB) [109, 26]. The x-ray reflectivity data of all datasets are evaluated with varying starting parameters using Abeles algorythm [107] as described in section 2.5.4. In figure 3.7*a*, an example of the data evaluation is shown for a POPC bilayer in pure water. Shown are the 15 electron density profiles (*grey curves*) with the lowest χ^2, all fitting the reflectivity data in figure 3.6 (*I*). From these profiles, an average electron density is calculated (*black curve*), and smoothed by the instrumental resolution of 5 Å (*red curve*). The resulting electron density profile (*red curve*) exhibits the typical shape of a surface supported lipid bilayer [109, 128, 129]. Lipid head and chains distal to the substrate as well as the hydrophobic part of the bilayers are clearly visible [109]. The headgroup proximal to the silicon surface is not visible in the profiles (*red curve*) as expected from the simulations in figure 3.4. To obtain information of the packing of the lipids for both bilayer leaflets independently, the averaged electron density profile is now decomposed into its chemical component groups, as described in [117]. In figure 3.8, the chemical structure of the lipids and the chemical groups for the decomposition are shown. These groups contribute additively to the total electron density profile. Two gaussian functions were used for the headgroup, one gaussian for the phosphate and choline group (figure 3.8, *cyan*) for pure POPC bilayers or phosphate + serine (figure 3.8, *dark cyan*) for the mixed bilayers, respectively. A second gaussian is used for the backbone's glycerol and carbonyl group (figure 3.8, *green*). Two error functions are used for the alkyl chains (figure 3.8, *black*) and one gaussian function for the chain termini (methyl groups) (figure 3.8, *orange*) of both leaflets. For lipids containing a bromine label in their methylene chain region one gaussian, accounting for the C_2Br_2 group (figure 3.8, *blue*) is added. The areas of all groups are fixed to the stoichiometric ratios of their electron numbers (see figure 3.8), such that only the total area per lipid of each leaflet, the width and position of each group, and the amount of brominated lipid are fitting parameters. The ratio of serine to choline group is kept at the stochiometric

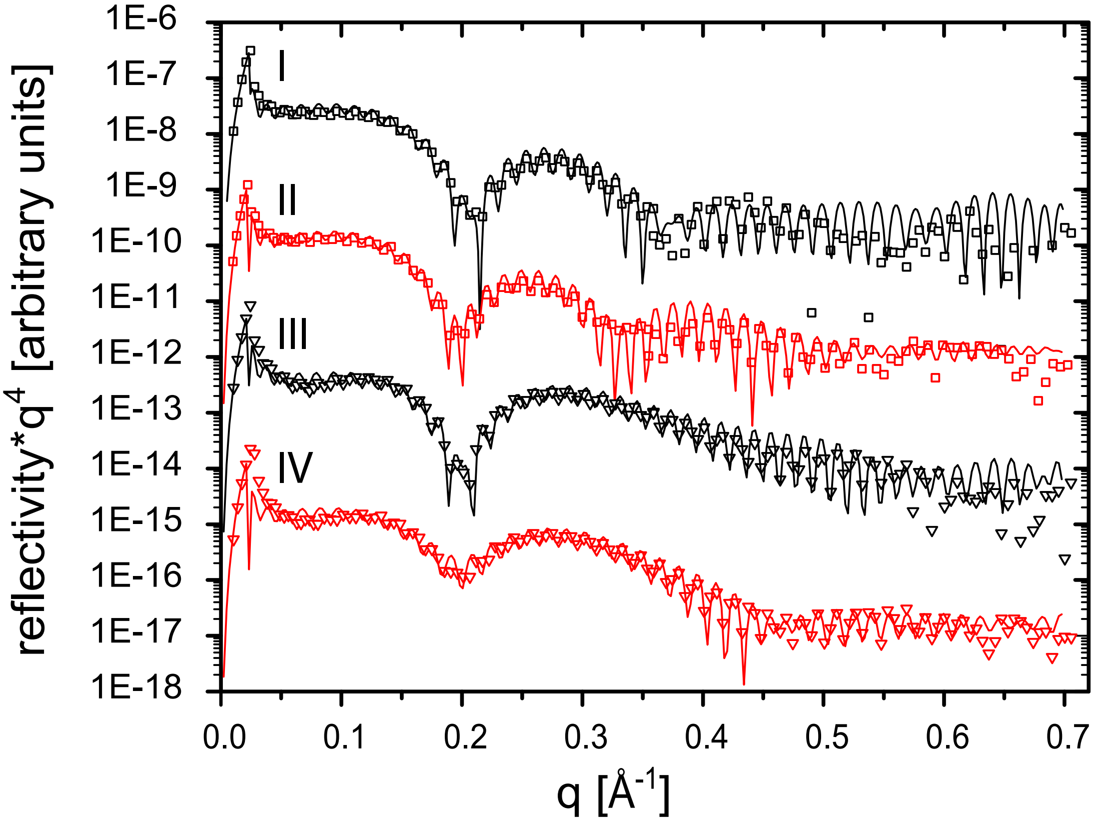

Figure 3.6: X-ray reflectivity data and best fit to data of a pure POPC (*I*), a 25% POPS 75% POPC (*II*), a pure PCb (*III*) and a 25% POPS 75% PCb (*IV*) containing bilayer, in pure water. The lines represent the best fit to the data.

ratio of the mixture. Silicon substrate and water are each represented by an error function. The silicon substrate roughness is adjusted to the value of ≈ 4 Å obtained by independent measurements of the bare wafers and is kept constant during the fitting process.

As an example, the decomposition of the electron density profile of a POPC bilayer is shown in figure 3.7*b*. 10000 fits were initialized with random seed parameters, and the best 1000 fits to the electron profile are shown in figure 3.7*b*. The decomposition of the profile leads to three stable fit parameters, namely, the area per lipid for proximal and distal leaflet and the thickness of the bilayer (see table 3.1). With this information it is possible to resolve the influence of the surface, bilayer charge and buffer condition on each leaflet separately.

Figure 3.9 shows the electron density and the best fit (*red line*) of the decomposition of the electron density profile of a pure POPC (*a*) and a 75% POPC 25% POPS containing bilayer (*b*) in pure water. Both electron density profiles (*red curves*) feature the typical shape of a surface supported bilayer [109, 128, 129]. The phosphate group of the lipid headgroup gives rise to a distinct increase in electron density adjacent to the buffer solution, in both profiles. Furthermore, the low electron density of the lipid chains leads to a decrease in electron density in the hydrophobic part of the bilayer [109]. In both profiles, the headgroup proximal to the silicon surface is not visible, yet, the decomposition into chemical components reveals that they are present in the decays of the substrates. Table 3.1 summarizes the thicknesses and areas per lipid of each leaflet for all bilayer compositions in pure water. All bilayers show the same thickness of 39 Å within error, in perfect agreement with previous measurements [116]. Furthermore, no difference in area per lipid in the distal leaflet as compared to the proximal leaflet is found. However, the POPC bilayer exhibits a higher packing density in both leaflets than the 25 % POPS 75 % POPC containing bilayer. This is presumably due to the negatively charged POPS lipids repelling each other, leading to an increase in the overall area per lipid.

To further investigate the distribution of lipids in the proximal and distal leaflet, a PC derivative with a chemical bound bromine label (PCb) is used. In figure 3.6 the reflectivity data of a pure PCb bilayer (*III*) and a 75% PCb 25% POPS (*IV*) containing bilayer are shown. The reflectivity data of bilayers with attached bromine label exhibit broader Kiessig fringes as compared to the data of unlabeled bilayers, due to a superposition of the signals of the bromine label and the bilayer chains.

The reflectivity data are analysed as described in section 2.5.4. The chemical decomposition of the profiles is perfomed as described above. Figure 3.10 shows the electron density profile and decomposition fits of a pure PCb and a 25% POPS 75% PCb bilayer in pure water. In the 25% POPS 75% PCb bilayer, the proximal leaflet exhibits an increase in electron density in the methylene region as compared to the distal leaflet. Furthermore, the profile resembles the simulation of a POPS PCb bilayer with a high amount of PCb in the proximal leaflet (see figure 3.5, *cyan curve*). Thus, either the proximal leaflet of the bilayer contains more PCb than the distal leaflet or the proximal leaflet exhibits a higher lipid order than the distal leaflet. In table 3.1 the bilayer thicknesses and areas of distal and proximal leaflet are summarized. The pure PCb bilayer displays an area per lipid of 80 ± 3 Å^2 in both leaflets. Both bilayer leaflets of the 25% POPS 75% PCb bilayer exhibit

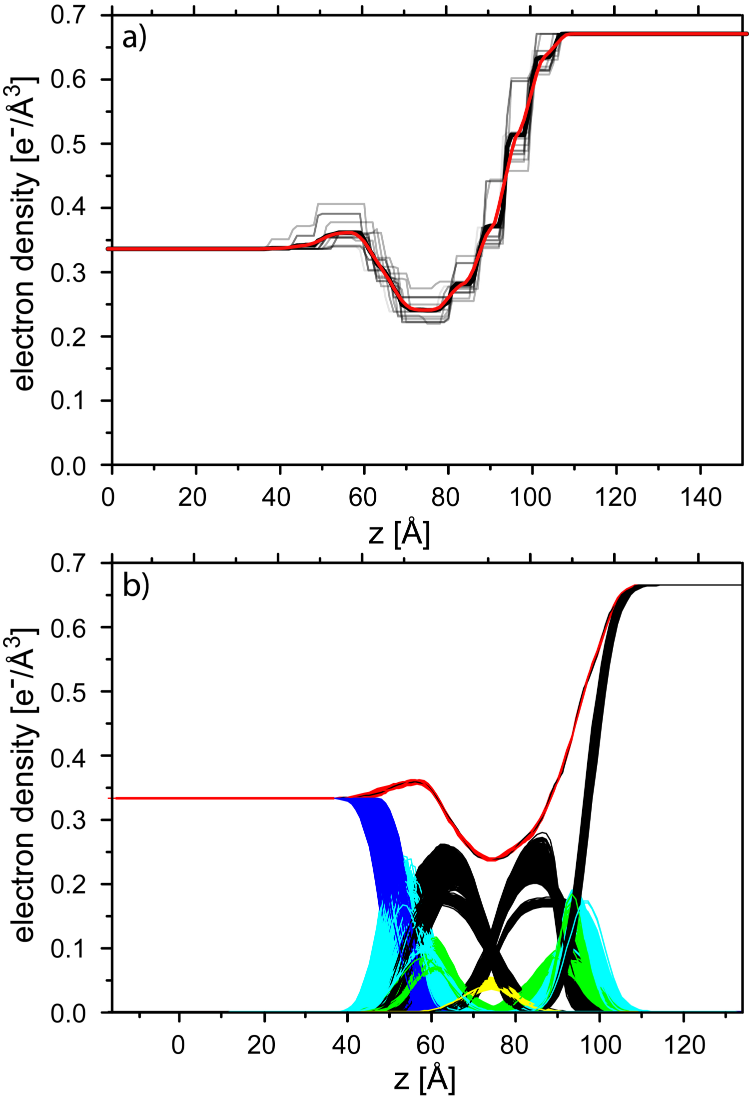

Figure 3.7: (*a*) 15 best electron density fits (*grey lines*) calculated weighted mean (*black line*) and smoothed weighted mean (*red line*) to the data of a pure POPC bilayer in water. (*b*) Best 1000 chemical group decomposition fits to obtained electron density profile of a POPC bilayer in pure water. Turquoise gaussians describe the phosphate and choline group, green gaussians the carbonyl and glycerol groups and yellow gaussians the methyl groups of both leaflets. The black lines describe the alkyl chains. Furthermore the water distribution (*blue lines*) and substrate distribution (*black error functions*) are clearly visible for each fit.

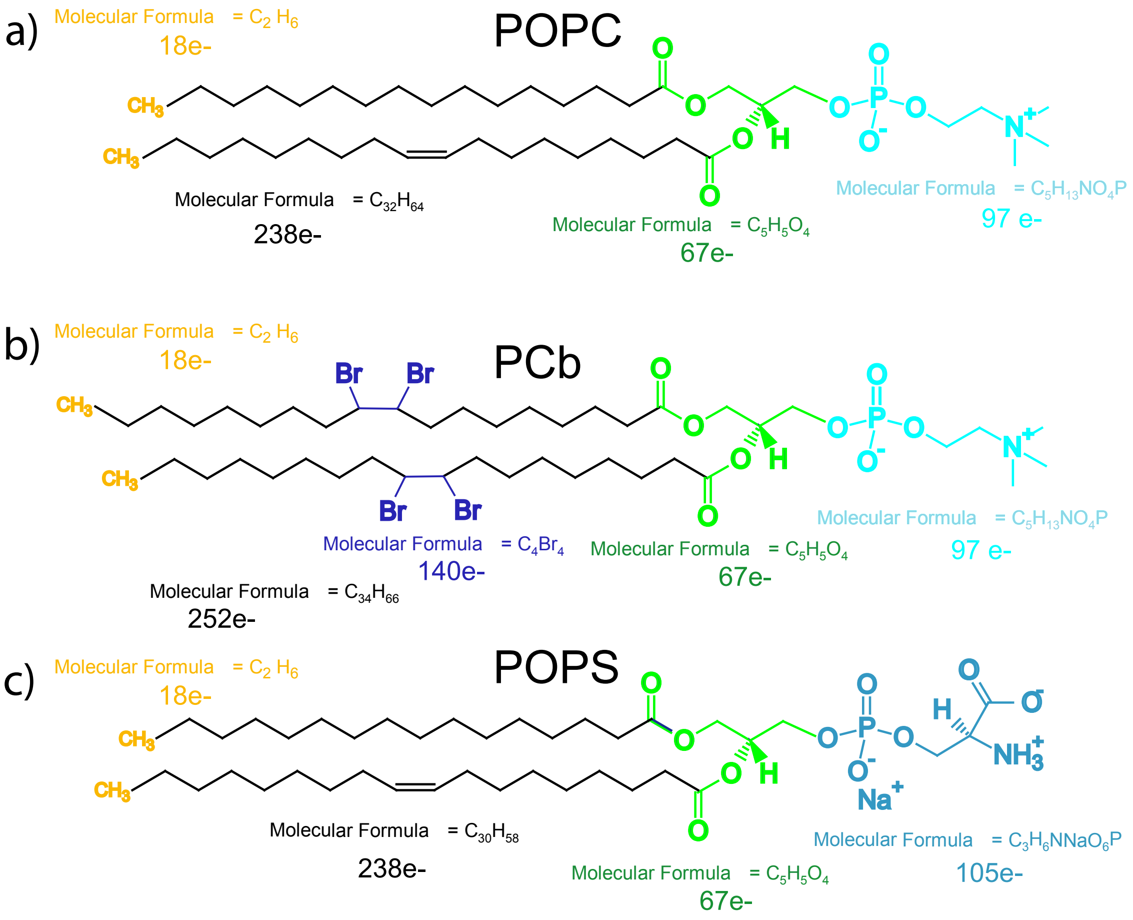

Figure 3.8: Chemical composition and electron number of chemical compounds as used for chemical decomposition fits. (*a*) POPC, (*b*) PCb, (*c*) POPS.

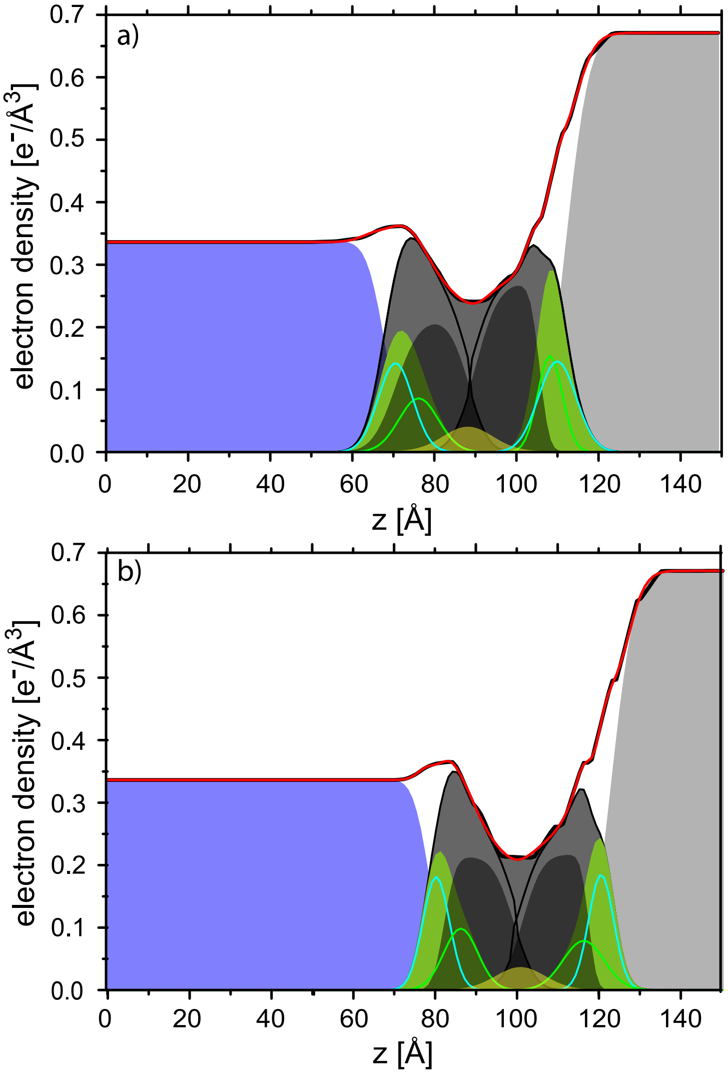

Figure 3.9: Electron density profiles (*black thick line*) and decomposition fit (*red line*) of a pure POPC (*a*) and a 25% POPS 75% POPC containing bilayer (*b*). Shown are the phosphate and choline/serine groups (*green gaussians*), carbonyl and glycerol groups (*turquois gaussians*), methylene chains (*black areas*) and methyl groups (*yellow gaussian*). Silicon substrate and water are shown as grey and blue areas. Furthermore, the overall headgroup (*dark green areas*) of the bilayer, the area of each leaflet (*black lines*) and the overall bilayer area (*dark grey area*) are shown.

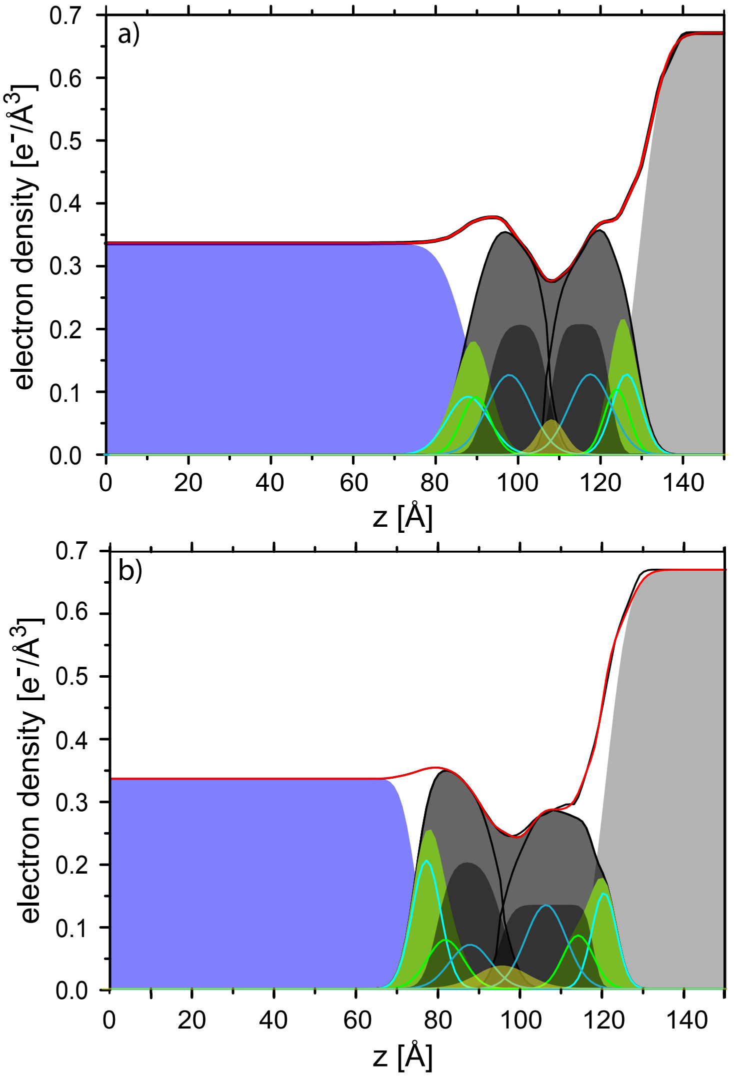

Figure 3.10: Electron density profiles (*black thick lines*) and decomposition fit (*red lines*) of a pure PCb (*a*) and a 25% POPS 75% PCb bilayer (*b*) in pure water. Shown are the phosphate and serine groups (*green gaussians*), carbonyl groups (*turquois gaussians*), methylene chains (*black areas*) and bromine groups (*blue gaussians*). Silicon substrate and water are shown as grey and blue areas. Furthermore, the overall headgroup (*dark green areas*) of the bilayer, the area of each leaflet (*black lines*) and the overall bilayer area (*dark grey areas*) are shown.

bilayer	thickness [Å]	area per lipid distal leaflet [Å^2]	area per lipid proximal leaflet [Å^2]
100% POPC	39 ± 2	60 ± 6	59 ± 3
25% POPS 75% POPC	39 ± 1	70 ± 5	66 ± 2
100% PCb	39 ± 1	78 ± 2	79 ± 3
25% POPS 75% PCb	42 ± 2	83 ± 8 amount of PCb: 0.51 ± 0.05	85 ± 1 amount of PCb: 1 ± 0.01

Table 3.1: Weighted mean of width and area per lipid of a POPC, a 25% POPS 75% POPC, a PCb, and a 25% POPS 75% PCb containing bilayer, in pure water.

the same area per lipid, namely 85 Å^2. Compared to the pure PCb bilayer, the 25% POPS 75% PCb bilayer exhibits a lower packing density in both leaflets. The slight increase in packing density is inline with the increase for the 25% POPS 75% POPS containing bilayer.

Interestingly, the area per lipid is higher in all PCb containing bilayers than in the unlabeled bilayers. The lower bilayer density presumably stems from the large bromine label attached to the hydrocarbon chains of the lipids. Such an increase in lipid area to larger values was already observed for monolayers formed from lipids with attached bromine label [130] at the liquid air interface. The labeling of one species of lipids allows for the possibility to resolve the distribution of each lipid in both leaflets separately. Fitting of the profile of the 75% PCb 25% POPS containing bilayer leads to a PCb fraction in the distal leaflet of 0.51 ± 0.05 and 0.99 ± 0.01 in the proximal leaflet. This enrichment of negatively charged POPS in the distal layer may be attributed to electrostatic repulsion between substrate and lipids. After appropriate cleaning, silicon oxide has a high density of negatively charged OH groups. This may cause a lipid redistribution, either during the spreading process, or negatively charged lipids flip flop from the proximal to the distal leaflet in the formed bilayer [131].

3.2.3 Influence of calcium on bilayer structure

In the following section the influence of calcium on the structure and mobility of surface supported bilayers is investigated for different bilayer compositions. Figure 3.11 shows the x-ray reflectivity data of a pure PCb (*I*), a 25% POPS 75% POPC (*II*), a 25% POPS 75% PCb (*III*) and a 50% POPS 50% POPC (*IV*) containing bilayer in a 1 mM calcium 20 mM Tris buffer (buffer B). The rapid Kiessig fringes with $\Delta q \approx 0.016$ Å^{-1} for both of the 25% PS containing bilayer and $\Delta q \approx 0.0064$ Å^{-1} for the 50 % POPS containing bilayer are due to interference of the thermal silicon oxide layer on top of the silicon surface and the silicon substrate. The Kiessig fringes of the data of the 50 % POPS bilayer are due to a substrate with 1000 Å silicon oxide layer as compared to 500 Å for all other samples. The broad Kiessig fringes with $\Delta q \approx 0.15$ Å^{-1} originate from the surface supported bilayer [109]. The bromine label of PCb leads to a smearing out of the Kiessig fringes due to a

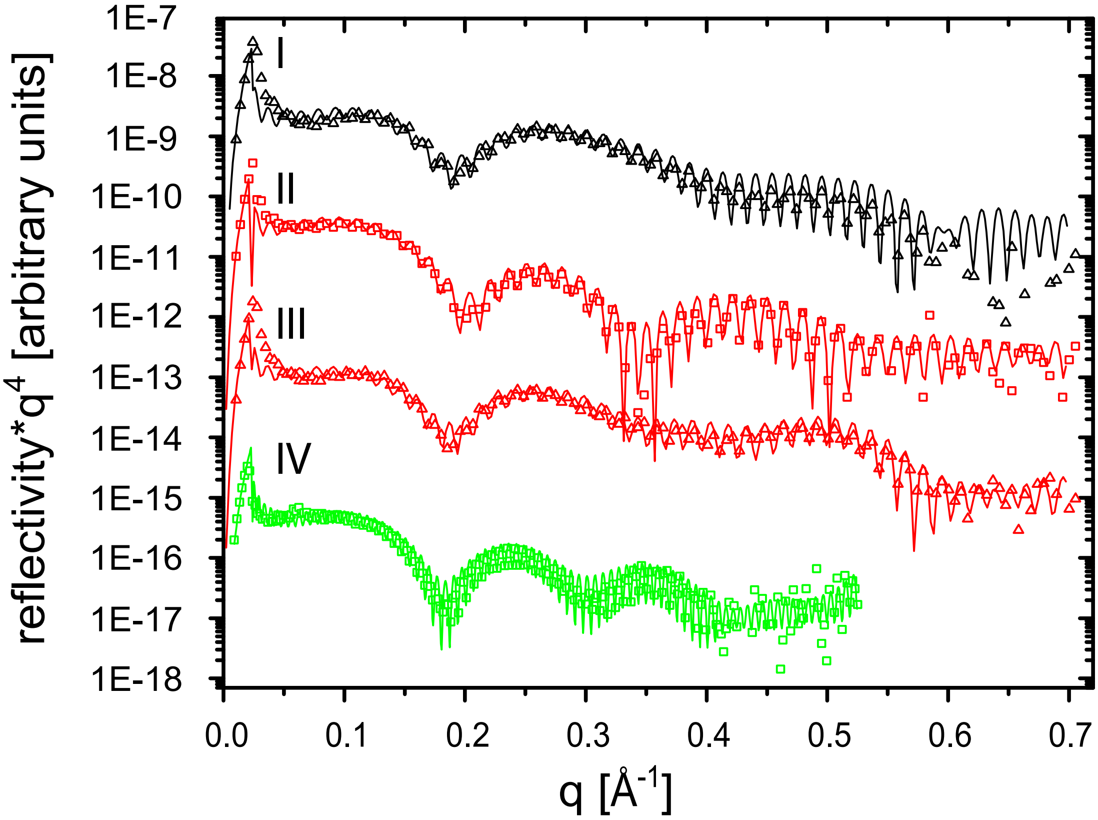

Figure 3.11: X-ray reflectivity data and fit of a pure PCb (*I)*) a 25% POPS 75% POPC (*II*) bilayer, a 25% POPS 75% PCb (*III*) and a 50% POPS 50% POPC (*IV*) bilayer in buffer B.

superposition of the bromine signal and the bilayer, as observed before (see figure 3.6).

The evaluation of the reflectivity data of a 75% POPC 25% POPS and a 50% POPC 50% POPS bilayer in calcium buffer results in the electron density profiles in figure 3.12. In both bilayers head and chains distal to the substrate, as well as the hydrophobic part of the bilayers are discernible [109]. The headgroup proximal to the silicon surface is not visible in the total profile (*red curve*) of the 25% POPS containing bilayer. In contrast, it is evident in the profile of the 50% POPS containing bilayer, in the shoulder of the electron density of the silicon contribution.

To obtain information of the packing of the lipids in the two membrane leaflets, the averaged electron density profile is decomposed into its chemical groups as described in section 3.2.2. Since calcium bridges negatively charged serine groups [132, 133], one calcium per two POPS is added to the serine group for the analysis of measurements performed in calcium containing buffer. The exact analysis and fitting routine is described in chapter 2.5.7. Figure 3.12 shows the contribution of each of the single chemical compounds to the overall electron density profile of a pure POPC bilayer (*a*) and a 25% POPS 75% POPC containing bilayer (*b*) in calcium containing buffer. The result of the bilayer decomposition

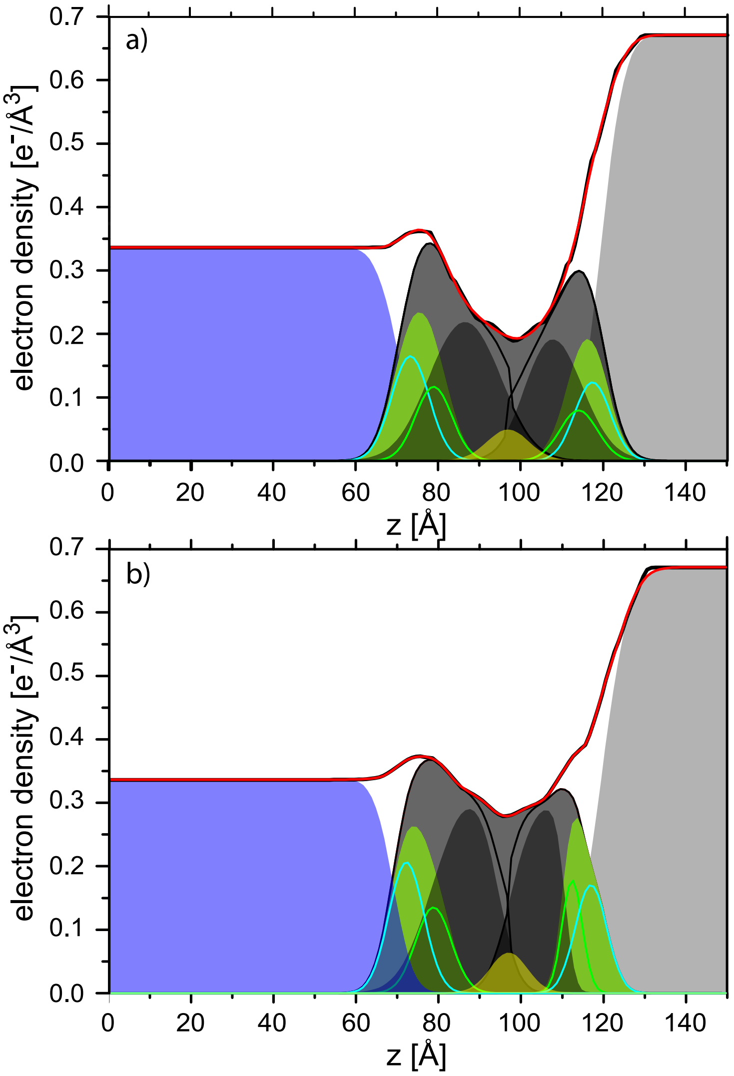

Figure 3.12: Electron density profile (*black thick line*) and chemical component distribution of a 25% POPS (*a*) and a 50% POPS (*b*) containing bilayer in buffer B. Turquoise gaussians describe the phosphate and choline/serine groups, green gaussians the carbonyl and glycerol groups and yellow gaussians the methyl groups of both leaflets. The black filled areas describe the alkyl chains, green filed areas the overall head group distributions. Furthermore, the water distribution (*blue filled areas*) and the substrate (*light grey filled areas*) distribution are indicated. Dark grey areas describe the overall bilayer distributions. Black lines describe the distributions of proximal and distal leaflet.

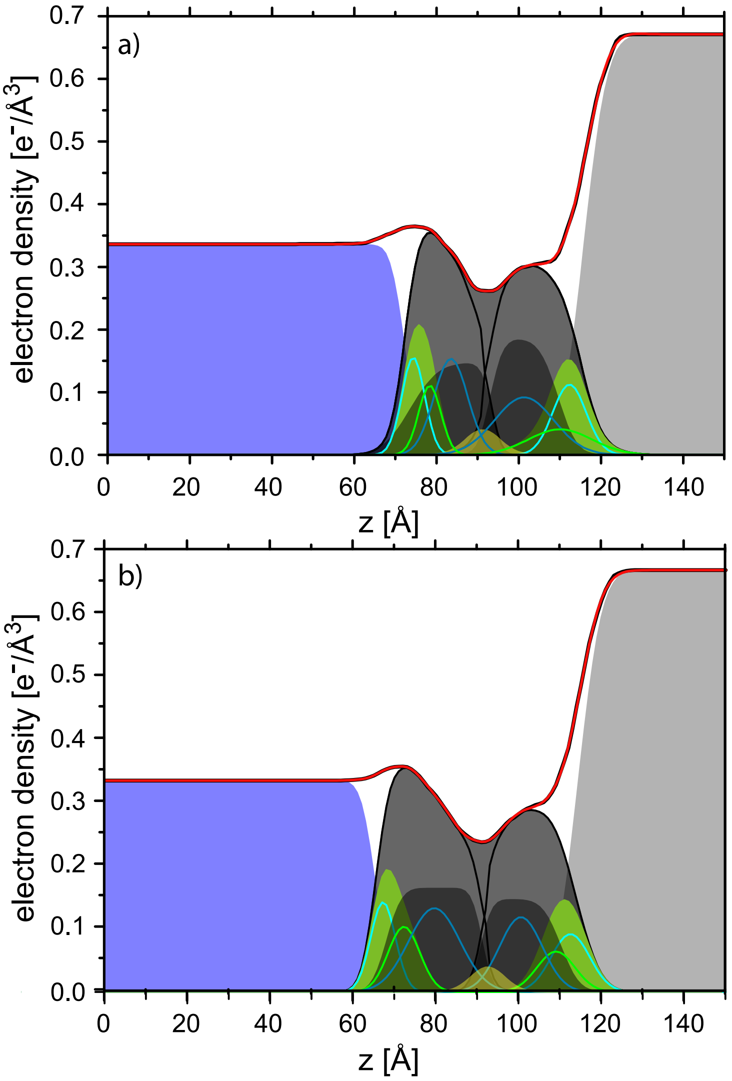

Figure 3.13: Electron density (*black thick line*) and decomposition fit (*red line*) of a pure PCb (*upper figure*) and a 25% POPS 75% PCb containing bilayer (*lower figure*) in calcium containing buffer. Shown are the phosphate and choline/serine groups (*green gaussian*), carbonyl and glycerol groups (*turquois gaussian*), methylene groups (*black areas*) and bromine groups (*blue gaussians*). Silicon substrate and water are shown as grey and blue areas. Furthermore, the overall headgroup (*dark green area*) of the bilayer, the area of each leaflet (*black lines*) and the overall bilayer area (*dark grey area*) are shown.

bilayer	thickness [Å]	area per lipid distal leaflet [$Å^2$]	area per lipid proximal leaflet [$Å^2$]
25% POPS 75% POPC	42 ± 2	57 ± 3	67 ± 3
50% POPS 50%POPC	39 ± 2	54 ± 5	61 ± 2
100% PCb	40 ± 2	82 ± 5	84 ± 3
25% POPS 75% PCb	45 ± 1	66 ± 5 amount of PCb: 0.79 ± 0.15	90 ± 1 amount of PCb: 0.98 ± 0.03

Table 3.2: Thickness and area per lipid of a POPC a 25% POPS 75% POPC, a PCb and a 25% POPS 75% PCb containing bilayer in buffer B.

is summarized in table 3.2. In both cases, the distal leaflets display a higher density than the proximal leaflets, namely a lipid area of 57 ± 3 $Å^2$ as compared to 67 ± 3 $Å^2$ for the 25% POPS bilayer and 54 ± 5 $Å^2$ as compared to 61 ± 2 $Å^2$ for the 50 % POPS bilayer. Furthermore, the distal leaflet of the 25% POPS bilayer exhibits a higher density in calcium containing buffer than in pure water, while in the proximal leaflet the area per lipid remains unchanged. The thickness of the 25% POPS bilayer increases from 39 ± 1 Å in pure water to 42 ± 2 Å in calcium buffer. Apart from that, the 50% POPS bilayer shows a higher density of the distal leaflet than the 25% POPS containing bilayer. Calcium dehydrates the phosphate group in negatively charged lipids and induces a transition to a more stretched and more packed phase of the lipid headgroup [132]. The increase in density with POPS amount confirms this observation. The higher density of the distal leaflets in all negatively charged bilayers may be due to an accumulation of negatively charged lipids in the distal leaflet and a densification of such lipids due to calcium bridging. To resolve the distribution of negatively charged and neutral lipids in both leaflets bilayers containing brominated PCb lipids were investigated in calcium containing buffer. In figure 3.11 the reflectivity data and best fit to the data of a pure PCb (*I*) and a 25% POPS 75% PCb (*III*) bilayer are shown. Again, the chemically bound bromine label leads to a change in reflectivity signal as compared to bilayers without brominated alkyl chains. Figure 3.13 shows the electron density and chemical decomposition fit of a pure PCb bilayer and a 25% POPS 75% PCb bilayer.

Clearly visible are the headgroups distal to the surface. The headgroups proximal to the surface are hidden in the decrease of the substrate to the methylene chains. Interestingly, the signal of the bromine label is more pronounced in the proximal leaflet of both bilayers. However, the 25 % POPS bilayer exhibits a steeper decrease from the headgroup of the distal leaflet to the methylene chain region in the distal leaflet, leading to the assumption that there is less PCb in the distal leaflet than in the proximal leaflet. Table 3.2 summarizes the fitting results for bilayers in calcium buffer. The pure PCb bilayer exhibits the same area per lipid of 84 $Å^2$ for both leaflets within error. Furthermore, the lipid area and width does not change in calcium buffer as compared to pure water. For the 25% POPS 75% PCb bilayer, the area per lipid of the distal leaflet is lower than the area per lipid in the proximal leaflet, namely 66 ± 5 $Å^2$ and 90 ± 1 $Å^2$ respectively. The packing of the distal leaflet increases in calcium buffer to a lipid area of 66 ± 5 Å^2 as compared to 83 ± 8 Å^2 in pure water, while the proximal leaflet remains unaffected. Furthermore, the bilayer's width changes from 39 Å to 45 Å.

Thus, calcium leads in bilayers consisting of mixtures of PCb and POPS to a more stretched out and more densely packed conformation of the POPS lipids as observed before for label free bilayers. Fitting of the profiles leads to a PCb fraction 0.79 ± 0.14 in the distal and 0.98 ± 0.03 in the proximal leaflet. The use of bromine labeled PCb lipids confirms that negatively charged POPS lipids are prevented from redistributing to the proximal leaflet and reside in the distal bilayer leaflet. This is surprising because calcium is known to shield electrostatic forces to a high degree and it would be interesting to reveal if larger calcium concentrations and thus a larger electrostatic screening leads to an equal distribution of negatively charged lipids in both bilayer leaflets.

3.2.4 Diffusivity of negatively charged bilayers

The change of lipid mobility in cell membranes and bilayer model systems mirrors changes in their physical state and lateral structure. Therefore, diffusion measurements complement the structural investigations by x-ray reflectivity in the following sections. Here, the influence of buffer condition and protein binding on the fluidity of negatively charged bilayers are investigated with the method of continuous bleaching. An analytical method to analyze continuous bleaching data was developed by Dietrich *et. al* [103]. This approach does not hold for circular apertures of the microscope and inhomogeneous illumination profiles of the sample. To deal with these conditions a new tool to evaluate continuous bleaching data is developed, as introduced in the following section, in collaboration with Georg Fritz (Arnold Sommerfeld Center for Theoretical Physics, LMU München).

A new tool to evaluate continuous bleaching data

Unprocessed continuous bleaching data consists of a timeseries of fluorescent images taken after constant time intervals Δt. Since images are taken with a circular aperture, the theoretical description of the experimental setup requires the solution of the radial reaction diffusion equation

$$\frac{\partial}{\partial t}c(r,t) = D\left(\frac{\partial^2}{\partial r^2} + \frac{1}{r}\frac{\partial}{\partial r}\right)c(r,t) - k(r)c(r,t)\,, \tag{3.1}$$

where $c(r,t)$ is the concentration of unbleached fluorophore at time t and distance r from the center and $k(r)$ is the space-dependent bleaching rate. In order to extract the concentration of unbleached fluorophore from fluorescent images, a number of pre-processing steps are required. Also, the radial profile of the bleaching rate $k(r)$ needs to be estimated from the experimental data.

Image and data pre-processing. In a first step the radial intensity of a bleaching time series is extracted. Figure 3.14*a* shows the first frame of a continuous bleaching time series.

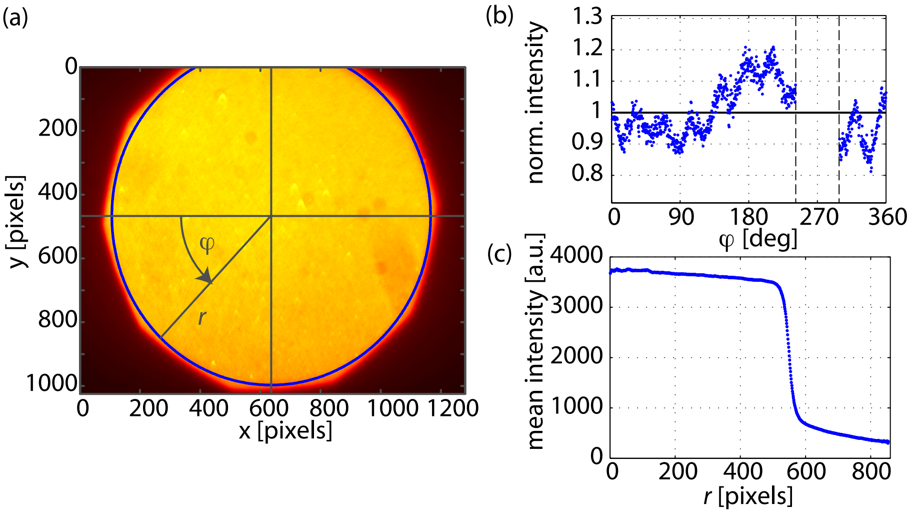

Figure 3.14: (*a*) Fluorescence microscopy image of a lipid bilayer composed of POPC recorded at t=0 s. (*b*) Normalized intensity at constant distance from the center of the bleached spot, extracted along the angular direction φ (*blue line* in (*a*). The gap in the intensity extraction at the chosen radius of $r = 530\,$pixels is due to the incomplete exposure of the illuminated area in the top part of (*a*). (*c*) Radial intensity profile obtained from averaging at each radial position r over all available angles φ.

In figure 3.14*b* the intensity profile along the angular direction is shown (see figure 3.14*a*, *blue circle*). To obtain the radial intensity profile the average intensity at radial position r, is obtained from an average over all angles φ. To this end, φ was discretized into N_φ discretization steps, i.e., $\varphi_i = (2\pi i)/N_\varphi$, and the average intensity at radial position r was computed according to

$$I(r) = \frac{1}{N_\varphi} \sum_{i=1}^{N_\varphi} I(r, \varphi_i)\,, \tag{3.2}$$

leading to the profile in figure 3.14*c*. At low values of r it might well be that individual intensity values in a given pixel are counted multiple times, whereas at high values of r some pixels are left out for averaging. Hence, at low r less pixels are effectively used for averaging and thus relative fluctuations are larger than at high r values. The extraction of the radial intensity profile of each time frame of a continuous bleaching series (figure 3.15*a*) leads to intensity profiles as shown in figure 3.15*b*.

Assuming that initially all fluorophores are unbleached, the curved intensity profile $I_0(r)$ at $t = 0$ min (figure 3.15*b*) indicates, that the lamp of the microscope produces an uneven illumination profile. This has twofold implications: First, the radial intensity does not directly mirror the concentration profile of the sample and second, the bleaching rate is a function of r. In order to extract concentration profiles from intensity profiles, the whole time series of intensity profiles are normalized by the first frame of the measurement (see figure 3.15*c* and *d*). This approach is reasonable as long as the focussing period ($t < 0\,$s) is short enough to prevent the first image from significant photobleaching.

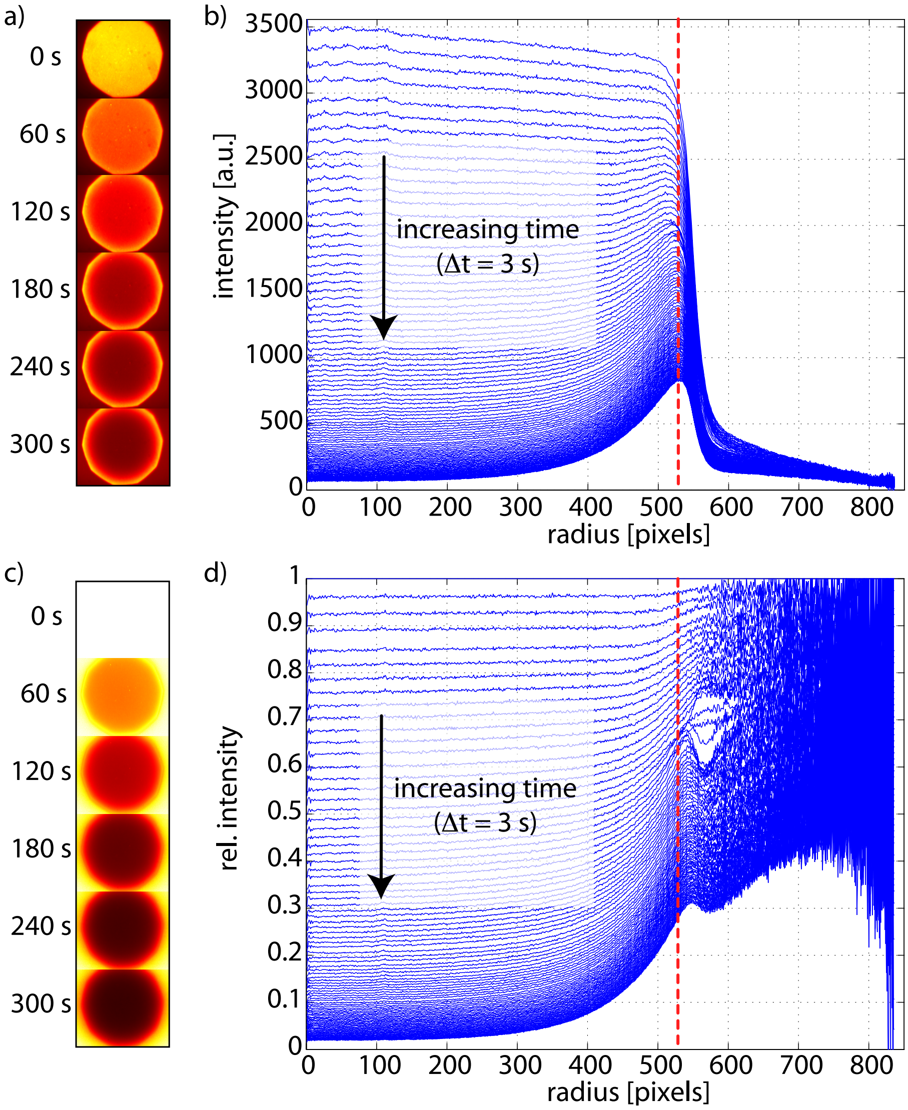

Figure 3.15: (*a*) Unprocessed timeseries of fluorescence images obtained from continuous bleaching of a standard POPC membrane. (*b*) Radial intensity profiles as a function of time obtained from angular averaging. The time between subsequent profiles is $\Delta t = 3$ s. (*c*) Timeseries of fluorescence images after correction for uneven illumination. The correction was achieved by dividing all frames with $t > 0\,\mathrm{s}$ by the first frame at $t = 0\,\mathrm{s}$, which is assumed to represent the illumination profile. (*d*) Illumination-corrected radial intensity profiles. For radii smaller than the bleaching spot radius ($r < r_{spot}$; indicated by the *red dotted line*) the relative intensity is proportional to the concentration of unbleached fluorophores. For $r > r_{spot}$ the relative intensity displays large fluctuations and does no longer reflect the fluorophore concentration faithfully. This is because the illumination outside the bleaching ring is very low, and hence scatterlight and other background effects lead to large relative uncertainties.

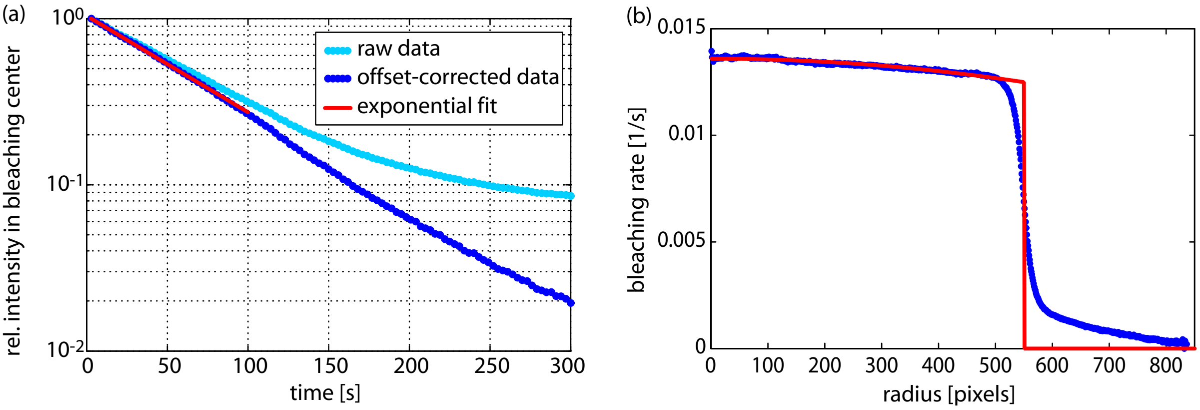

Figure 3.16: (*a*) Determination of the bleaching rate inside a small disc in the center of the bleaching spot ($r_{disc} = 20$ pixels). The raw data (*cyan line*) deviates after $t \approx 100\,\mathrm{s}$ from a simple exponential decay and saturates to a certain background intensity for large times. By subtraction of the minimal (relative) intensity extracted at $t = 15\,\mathrm{min}$, the offset-corrected intensities (*blue line*) were obtained. An exponential fit to these data yields the bleaching rate k_0 at $r = 0$. (*b*) The radial dependence of the bleaching rate was modulated according to the illumination profile $I_0(r)$, i.e. $k(r) = k_0 \times I_0(r)/I_0(r = 0)$ (*blue line*).

In a next step the bleaching profile is estimated. First, the central bleaching rate is estimated from a small disc in the center of the aperture area. Figure 3.16*a* shows the time dependent intensity in the center of the aperture area. The raw data (*cyan line*) deviates after a sample-specific time from a simple exponential decay and saturates to a certain background intensity for large times. However, for $r = 0$ one expects an exponential decay even in the long run, similar to the results of a slit aperture published previously [103]. By subtraction of the minimal (relative) intensity extracted at large times, the offset-corrected intensities (*blue line*) are obtained. An exponential fit to these data yields the bleaching rate k_0 at $r = 0$. Then the radial dependence of the bleaching rate is modulated according to the illumination profile $I_0(r)$, i.e. $k(r) = k_0 \times I_0(r)/I_0(r = 0)$ see figure 3.16*b* (*blue line*).

Numerical solution of the radial diffusion equation. For a numerical solution of equation 3.1 the temporal and spatial coordinates are discretized by

$$\begin{aligned} t_n &\equiv t_0 + n\Delta t, & n &= 0, 1, \ldots, N \text{ and} \\ r_j &\equiv j\Delta r, & j &= 0, 1, \ldots, J\,, \end{aligned} \tag{3.3}$$

with Δt and Δr being the temporal and spatial discretization stepsize, respectively. $c_j^n \equiv c(r_j, t_n)$ and $k_j \equiv k(r_j)$ are defined accordingly. The derivatives in Eq. (3.1) are approxi-

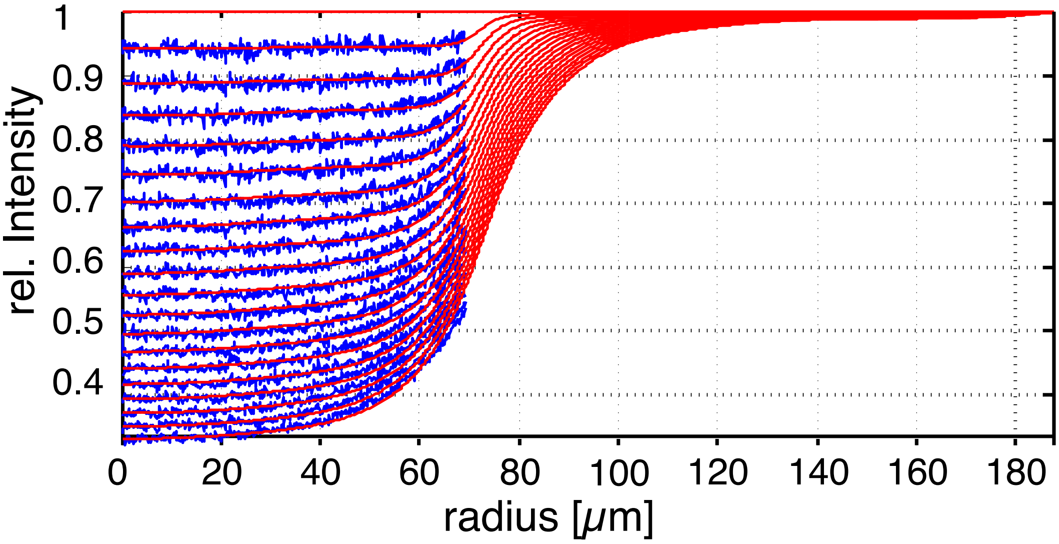

Figure 3.17: Numerical fit *red lines* to the 20 first frames of the radial intensity profile *blue lines* of a continuous bleaching time series of a POPC bilayer in water.

mated by finite differencing via the implicit *Crank-Nicolson* scheme [134],

$$\begin{aligned}
\frac{\partial c}{\partial t} &\approx \frac{c_j^{n+1} - c_j^n}{\Delta t}\,,\\
\frac{\partial c}{\partial r} &\approx \frac{1}{4}\left(\frac{c_{j+1}^n - c_{j-1}^n}{\Delta r} + \frac{c_{j+1}^{n+1} - c_{j-1}^{n+1}}{\Delta r}\right) \text{ and}\\
\frac{\partial^2 c}{\partial r^2} &\approx \frac{1}{2}\left(\frac{c_{j+1}^n - 2c_j^n + c_{j-1}^n}{(\Delta r)^2} + \frac{c_{j+1}^{n+1} - 2c_j^{n+1} + c_{j-1}^{n+1}}{(\Delta r)^2}\right).
\end{aligned} \tag{3.4}$$

Inserting (3.4) in (3.1) and grouping the terms accordingly, leads to the iteration rule

$$\begin{gathered}
-\alpha(1+\frac{\Delta r}{2r_j})c_{j+1}^{n+1} + (1+2\alpha)c_j^{n+1} - \alpha(1-\frac{\Delta r}{2r_j})c_{j-1}^{n+1} = \\
\alpha(1+\frac{\Delta r}{2r_j})c_{j+1}^{n} + (1-2\alpha-\Delta t k_j)c_j^{n} + \alpha(1-\frac{\Delta r}{2r_j})c_{j-1}^{n}\,,\\
j = 1, 2, \ldots, J-1,
\end{gathered} \tag{3.5}$$

with $\alpha \equiv D\Delta t/(2\Delta r^2)$. The boundary conditions are chosen such that there is zero flux at $r = 0$ (Neumann boundary condition) and a fixed concentration at $r = r_J$ (Dirichlet boundary condition). The former condition results from the fact, that there is no source or sink at the origin, and hence, the slope of the concentration profile must vanish. The latter boundary condition implements an inexhaustible reservoir at $r = r_J$, where $r_J = 2000$ pixels is chosen much larger than the radius of the bleaching spot ($r \approx 500$ pixel). Together,

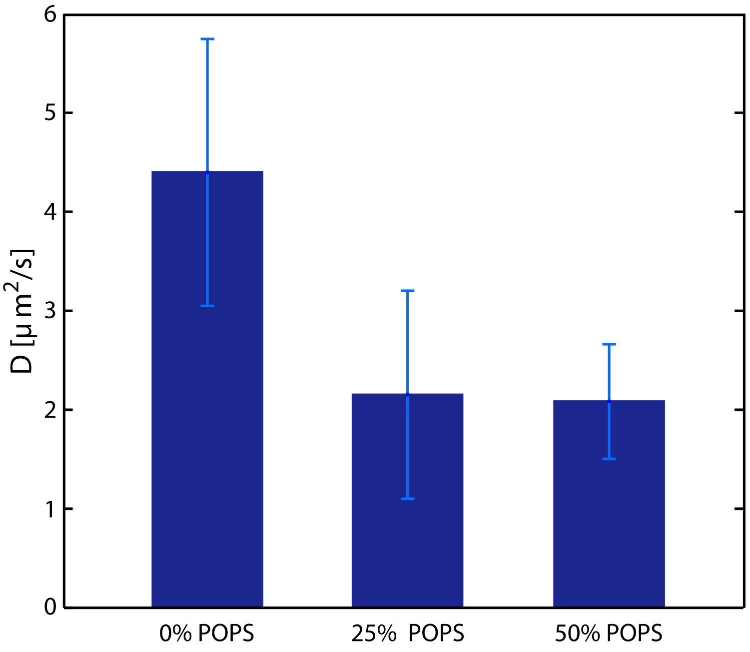

Figure 3.18: Diffusion constant of a pure POPC a 25% POPS and a 50% POPS containing bilayer.

they determine the iteration rules for $j = 0$ and $j = J$,

$$\begin{aligned} -2\alpha c_1^{n+1} + (1+2\alpha)c_0^{n+1} = \\ 2\alpha c_1^n + (1 - 2\alpha - \Delta t k_j)c_0^n \ , \text{ and} \\ c_J^{n+1} = c_J^n \, . \end{aligned} \tag{3.6}$$

Parameter estimation. The iteration scheme in Eq. (3.5) was implemented in C++ to solve the reaction diffusion equation and yield concentration profiles at pre-described time-intervals Δt - analogous to the experimental data. However, when comparing theory and experiment, it turned out that experimental data often deviated slightly in total concentration from the theoretical profiles. We attributed these deviations to fluctuations in the lamp intensity on short timescales and rescaled experimental concentration profiles to match the theoretical profiles at $r = 0$. Then, we calculated the χ^2 as the sum of the squared deviations between theory and experiment and varied the diffusion constant D to minimize χ^2 by a Brent minimization algorithm. The result of such a fit to the first 20 frames of a POPC bilayer in water is shown in figure 3.17.

Diffusion of negatively charged bilayers in calcium containing buffer

Figure 3.18 shows the diffusion constants of four different bilayers on silicon supports. A 50% POPC 50% POPS, a 75% POPC 25%POPS bilayer and a bilayer that consists of pure

POPC as a control are investigated. For the pure POPC bilayer a diffusion constant of 4.2 ± 1.4 µm^2/s is obtained. This result indicates an initially very fluid surface supported bilayer in the expected range [135, 136, 137]. Compared to the pure POPC bilayer, the 25% POPS 75% POPC bilayer exhibits in calcium buffer a drastic reduction of the diffusion constant of approximately 50%, to a value of 2.3 ± 1 µm^2/s. The data of the 50% POPS 50% POPC containing bilayer exhibits a similar diffusion constant as the bilayer with 25% POPS amount.

3.2.5 Summary of bilayer investigations in water and calcium buffer

The method of vesicle spreading with osmotic pressure lead to homogenous surface supported bilayers on silicon supports with a high concentration of negatively charged lipid. The structure of bilayers with different ratio of negatively charged POPS to neutral POPC was investigated with x-ray reflectometry. Furthermore, it was shown that bromine labeled PC derivatives provide the possibility to resolve the lipid distribution in both bilayer leaflets, independently. All measurements of bilayers containing negatively charged POPS lipids displayed a slight increase in lipid area in pure water compared with pure zwitterionic bilayers. Upon the addition of calcium, all POPS containing bilayers exhibited an increase in lipid packing in the distal leaflets, while the density of the proximal leaflets and the density of pure zwitterionic bilayers was unaffected. The chemical decomposition of the electron density of a mixed PCb/POPS bilayer revealed an accumulation of negatively charged POPS lipid in the proximal bilayer leaflet in water and calcium buffer, while the proximal leaflet consisted solely of PCb in both buffer conditions. A new program to evaluate continuous bleaching data with a standard microscopy setup was developed and was successfully applied to compare diffusion constants of pure POPC bilayers and bilayers consisting of POPC/POPS mixtures. The measurements revealed a reduced diffusion constant for POPS containing SLBs in calcium buffer compared to pure POPC SLBs.

3.3 Arrangement of Annexin II and its influence on bilayer structure and lipid diffusivity

In the following section the binding of the protein Annexin II in its tetrameric (Anx A2t) and monomeric (Anx A2m) form to single supported bilayers of different compositions is investigated. Here, the conformation of the protein upon binding and the accompanied structural and dynamical changes in the lipid membranes are resolved.

3.3.1 Arrangement of Annexin II

Figure 3.19 shows the reflectivity data of three bilayer compositions, namely a 25% POPS 75% POPC containing bilayer (*I*), a 25% POPS 75% PCb containing bilayer (*II*) and a

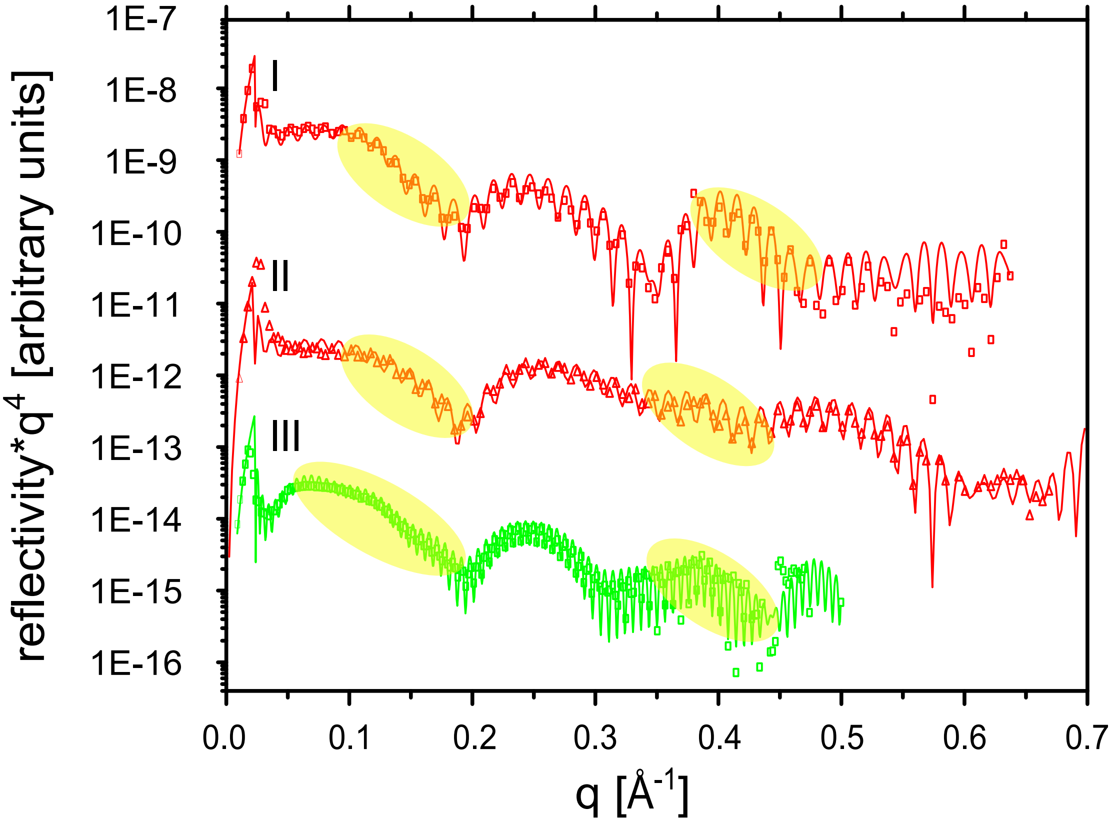

Figure 3.19: X-ray reflectivity data and best fit after Anx A2t incubation of a 25% POPS 75 %POPC bilayer (*I*), a 25% POPS 75 %PCb bilayer (*II*) and a 50% POPS 50 %POPC bilayer (*III*). Yellow ellipsoids mark the region with pronounced changes in reflectivity signal due to Anx A2t binding, compared to bare bilayers (cf. figure 3.11).

50% POPS 50% POPC containing bilayer (*III*) are shown. Incubation with Anx A2t leads to a clear change in reflectivity signal (*yellow ellipsoids*) as compared to bilayers in calcium containing buffer, cf. figure 3.11.

The reflectivity data is analysed as described in section 2.5.4 and the resulting electron density profiles and chemical decomposition fits are shown in figure 3.20. After Anx A2t incubation, an increase in electron density adjacent to the distal headgroup is observed in all bilayer compositions (figure 3.20, *red areas*). This increase is identified as the Anx A2t layer. In the case of the 50% POPS bilayer the Anx A2t signature is more pronounced compared to both of the 25% POPS bilayers, indicating a larger Anx A2t coverage for increasing POPS content. Calculation of the protein coverage as desribed in section 2.5.8 reveals a protein coverage of 91% in the case of the 50% POPS bilayer 27% in the case of the 25% POPS 75% POPC and 12% in the 25% POPS 75% PCb containing bilayer. Table 3.3 summarizes the result for three different protein coverages. Interestingly, all data sets exhibit approximately the same protein layer thickness of about 60 Å indicating that the higher protein coverage does not influence Anx A2t configuration. Moreover, already

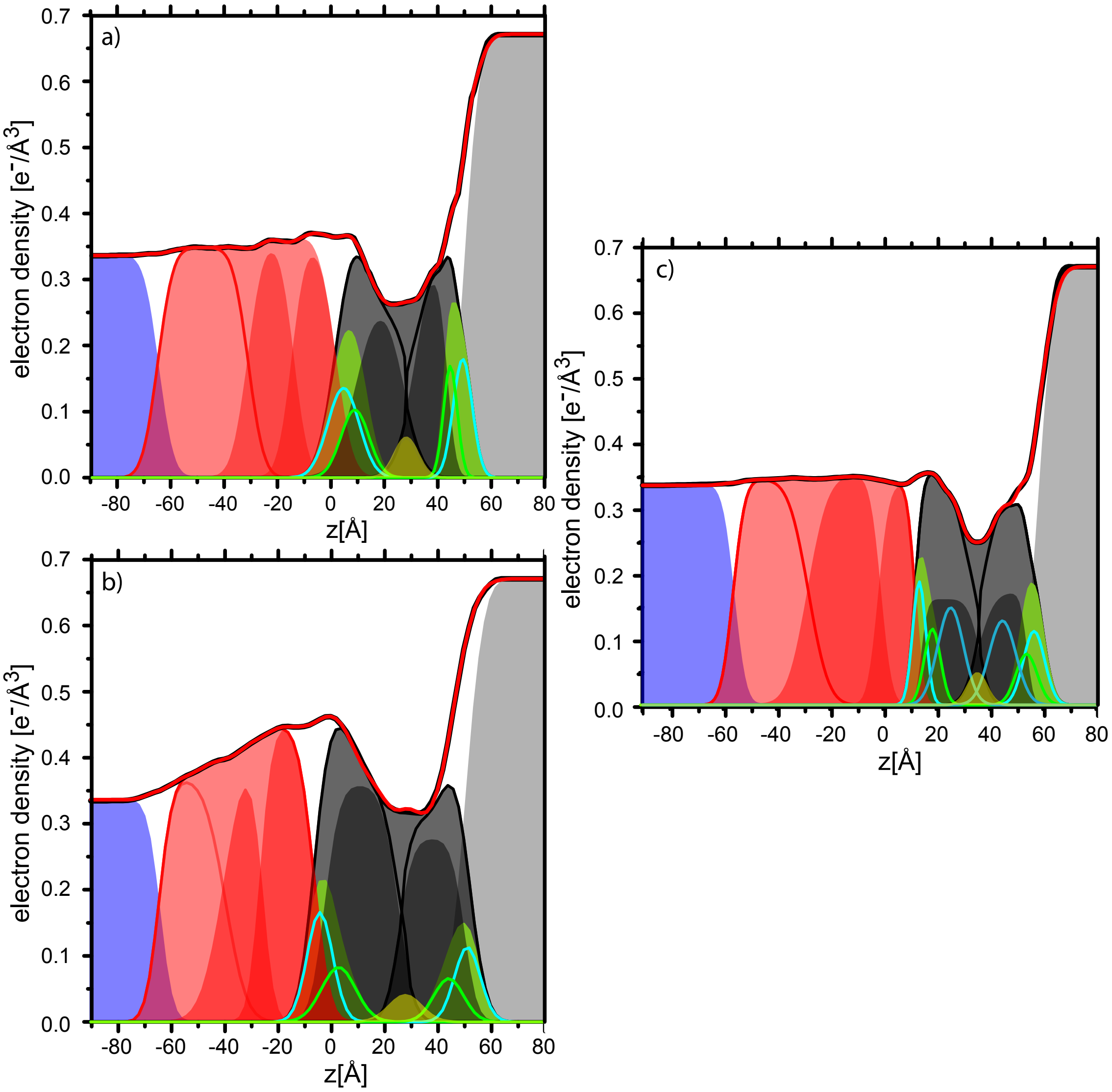

Figure 3.20: Electron density profiles (*black thick line*) and decomposition fit (*red line*) of a 25% POPS 75% POPC bilayer (*a*), a 50% POPC 50% POPS bilayer (*b*) and a 25% POPS 75% PCb bilayer (*c*), after Anx A2t binding. Shown are the phosphate and serine groups (*green gaussian*), carbonyl groups (*turquois gaussian*), methan groups (*black areas*) and bromine groups (*blue gaussians*). Silicon substrate and water are shown as grey and blue areas. Furthermore, the overall headgroup (*green area*) of the bilayer, the area of each leaflet (*black lines*) and the overall bilayer area (*dark grey area*) are shown. The distribution of Anx A2t is shown by red lines and the overall protein by the red area.

bilayer	protein coverage, incubated protein	protein width [Å]
25% POPS 75% POPC	0.27, Anx A2t	67 ± 2
50% POPS 50% POPC	0.91, Anx A2t	66 ± 2
25% POPS 75% PCb	0.12, Anx A2t	70 ± 1
25% POPS 75% POPC	0.13, Anx A2m	35 ± 1

Table 3.3: Weighted mean of protein width for different protein coverage rates and Annexin II tetramer (Anx A2t) as compared to Annexin II monomer (Anx A2m).

from visual inspection of the electron density profiles the vertical configuration of Anx A2t seems very unlikely, as it would result in a significantly larger thickness of the protein layer (cf. figure 1.3,*b*) [76, 78, 80, 81].

Annexin A2 monomer

To compare the obtained Anx A2t structure with the Annexin II monomer (Anx A2m) structure, a 25% POPS 75%POPC bilayer is investigated with x-ray reflectivity in calcium buffer and after Anx A2m incubation. Figure 3.21 shows the obtained data and best fit to the data in calcium buffer (*I*) and after Anx A2m incubation (*II*). The Anx A2m signature (*yellow ellipsoids*) changes the data at different q values as compared with the tetramer (compare with figure 3.19, *yellow ellipsoids*). This difference indicates a larger thickness of the tetramer than the monomer. Evaluation of the data leads to the electron density profiles in figure 3.22. After Anx A2m incubation an increase in electron density adjacent to the distal headgroup is observed (figure 3.22*b, red area*). This increase is identified as the Anx A2m layer. In table 3.3 the result of the width of the monomer layer as compared to the width of the tetramer layer at three different protein coverages is shown. The monomer signature exhibits a thickness of about 35 Å. This is a slightly larger thickness as 30 Å which were obtained from AFM measurements [69]. Compared with Anx A2t the reduced thickness of the monomer is caused by the missing p11 protein dimer (cf. figure 1.3*b*). The protein coverage of the bilayer is calculated as described above. For the monomer a protein coverage of 0.13 is obtained from the maximum in electron density in the Anx A2m signal.

3.3.2 Influence of Annexin II Tetramer binding on bilayer structure and mobility

To obtain the effect of Annexin II tetramer (Anx A2t) binding on bilayer structure, the results of the chemical decomposition of a 25% POPS 75% POPC a 50% POPS 50% POPC and a 25% POPS 75% POPC bilayer after Anx A2t incubation are compared with the structural results of the same bilayers in calcium buffer.

Table 3.4 summarizes the results of the chemical decomposition after Anx A2t incubation. After Anx A2t incubation the bilayers thickness increases slightly from 40 ± 2 Å to 48 ± 1 Å in the case of the 25% POPS containing bilayer, and from 39 ± 2 Å to 45 ± 1 Å

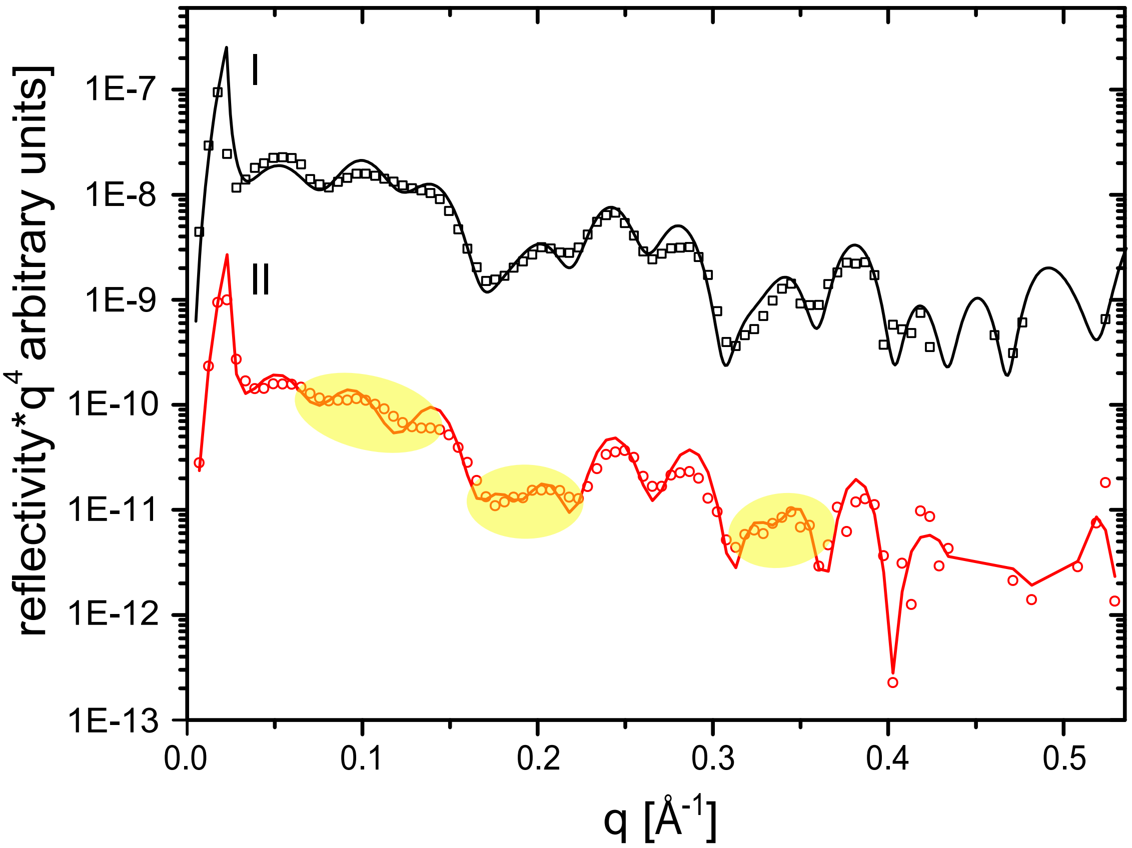

Figure 3.21: X-ray reflectivity data and best fit to a 25% POPS 75%POPC bilayer before (*I*), and after (*II*) Anx A2m incubation. Yellow ellipsoids indicate the change in the reflectivity signal due to Anx A2m binding.

bilayer	thickness [Å]	area per lipid distal leaflet [Å^2]	area per lipid proximal leaflet [Å^2]
25% POPS 75% POPC	48 ± 1	46 ± 4	66 ± 2
50% POPS 50% POPC	45 ± 1	41 ± 1	62± 1
25% POPS 75% PCb	44 ± 1	70 ± 1 amount of PCb = 0.89 ± 0.1	86 ± 1 amount of PCb = 1 ± 0.01

Table 3.4: Thickness and area per lipid of both leaflets, of a pure POPC a 25% POPS 75% POPC, a 50% POPS 50% POPC and a 25% POPS 75% PCb containing bilayer after Anx A2t incubation.

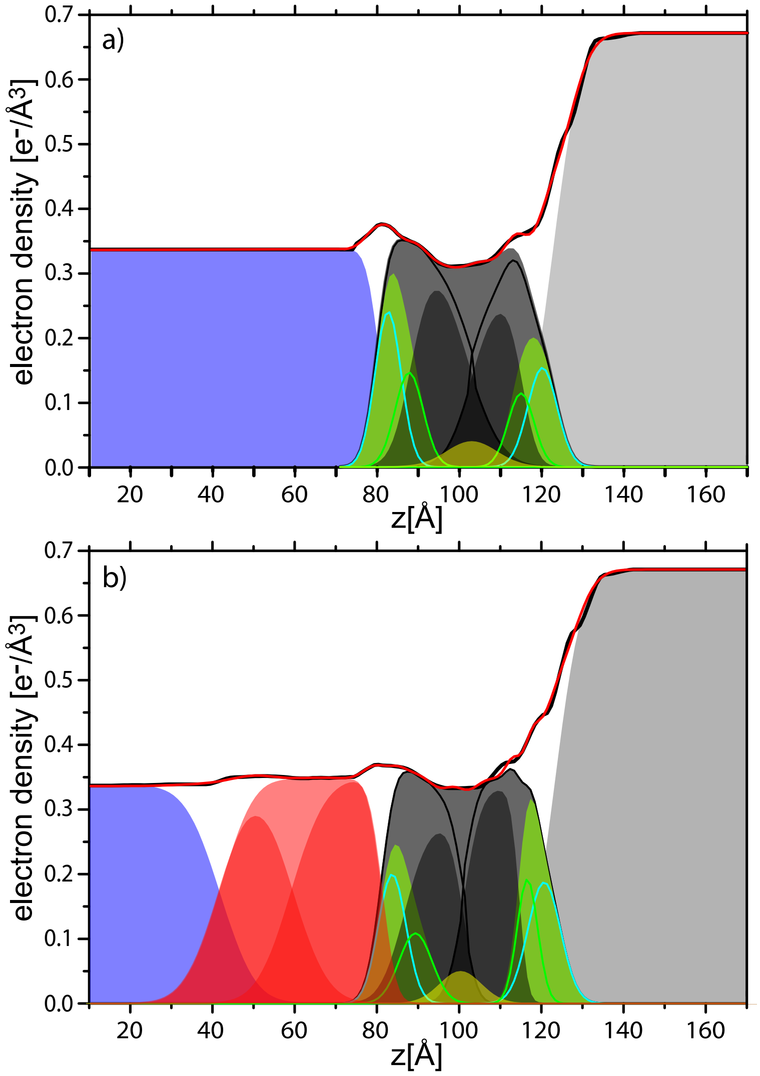

Figure 3.22: Electron density profile (*black thick line*) and decomposition fit (*red line*) of a 25% POPS 75% POPC bilayer in calcium buffer (*a*) and the same bilayer after Anx A2m incubation (*b*). Shown are the phosphate and serine groups (*green gaussian*), carbonyl groups (*turquois gaussian*), methylene groups (*black areas*) and bromine groups (*blue gaussians*). Silicon substrate and water are shown as grey and blue areas. Furthermore, the overall headgroup (*dark green area*) of the bilayer, the area of each leaflet (*black lines*) and the overall bilayer area (*dark grey area*) are shown. The distribution of Anx A2m is shown by red lines and the overall protein by the red area.

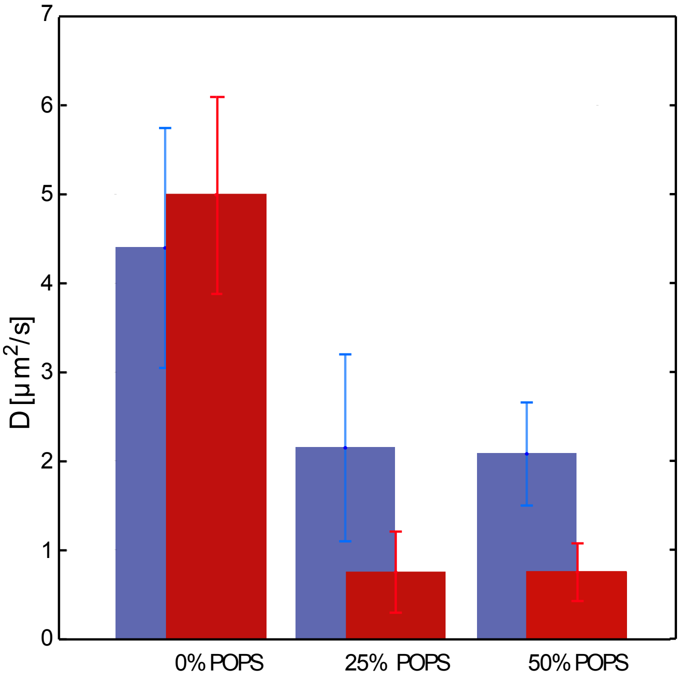

Figure 3.23: Diffusion constant of a pure POPC a 25% POPS and a 50% POPS containing bilayer in calcium buffer (*blue columns*) and after Anx A2t incubation (*red columns*).

in the case of the 50% POPS containing bilayer. However, the 25% POPS 75% PCb bilayer does not change its thickness. This may be due to the low protein coverage as calculated above (see table 3.3). All bilayers exhibit an asymmetric lipid packing density in the distal as compared to the proximal leaflet. The distal, buffer facing leaflet contains more lipid per unit area than the proximal leaflet. Furthermore, all POPS containing bilayers exhibit a higher packing density of the distal leaflet after Anx A2t incubation than in calcium containing buffer, namely, 46 ± 4 $Å^2$ per lipid as compared to 57 ± 3 $Å^2$ per lipid for the 25% POPS containing bilayer and 41 ± 1 $Å^2$ per lipid as compared to 54 ± 5 $Å^2$ per lipid in the case of the 50% POPS containing lipid bilayer. However, there is no change in packing density for the PCb containing bilayer after Anx A2t incubation, which may again be attributed to the low protein coverage. The packing density of the proximal leaflet does not change in all cases within error.

Now, the distribution of PCb in the two leaflets is resolved for the 25% POPS 75% PCb containing bilayer after Anx A2t incubation for each bilayer leaflet separately. Fitting of the electron density profile leads to an amount of PCb in the distal leaflet of 0.89 ± 0.1 and 1 ± 0.01 in the proximal leaflet, indicating that the proximal leaflet consists of pure PCb, while all POPS is located in the distal leaflet.

To investigate the influence of Anx A2t binding on bilayer diffusion, three different bilayer compositions are investigated with continuous bleaching. Figure 3.23 shows the diffusion constant of a 100% POPC, a 25% POPS 75% POPC and a 50% POPS 50%

POPC bilayer before (*blue columns*) and after Anx A2t incubation (*red columns*). Both POPS containing bilayers exhibit a drastic reduction in diffusion constant after Anx A2t incubation, namely 0.9 ± 0.5 $\mu m^2/s$ for the 25% POPS containing bilayer and 0.7 ± 0.2 $\mu m^2/s$ for the 50% POPS containing bilayer, as compared to 2.3 ± 1 $\mu m^2/s$ and 2.0 ± 0.8 $\mu m^2/s$ before protein binding. In contrast, the pure POPC bilayer displays the same diffusion constant before and after Anx A2t incubation (see figure 3.23).

Former AFM measurements have already revealed that the protein is able to accumulate PS lipids [15]. Here, x-ray reflectivity measurements revealed a densification of a 50 % POPS and a 25% POPS bilayer after Anx A2t incubation (see table 3.4). These structural investigations uncover, that Anx A2t not only redistributes POPS lipids into its binding area [15], but also condenses the bilayer upon binding, leading to a reduced diffusion constant.

3.3.3 The arrangement of Anx A2t and its influence on bilayer structure as obtained by neutron reflectivity

A further possibility to characterize a protein bound to a bilayer and the induced change in bilayer composition upon protein binding is to use neutron reflectivity. The method reveals the distribution and type of atomic nuclei in the sample and is thus a complementary method to x-ray reflectivity. In particular the possibility of changing the contrast between individual layers by partial deuteration of the system allows to highlight selected components.

Design of a microfluidic cell for neutron scattering

Previous neutron diffraction chambers consist of a teflon trough with a relatively large volume of approximately 20 ml [138]. Due to turbulent flow in large volumes, buffer exchange cannot be performed in a efficient way. Furthermore, the necessary amount of lipid, protein and buffer solution is tremendously high, leading to costly and time consuming experiments. In this work, a new chamber design is developed to circumvent these problems. In figure 3.24*a* the new chamber mounted on a silicon block is shown. It consists of a teflon block with a channel of only 100 μm thickness that is mounted on a silicon block by two aluminum lids. Two deeper channels for the inlets guarantee laminar flow over the silicon block (see figure 3.24*b*). Apart from that, a quartz glass window is glued into a cavity of the microfluidic channel, to allow for surface quality control by fluorescence microscopy. The microfluidic setup of the chamber guarantees a complete buffer exchange after rinsing with relatively small buffer amounts of 2.5 ml.

Neutron reflectivity of a negatively charged bilayer and bound Annexin II tetramer

Figure 3.25 shows the neutron reflectivity (NR) data of a 25 % POPS 75 % POPC containing bilayer on a silicon support in calcium buffer before Anx A2t incubation (*blue open*

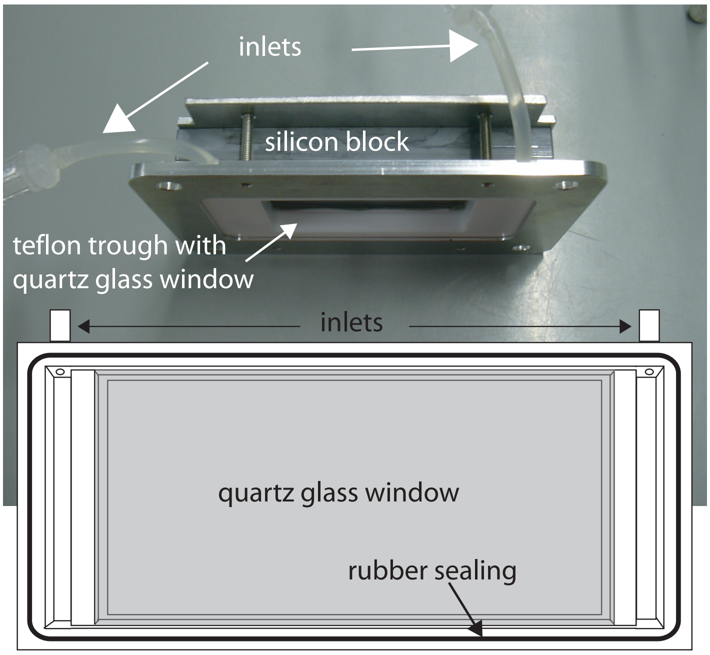

Figure 3.24: Microfluidic chamber used for neutron and microscopy measurements. (*a*) Picture of teflon trough that is mounted on a silicon block. (*b*) Cartoon of the microfluidic channel with inlets quartz glass window and rubber sealing.

squares), after Anx A2t incubation (*red open squares*) and after rinsing with EDTA containing buffer (*green open squares*). The rapid intensity oscillations (Kiessig fringes) with a periodicity of $\delta q \approx 0.013$ Å^{-1} are due to the interference between the reflections at the silicon oxide layer and the silicon substrate. For a momentum transfer q larger 0.075 these fringes disapear in the reflectivity signal, due to the lower resolution at higher q values (cf. section 2.5.3). The data of the bilayer (figure 3.25, *blue open squares*) exhibits the typical form of a protonated surface supported bilayer [139, 104, 140]. However, a dip in intensity at $q \approx 0.15$ Å$^{/1}$ as obtained for protonated bilayers is not detectable due to a low q_{max} of the measurement. After Anx A2t incubation a clear change in signal is investigated (*red open squares*).

Rinsing with EGTA containing buffer (buffer C) lead to a similar reflectivity signal as the signal of the bilayer before Anx A2t incubation (please compare figure 3.25, *green open squares* and *blue open squares*). This change in signal confirms that the protein reversibly binds in a calcium dependent manner. Evaluation of the neutron reflectivity data leads to the scattering length density (SLD) profiles in the inset of figure 3.25. The scattering length density of the protonated bilayer exhibits the typical thickness of a surface supported bilayer with D_2O inclusions. From the scattering length density of the buffer solution $\rho_{\mathrm{b}} = 6.074 \times 10^{-6}$Å^{-2} and the theoretical scattering length density of the bilayer hydrocarbon region $\rho_{\mathrm{CH_2}}$ = -0.2$\times 10^{-6}$Å^{-2} [104], a bilayer coverage of 76 % is calculated with equation 2.52. After Anx A2t incubation the SLD profile exhibits a further layer between buffer

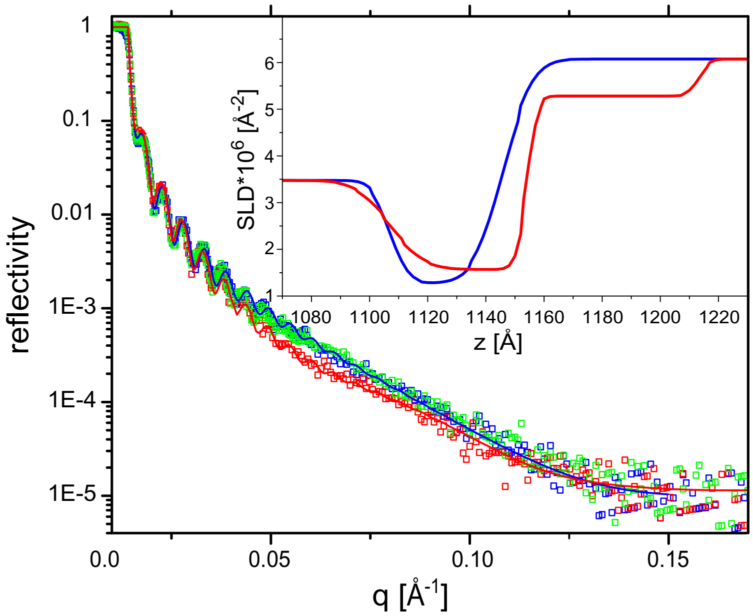

Figure 3.25: Neutron reflectivity data and fit to a 25% POPS 75% POPC bilayer before (*blue squares* and *blue line*), and after (*red squares* and *red line*) Anx A2t incubation *green squares*: the data approaches the original bilayer data after rinsing with buffer C (*green squares* and *green line*) which is supposed to remove Anx A2t.

and bilayer with a SLD of 5.283 $\times 10^{-6}$Å^{-2} and a thickness of about 60 Å. This layer is identified as an Anx A2t layer on top of the bilayer. The theoretical SLD for Annexin is obtained from the chemical sum formular of the protein (calculated with ExPASy [119]) as 1.88 $\times 10^{-6}$Å^{-2}. With equation 2.52 and the SLD of D_2O an Anx A2t coverage of 19 % is obtained, which is slightly lower as obtained by x-ray measurements (please compare with table 3.3, *first row*). This may be due to an exchange of hydrogen atoms with deuterium atoms at the surface of the protein, as already observed for Annexin V [141], which may lead to an increase in scattering length density of the protein, and to a seemingly lower coverage. After Anx A2t incubation, an increase in bilayer thickness from 39 Å to 47 Å is investigated. This increase in thickness is similar to the increase observed by XR (see table 3.4).Thus, the bilayer lipids change their conformation to a more stretched out state after Anx A2t incubation as already observed by XR. Furthermore, there is no change in SLD in the headgroup adjacent to the protein, indicating that the protein does not penetrate the bilayer, but rather sits on top of it. In summary XR and NR both reveal a change of the bilayer lipids to a more stretched out state after Anx A2t binding. Furthermore, both methods reveal an Anx A2t layer thickness of $\approx$ 60 Å and thus a binding of the protein in the open conformation as described in figure 2.9*a*, *upper figure*. Apart from that, due to the high contrast between protein and bilayer headgroup, NR reveals that Anx A2t does not penetrate the bilayers headregion but resides on top of the bilayer.

3.3.4 Summary of Annexin II tetramer binding

In all mixtures of POPC and POPS, the binding of the protein Anx A2t lead to a densification of solely the bilayers' distal leaflets, to a lipid packing close to gel values. The lipid areas of all proximal leaflets were not affected within error. In addition, for bilayers consisting of mixtures of POPC and POPS, the bilayer thicknesses after Anx A2t binding increased slightly. The electron density profile of a 25% POPS 75% PCb bilayer revealed an asymmetric lipid distribution, with an accumulation of POPS in the distal bilayer leaflet. Upon Anx A2t incubation, the diffusion constants of both POPS containing SLBs were significantly reduced, while bilayers consisting solely of POPC displayed the same diffusion constants as in calcium buffer.

The thicknesses of the Anx A2t layer obtained from x-ray and neutron reflectivity measurements were about 6 nm in all cases. Higher Anx A2t coverage did not lead to a change in protein layer thickness. In contrast, the binding of Anx A2 monomer lead to a thickness of the protein layer of about 3 nm, that is attributed to the missing p11 dimer. Neutron reflectivity measurements revealed that Anx A2t does not penetrate the bilayers headgroup but binds on top of the bilayer.

Chapter 4

Discussion

4.1 Structure of charged bilayers in water

In this thesis a new method to create surface supported negatively charged bilayers on silicon supports was developed. To this end, the silicon surface was incubated with large unilamelar vesicles (LUVS) of different ratio of negatively charged POPS to neutral POPC or PCb lipid, in a buffer with high monovalent salt concentration. After coverage by intact vesicles was reached, the surface was rinsed with pure water so that the high osmotic pressure between buffer inside the vesicles and water lead to an opening of the vesicles and the formation of single surface supported bilayers. With this method homogenous bilayers with an amount of negativly charged lipid up to 50 mol% could be obtained. X-ray reflectivity (XR) of a POPC bilayer in pure water revealed the typical shape of a surface supported lipid bilayer [109, 128, 129] and packing densities of about 60 Å^2/lipid for both leaflets. Since typical literature values for densities of uncharged bilayers are between 50 and 70 Å^2 /lipid [142, 129], the spreading method seems not to influence the structure of the obtained zwitterionic bilayer.

All measurements of bilayers containing negatively charged POPS lipids displayed a slight increase in lipid area in pure water compared with pure zwitterionic bilayers. Although the difference in lipid area is on the edge of experimental resolution (see table 3.1), all negatively charged bilayers consistently exhibit an increase in lipid area. This decrease in lipid density might be the consequence of an electrostatic repulsion between POPS lipids. Indeed, a larger lipid area for bilayers with negatively charged lipids has been proposed by theoretical calculations of the electrostatic free energy [143]. This theoretical prediction was approved in XR measurements of bilayer stacks in humid conditions. The lipid area increased with increasing PS amount in mixtures of DPPC and DPPS [144]. The measurements performed in this thesis are among the first observation of this effect for a single bilayer in water excess, and may thus give an insight into the forces that occur in mixed bilayers of native cell membranes.

To resolve the distribution of negatively charged lipid, a PC derivative with a chemically bound bromine label was used. Here it could be shown that on silicon supports SLBs are formed from such lipids and lipid mixtures of PCb and negatively charged POPS. The attached bromine label lead to a clear change in XR data in all cases. The electron density profile of a pure PCb bilayer clearly displayed an increase in electron density in the bilayer's chain region as compared to unlabeled bilayers, and resembled theoretical calculations of the electron density profile of a PCb bilayer (cf. figure 3.4). The increase in electron density is due to the large electron number of 35 e^- per bromine as compared to the lower electron density of the hydrocarbon chain region (for comparison see figure 3.8) [145, 115]. The chemical decomposition of the electron density profiles revealed a higher area per lipid for the PCb containing bilayers than bilayers that contained POPC (see table 3.1). The large bromine label presumably leads to a distortion in the packing of the hydrocarbon chain region and thus to less densely packed bilayers. Hristova *et al.* have already observed a similar behavior in lipid monolayers [130] at the liquid air interface and thus our results expand their observation to single surface supported bilayers.

The evaluation of the XR data of a 25% POPS 75% PCb bilayer revealed an asymmetric shape, with a larger increase in the electron density of the methylene chain region of the proximal leaflet than in the distal leaflet. This profile strikingly resembled the simulated profile of a bilayer with pure PCb in the proximal leaflet and POPS in the distal leaflet (see figure 3.5 *c*). In fact, the chemical decomposition of the electron density profile revealed an anisotropic distribution of brominated lipid in distal and proximal leaflet. The bilayer leaflet proximal to the silicon surface consisted of pure PCb while the distal leaflet consisted of about 50% PCb and 50% POPS. POPS is displaced from the proximal leaflet to the distal bilayer leaflet, presumably due to electrostatic repulsion by the negatively charged silicon surface. Such a behavior has also been observed for POPC bilayers on silicon supports, where a gradient in negatively charged fluorescent label TEXAS RED developed between proximal and distal leaflet at low salt concentration and low Debye screening [23]. Note that for SiO_2 the density of hydroxyl groups, and thus, the negative charge at the surface depends crucially on the cleaning procedure [146]. Here, the amount of hydroxyl groups was maximized by aggressive wet chemical cleaning (see chapter 2.6). Less efficient cleaning procedures or longer storage times after cleaning may result in a reduced number of hydroxyl groups, which may be the origin for some controversy in the literature [23, 22].

To estimate the electrostatic repulsion between the silicon surface and negatively charged lipids, the electrostatic potential of the silicon oxide surface is computed in the following for typical salt concentrations used throughout this thesis. The wet chemical cleaning procedure of the silicon oxide surfaces leads to a high coverage with silanol groups. There are two reactions that occur at the silicon oxide surface. The first, with a pKa of about 3, is a protonation of the silanol groups to cationic groups:

$$\mathrm{SiOH_2^+} \rightleftharpoons \mathrm{SiOH} + \mathrm{H^+}.$$

The second, with a pKa of about 7 is a deprotonation of the silanol groups to anionic groups [147]:

$$\mathrm{SiOH} \rightleftharpoons \mathrm{SiO^-} + \mathrm{H^+}$$

A typical density of silanol groups at the silicon oxide surface is 8 sites/nm^2 [147].

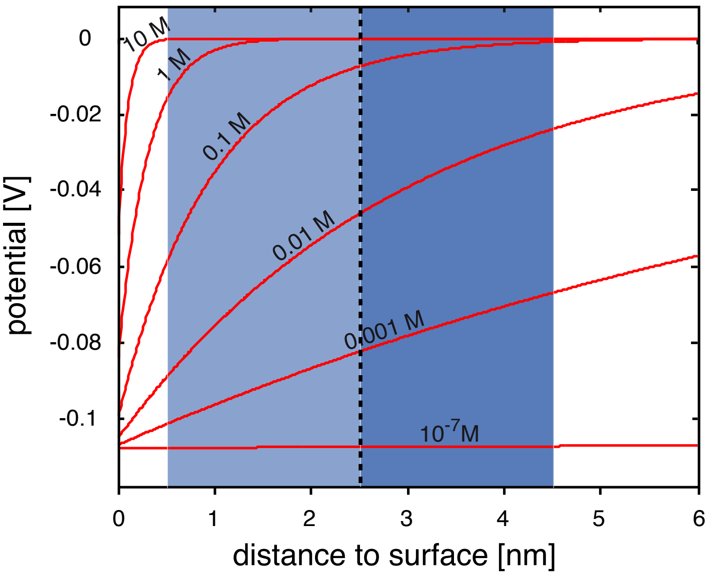

Figure 4.1: Electrostatic potential of a silicon surface as a function of the distance to the surface and electrolyte concentration in a 1:1 electrolyte solution. *Blue area*: area of a bilayer that resides 0.5 nm away from the silicon surface. *Ligth blue area*: area of the proximal bilayer leaflet, *Dark blue area*: area of the distal bilayer leaflet. *Dotted line*: borderline between proximal and distal leaflet.

In this thesis, either pure water or buffer solutions with a pH of 7.4 was used. Duval *et al.* have shown that at a pH of 7.4 about 40 % silanol groups are in the anionic form while the amount of the protonated form is below 5%. Thus, about 3 sites/nm^2 out of 8 sites/nm^2 silanol groups are negatively charged, leading to a charge density of -0.48 C/m^2. In figure 4.1 the electrostatic potential is calculated with equation 2.17 for different NaCl concentrations for surface distances up to 6 nm. As expected, the potential in a 1 M NaCl electrolyte falls of rapidly. At 0.5 nm distance from the surface the electrostatic energy of one POPS lipid is about 15 meV, while at 2 nm distance from the surface (see figure 4.1, *dotted line*) the electrostatic energy is close to zero. With Eq. 2.4, using $z_s = 5$ Å, an area per lipid a_{lipid} of 70 Å^2, a Hamaker constant A_{123} of 4×10^{-21} J [19], and a bilayer thickness $d_b = 40$ Å, the van der Waals energy per lipid between silicon and bilayer is estimated as $E_{VWD}/lipid = 1.9$ meV. Since, for a 25% POPS 75% POPC bilayer there is one negative charge per four lipids, we compare the van der Waals energy of four lipids (7.5 meV) with the electrostatic energy per negatively charged lipid.

In a 1 M NaCl buffer solution, the electrostatic energy at the location of the proximal lipid headgroup, is slightly larger (15 meV at 0.5 nm) than the van der Waals energy (7.5 meV). However, for the distal leaflet, the attractive van der Waals energy becomes the dominant energy. The coverage of intact but stably attached negatively charged vesicles may thus be explained by the interplay of an attractive van der Waals and repulsive electrostatic energy. However, a difference in electrostatic potential of $\simeq$ 15 mV between

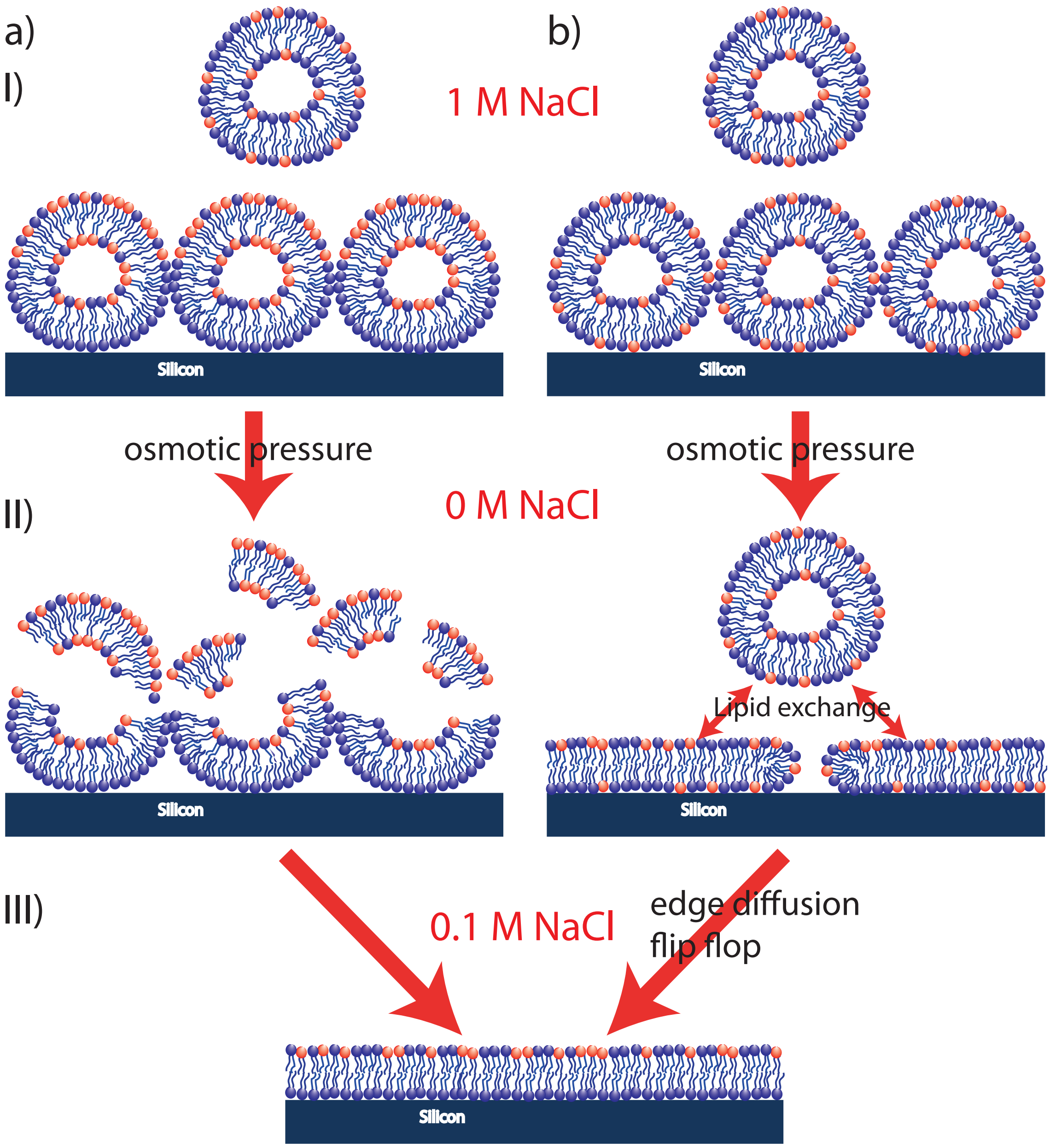

Figure 4.2: Two possible scenarios for the redistribution of negatively charged POPS lipids (*red lipid headgroups*) during vesicle spreading: (*a*) negatively charged lipids accumulate in the upper part of the vesicles (*I*), the upper part is split off during the process of spreading (*a, II*)) and an asymmetric bilayer forms (*III*) or (*b*) homogenous bilayer patches form during vesicle spreading (*b, I* and *II*) and an asymmetric bilayer forms via edge diffusion and/or flip flop of POPS lipids to the distal leaflet (*III*).

both bilayer leaflets may still lead to a redistribution of PS lipids to the upper half of the vesicle as illustrated in figure 4.2*a, I*. During the use of osmotic pressure, the vesicles are exposed to pure water, leading to an opening of the vesicles and a low Debye screening of the negatively charged silicon oxide surface (see figure 4.2, *II*). The latter leads to an accumulation of negatively charged POPS lipids in the water-facing bilayer leaflet, either by splitting of the upper vesicle half (see figure 4.2*a, II*) or by edge diffusion and/or flip flop of POPS lipids to the distal bilayer leaflet in already formed bilayer patches (see figure 4.2*b, II)*). For a NaCl concentrations of 0.1 M, the electrostatic energy due to the potential difference between proximal and distal leaflet is still in the range of $2kT$ (see figure 4.1, *dotted line* and *dark blue area*). Thus, at this concentration, the redistribution of negative lipids to the proximal leaflet is inhibited, by the electrical potential of the substrate. In buffers with NaCl concentrations $\geq$ 0.1 M, van der Waals and electrostatic energy (see figure 4.1) are in the same range, at distances of the distal bilayer leaflet. Since negatively charged lipids reside in the distal bilayer leaflet, the bilayers are stabilized at the silicon surface in buffers with this NaCl concentration.

In the light of low shielding of the negatively charged surface in pure water, it is astonishing that negatively charged bilayers form at all. Apparently, the hydrophobic force between the hydrocarbon chains leads to a strong coherence of the bilayer patches, so that a delamination of charged lipids is diminished. Furthermore, the reallocation of ions to the buffer solution is time dependent and thus some ions may still reside between bilayer and silicon oxide surface stabilizing the bilayer patches. However, a negatively charged bilayer in pure water is a transient situation. Storage of negatively charged bilayers in pure water lead to a delamination of the bilayer from the silicon substrate over time.

4.2 Influence of calcium on the structure of bilayers

In response to calcium buffer, all POPS containing bilayers exhibited a decrease in lipid area of the buffer-facing leaflet as compared to bilayers in water. Strikingly, the lipid area of the substrate facing leaflets remained unaffected and is close to values known for uncharged bilayers. Furthermore, both leaflets of the pure PCb bilayer do not change their lipid area upon adding calcium. Thus, in all measurements containing POPS the distal, buffer-facing leaflets display a pronounced response to the presence of calcium-containing buffer.

Based on these findings, it is proposed that the response of the buffer-facing leaflet to Ca^{2+} results from a chelating effect of calcium ions. Indeed, a chelating effect of calcium ions bridging anionic lipids has been reported before [110, 132]; in the distal leaflet Ca^{2+} bridges at least two POPS molecules and thus results in a closer packing density. In contrast, in the proximal leaflet, POPS is depleted by electrostatics (see section 4.1) and thus the density of the proximal bilayer leaflet is not effected by the addition of calcium.

To directly prove the assymmetric distribution of POPS in negatively charged bilayers the electron density profile of a 75% PCb 25% POPS containing bilayer in calcium buffer was decomposed in its chemical compounds (see figure 3.13*b*). Again, the decomposition revealed an enrichment of POPS in the distal leaflet while the proximal leaflet consisted of pure PCb. All POPS The new method of vesicle spreading with osmotic pressure lead to asymmetric negatively charged bilayers with a high amount of POPS in the distal bilayer leaflet. This asymmetry resembles native cell membranes where the bilayer leaflet facing the cell's interior is enriched in negative lipids. The method provides thus a simple, variable platform to test the behavior of native proteins and bilayer compounds.

4.3 Arrangement of Annexin II Tetramer

The arrangement of the Anx A2t complex upon binding to single surface supported bilayers and the accompanied structural and dynamical changes in the lipid membranes were investigated. The thicknesses of the Anx A2t layer obtained from x-ray measurements were about 6 nm in all cases. The obtained protein thickness was confirmed by neutron reflectivity of a protonated 25% POPS containing bilayer. Higher coverage of the bilayer with Anx A2t did not lead to a change in protein layer thickness, i.e. the arrangement of Anx A2t is independent of protein coverage. In contrast, the binding of Anx A2 monomer lead to a thickness of the protein layer of about 3 nm, which is slightly larger than thicknesses obtained by AFM measurements [69]. However, during AFM measurements a certain force is exerted on the soft protein layer which may lead to a lower apparent protein thickness. All measurements indicate that Anx A2t does not bind in the vertical configuration to a single membrane, as it would result in a significantly larger protein thickness [79, 80]. Instead, the obtained results favor the side-by-side configuration of the Anx A2 tetramer and thus, provide a non-invasive and independent verification of previous AFM studies, [69] (see figure 4.3 for a summarizing illustration). Furthermore, neutron reflectivity studies revealed that the protein is an S-type protein (see section 2.3.1), as it does not penetrate the bilayers headgroup region but resides on top of the bilayer.

Binding of Anx A2t to single membranes in a side-by-side configuration has potential implications for the route of Anx A2t-induced membrane bridging. On the one hand it seems plausible that tetramers in the side-by-side configuration perform some kind of "breathing modes", in which one of the two Annexin monomers temporarily detaches from its membrane interface and is free to bind to an approaching bilayer. As a result, the membrane-membrane contact would be established by Anx A2t in a vertical configuration (figure 2.9 *b, bottom*), in line with cryo-electron microscopy results on Anx A2t-connecting vesicles [79]. However, this mode of membrane-bridging demands a high flexibility of the Anx A2t complex. Indeed, Illien *et al.* have found three different conformations of the tetrameric complex depending on the absence or presence of calcium [148]. Even though the above described work reveals a high flexibility of Annexin II's tetrameric complex it is currently unknown whether the Anx A2 tetramer is indeed able to fluctuate between vertical and side-by-side configuration. Alternatively, it was suggested that the membrane-membrane contact is mediated by the formation of a heterooctameric structure composed of two opposing Anx A2t complexes (figure 2.9*b, top*). This molecular arrangement was favored by Waisman in the case of Anx A2t-chromaffin granules interactions [149] and

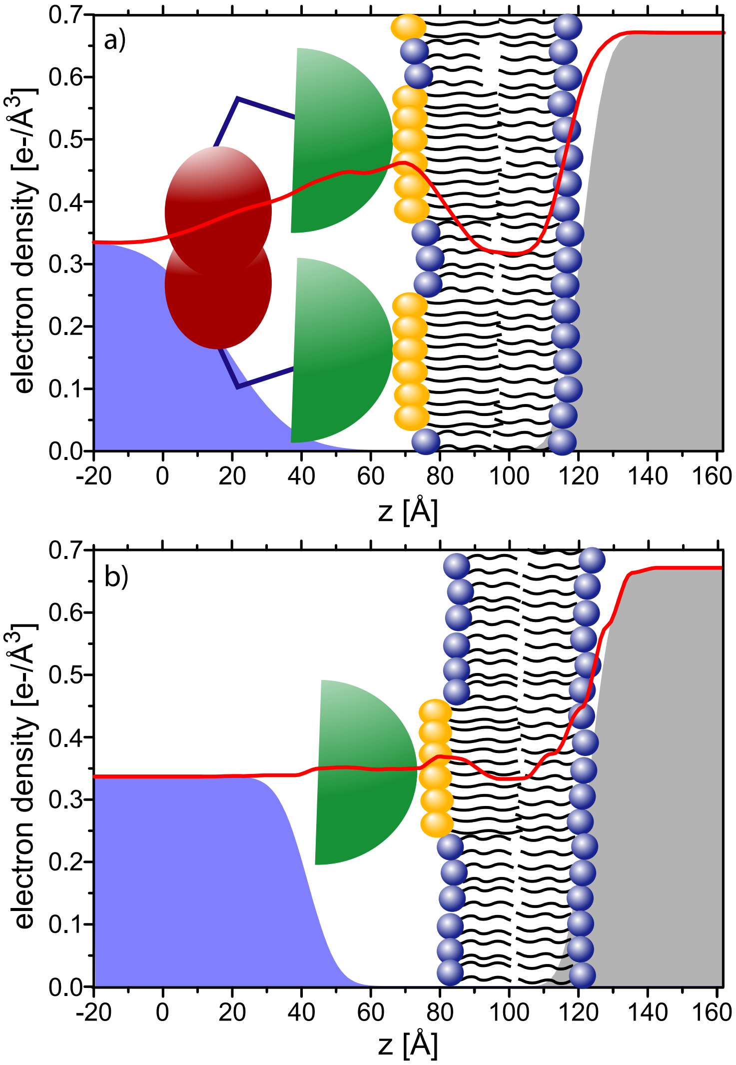

Figure 4.3: Proposed quarternary structure of Anx A2t (*a*) and Anx A2 monomer (*b*) upon binding to a supported lipid bilayer. In both cases Anx A2 monomer (*half spheres*) binds to the distal leaflet of the membrane while for Anx A2t, the p11 dimer (*ellipsoids*) sits on top of this structure. The presence of calcium ions and Anx A2t or Anx A2 monomer leads to a densification of the protein-facing leaflet of the bilayer, due to an enrichment of POPS as compared to POPC.

has also been discussed to occur following disulfide-bridge formation between cysteines within the C-terminal region of p11 [77]. In this model the dynamics of octamer-formation could take two alternative routes: either the octamers pre-assemble on a single membrane interface and thus directly allow bridging to a second membrane, or the Anx A2t tetramers distribute among both membrane interfaces and form octamers only upon membrane-membrane contact. From XR experiments performed in this thesis the thickness of the protein layer on a single SLB is only compatible with a monolayer of Anx A2t, suggesting that a pre-assembly of octamers on a single membrane interface is not significant under the experimental conditions used here.

4.4 Influence of Annexin II Tetramer binding on bilayer structure

Binding of the protein Anx A2t lead to a further densification of the bilayers' distal leaflet in all mixtures of POPC and POPS, while the proximal leaflets were not affected within error. Thus, the response of the leaflets is decoupled. Furthermore, binding of the protein slightly increased the bilayer thickness in the case of the 25% POPS 75% POPC and 50% POPS 50% POPC containing bilayers (see table 3.4). Apparently, the lipids change their conformation to a more stretched conformation during Anx A2t binding. However, the 75% PCb containing bilayer did not show a further densification of the distal leaflet and no change in bilayer thickness. This may be either attributed to a low protein coverage, or to a distortion in lipid packing due to the attached bromine label. All PCb lipid containing bilayers possessed a higher lipid area compared with their unlabeled counterparts in the investigated buffer conditions. It is known that a higher lipid area, leads to less organized lipid alkyl chains [130]. The large bromine label may thus distort the lipid packing and change the lipid chain organization to a less stretched out conformation.

Langmuir compression experiments with DMPA suggested a phase transition between liquid expanded to liquid condensed phase at a packing density of 40 Å^2/lipid, [150] similar to the densities found for the buffer-facing leaflet of the 50% POPS containing bilayer. Likewise, Watkins *et al.* have reported a similar packing density for DPPC SLBs, [151] in agreement with gel phase data. Hence, it is tempting to speculate that the Anx A2t-mediated densification of the bilayer is accompanied with a transition to gel phase in the distal leaflet. Indeed, asymmetric phase transitions in only a single leaflet of the bilayer have been observed before, e.g., in dilauroylphosphatidylcholine/distearoylphosphatidylcholine (DLPC/DSPC) mixtures [152], and thus a phase transition to gel phase in the distal leaflet only, may indeed occur during Anx A2t binding.

XR of a mixture of PCb and POPS revealed an asymmetric distribution of POPS in the distal as compared to the proximal bilayer leaflet, after Anx A2t incubation. The attached bromine label lead to a higher lipid area in all bilayers and a change in phase behavior as compared to unlabeled lipids. Nevertheless, the use of brominated PC derivatives is an effective approach to resolve an asymmetric lipid distribution, providing complementary information to neutron scattering techniques.

4.5 Changes in diffusion constant

Continuous bleaching measurements show a reduced diffusion constant of $D = 2.3 \pm 1$ $\mu m^2/s$ for POPS containing SLBs in calcium containing buffer compared to $D = 4.2 \pm 1.4$ $\mu m^2/s$ for pure POPC SLBs. This decrease in diffusion constant could be accounted to obstructed diffusion, in which calcium ions induce lipid domains of higher packing density and thereby form obstacles for the diffusion of fluorescently labeled lipids [31, 153]. XR revealed an enrichment of the distal leaflet with POPS and a densification in calcium buffer. These structural changes suggest that the formation of calcium-induced POPS domains in the distal leaflet could indeed be the origin of the reduced lipid mobility. Obstructed diffusion in phase separated SLBs has been studied before, and a reduction of the diffusivity by 50% was observed for an area fraction of the gel phase of 0.4 [31]. Hence, due to a higher lipid density in the 50% POPS containing bilayer one would expect that a higher POPS content leads to a lower diffusion constant. However, such a reduction was not resolved within experimental error. Interestingly, Gilmanshin *et al.* have observed a similar behavior for mixtures of POPC and anionic POPG [154]. The diffusion constant was not dependent on the POPC concentration between values of 0 and 80 mol% in calcium containing buffer, whereas it slightly rose with higher POPC amount [154]. Thus, measurements performed in this thesis show a similar behavior for mixtures of POPS and POPC.

Upon Anx A2t incubation, the diffusion constant of both POPS containing SLBs was significantly reduced to 0.9 ± 0.5 $\mu m^2/s$ (25 mol% POPS) and 0.7 ± 0.2 $\mu m^2/s$ (50 mol% POPS). Hence, both anionic bilayers exhibit the same reduction within the error bars, while the POPC control sample displays no decrease in mobility after protein incubation. FRAP measurements with surface supported POPC/POPG membranes also revealed a decrease in diffusion constant upon binding of Annexin IV [154] and the diffusion constant decreased with increasing POPG fraction. However, above a threshold of 50 mol% POPG no further reduction of the mobility was observed. From measurements in this work it seems as if in POPC/POPS mixtures after Anx A2t binding this threshold appears at slightly lower amount of anionic POPS. Yet, from the obtained data it cannot be excluded that there is still a modest dependency of the diffusion constant within the experimental errors.

Lipid demixing upon protein binding to multicomponent membranes has been discussed before in the context of oppositely charged lipid-protein pairs [155, 68]. Menke *et al.* have shown by AFM measurements that an area of POPS depletion develops around Anx A2t. This suggests that obstructed diffusion by phase separation could also be the origin for the reduction of diffusion in presence of Anx A2t, presumably due to POPS assembly underneath the protein [15]. It was speculated that Anx A2t may act directly to trap and cluster PS, thereby creating microdomains in the plasma membrane [28]. The XR data in this work revealed that the protein is not only able to accumulate POPS, but to further compact the bilayer, leading to an increase in bilayer thickness due to the formation of gel-like domains. Hence, the formation of large compact POPS domains below Anx A2t could explain the drastic change in diffusion constant upon Anx A2t binding.

These observations might have important consequences for the understanding of the physiological processes induced by membrane-associated Anx A2t. It was proposed that domain formation may act as nucleation site for lipid rafts and promote their clustering. Once domains are formed, raft structures and the associated cholesterol may further stabilize the lipid-Annexin II interaction *in vivo*, resulting in Annexin II-membrane scaffolds that are required to assemble components of the exocytotic machinery.[28]. However, the role of Anx A2t in this mechanism remained unclear. In addition, it was proposed that Anx A2t creates pores through a densification of the bilayer and thereby facilitates membrane fusion [27]. In this thesis, it was for the first time demonstrated that Anx A2t is indeed able to induce a densification of POPS-containing bilayers *in vitro* and, in addition, resolved that primarily the protein-facing leaflet is condensed. It is tempting to speculate that this asymmetry might be involved in the mechanism of Anx A2t-mediated endo- and exocytosis. The asymmetric insertion of lipids into the outer monolayer of lipid vesicles is often accompanied by positive-curvature strain [156]. In fact, Monte Carlo simulations showed that phase separation in asymmetric bilayers leads to spontaneous budding of the membrane [157]. In the future it will be interesting to use off-specular neutron scattering techniques for a complementary study of Anx A2t-induced membrane reorganization. For instance, deuterated POPS could be employed to enhance the contrast with respect to POPC and thus, to monitor protein-induced lipid segregation and clustering in the two leaflets.

Bibliography

[1] D. Voet, J. G. Voet, and Pratt C. W. *Fundamentals of Biochemistry.* John Wiley & Sons, Inc., 1999.

[2] K. Jacobson, E. D. Sheets, and R. Simson. Revisiting the fluid mosaic model of membranes. *Science*, 268:1441–1442, 1995.

[3] A. Kusumi, Y. Sako, and M. Yamamato. Confined lateral diffusion of membrane-receptors as studied by single-particle tracking (nanovid microscopy) - effects of calcium-induced differentiation in cultured epithelial-cells. *Biophysical Journal*, 65:2021–2040, 1993.

[4] B. C. Lagerholm, G. E. Weinreb, K. Jacobson, and N. L. Thompson. Detecting microdomains in intact cell membranes. *Annual Review of Physical Chemistry*, 56:309–336, 2005.

[5] H. Murakoshi, R. Iino, T. Kobayashi, T. Fujiwara, C. Ohshima, A. Yoshimura, and A. Kusumi. Single-molecule imaging analysis of Ras activation in living cells. *Proceedings of the National Academy of Sciences of the United States of America*, 101:7317–7322, 2004.

[6] G. P. Gorbenko, V. M. Trusova, J. G. Molotkovsky, and P. K. J. Kinnunen. Cytochrome C induces lipid demixing in weakly charged phosphatidylcholine/phosphatidylglycerol model membranes as evidenced by resonance energy transfer. *Biochimica et Biophysica Acta - Biomembranes*, 1788:1358–1365, 2009.

[7] M. A. Carbone and P. M. Macdonald. Cardiotoxin II segregates phosphatidylglycerol from mixtures with phosphatidylcholine: P-31 and H-2 NMR spectroscopic evidence. *Biochemistry*, 35:3368–3378, 1996.

[8] S. Faiss, K. Kastl, A. Janshoff, and C. Steinem. Formation of irreversibly bound annexin Al protein domains on POPC/POPS solid supported membranes. *Biochimica et Biophysica Acta - Biomembranes*, 1778:1601–1610, 2008.

[9] K. Vats, K. Knutson, A. Hinderliter, and E. D. Sheets. Peripheral protein organization and its influence on lipid diffusion in biomimetic membranes. *ACS Chemical Biology*, 5:393–403, 2010.

[10] G. Denisov, S. Wanaski, P. Luan, M. Glaser, and S. McLaughlin. Binding of basic peptides to membranes produces lateral domains enriched in the acidic lipids phosphatidylserine and phosphatidylinositol 4,5-bisphosphate: An electrostatic model and experimental results. *Biophysical Journal*, 74:731–744, 1998.

[11] D. M. Engelman. Membranes are more mosaic than fluid. *Nature*, 438:578–580, 2005.

[12] M. Kranenburg and B. Smit. Phase behavior of model lipid bilayers. *Journal of Physical Chemistry B*, 109:6553–6563, 2005.

[13] A. J. Garcia-Saez and P. Schwille. Surface analysis of membrane dynamics. *Biochimica et Biophysica Acta - Biomembranes*, 1798:766–776, 2010.

[14] R. Koynova and M. Caffrey. Phases and phase transitions of the phosphatidylcholines. *Biochimica et Biophysica Acta - Reviews on Biomembranes*, 1376:91–145, 1998.

[15] M. Menke, V. Gerke, and C. Steinem. Phosphatidylserine membrane domain clustering induced by annexin A2/S100A10 heterotetramer. *Biochemistry*, 44:15296–15303, 2005.

[16] M. Loose and P. Schwille. Biomimetic membrane systems to study cellular organization. *Journal of Structural Biology*, 168:143–151, 2009.

[17] P. Lenz, C. M. Ajo-Franklin, and S. G. Boxer. Patterned supported lipid bilayers and monolayers on poly(dimethylsiloxane). *Langmuir*, 20:11092–11099, 2004.

[18] P. S. Cremer and S. G. Boxer. Formation and spreading of lipid bilayers on planar glass supports. *Journal of Physical Chemistry B*, 103:2554–2559, 1999.

[19] T. H. Anderson, Y. Min, K. L. Weirich, H. Zeng, D. Fygenson, and J. N. Israelachvili. Formation of supported bilayers on silica substrates. *Langmuir*, 25:6997–7005, 2009.

[20] F. F. Rossetti, M. Textor, and I. Reviakine. Asymmetric distribution of phosphatidyl serine in supported phospholipid bilayers on titanium dioxide. *Langmuir*, 22:3467–3473, 2006.

[21] T. R. Khan, H. M. Grandin, A. Mashaghi, M. Textor, E. Reimhult, and I. Reviakine. Lipid redistribution in phosphatidylserine-containing vesicles adsorbing on titania. *Biointerphases*, 3:FA90–FA95, 2008.

[22] R. P. Richter, N. Maury, and A. R. Brisson. On the effect of the solid support on the interleaflet distribution of lipids in supported lipid bilayers. *Langmuir*, 21:299–304, 2005.

[23] A. P. Shreve, M. C. Howland, A. R. Sapuri-Butti, T. W. Allen, and A. N. Parikh. Evidence for leaflet-dependent redistribution of charged molecules in fluid supported phospholipid bilayers. *Langmuir*, 24:13250–13253, 2008.

[24] R. P. Richter, R. Berat, and A. R. Brisson. Formation of solid-supported lipid bilayers: An integrated view. *Langmuir*, 22:3497–3505, 2006.

[25] K. J. Seu, A. P. Pandey, F. Haque, E. A. Proctor, A. E. Ribbe, and J. S. Hovis. Effect of surface treatment on diffusion and domain formation in supported lipid bilayers. *Biophysical Journal*, 92:2445–2450, 2007.

[26] M. R. Horton, C. Reich, A. P. Gast, J. O. Rädler, and B. Nickel. Structure and dynamics of crystalline protein layers bound to supported lipid bilayers. *Langmuir*, 23:6263–6269, 2007.

[27] A. V. Faure, C. Migne, G. Devilliers, and J. Ayala-Sanmartin. Annexin 2 "secretion" accompanying exocytosis of chromaffin cells: Possible mechanisms of annexin release. *Experimental Cell Research*, 276:79–89, 2002.

[28] S. Chasserot-Golaz, N. Vitale, E. Umbrecht-Jenck, D. Knight, V. Gerke, and M. F. Bader. Annexin 2 promotes the formation of lipid microdomains required for calcium-regulated exocytosis of dense-core vesicles. *Molecular Biology of the Cell*, 16:1108–1119, 2005.

[29] K. Monastyrskaya, E. B. Babiychuk, and A. Draeger. The annexins: spatial and temporal coordination of signaling events during cellular stress. *Cellular and Moelcular Life Sciences*, 66:2623–2642, 2009.

[30] L. Fatimathas and S. E. Moss. Annexins as disease modifiers. *Histology and Histopathology*, 25:527–532, 2010.

[31] T. V. Ratto and M. L. Longo. Obstructed diffusion in phase-separated supported lipid bilayers: A combined atomic force microscopy and fluorescence recovery after photobleaching approach. *Biophysical Journal*, 83:3380–3392, 2002.

[32] W. K. Subczynski and A. Kusumi. Dynamics of raft molecules in the cell and artificial membranes: approaches by pulse EPR spin labeling and single molecule optical microscopy. *Biochimica et Biophysica Acta - Biomembranes*, 1610:231–243, 2003.

[33] J. N. Israelachvili. *Intermolecular and Surface Forces with Applications to Colloidal and Biological Systems.* Academic Press, London, 1985.

[34] R. P. Rand. Interacting phospholipid-bilayers - measured forces and induced structural-changes. *Annual Review of Biophysics and Bioengineering*, 10:277–314, 1981.

[35] J. Y. Walz and E. Ruckenstein. Comparison of the van der Waals and undulation interactions between uncharged lipid bilayers. *Journal of Physical Chemistry B*, 103:7461–7468, 1999.

[36] D. Leckband and J. Israelachvili. Intermolecular forces in biology. *Quarterly Reviews of Biophysics*, 34:105–267, 2001.

[37] J. N. Israelachvili. *Intermolecular and Surface Forces.* 2nd edn, Academic Press, London, 1991.

[38] M. Kasbauer, M. Junglas, and T. M. Bayerl. Effect of cationic lipids in the formation of asymmetries in supported bilayers. *Biophysical Journal*, 76:2600–2605, 1999.

[39] B. C. Donose, I. U. Vakarelski, E. Taran, H. Shinto, and K. Higashitani. Specific effects of divalent cation nitrates on the nanotribology of silica surfaces. *Industrial & Engineering Chemistry Research*, 45:7035–7041, 2006.

[40] M. L. Fielden, R. A. Hayes, and J. Ralston. Oscillatory and ion-correlation forces observed in direct force measurements between silica surfaces in concentrated $CaCl_2$ solutions. *Physical Chemistry Chemical Physics*, 2:2623–2628, 2000.

[41] A. Grabbe and R. G. Horn. Double-layer and hydration forces measured between silica sheets subjected to various surface treatments. *Journal of Colloid and Interface Science*, 157:375 – 383, 1993.

[42] J. Faraudo and F. Bresme. Origin of the short-range, strong repulsive force between ionic surfactant layers. *Physical Review Letters*, 94, 2005.

[43] J. P. Chapel. Electrolyte species-dependent hydration forces between silica surfaces. *Langmuir*, 10:4237–4243, 1994.

[44] R. Podgornik, D. C. Rau, and V. A. Parsegian. The action of interhelical forces on the organization of DNA double helices - fluctuation-enhanced decay of electrostatic double-layer and hydration forces. *Macromolecules*, 22:1780–1786, 1989.

[45] S. Leikin, V. A. Parsegian, D. C. Rau, and R. P. Rand. Hydration forces. *Annual Review of Physical Chemistry*, 44:369–395, 1993.

[46] S. Lequien, L. Goirand, and F. Lesimple. Design of the anomalous scattering beamline at the european synchrotron-radiation facility. *Review of Scientific Instruments*, 66:1725–1727, 1995.

[47] R. P. Rand and V. A. Parsegian. Hydration forces between phospholipid-bilayers. *Biochimica et Biophysica Acta*, 988:351–376, 1989.

[48] S. A. Tatulian, V. I. Gordeliy, A. E. Sokolova, and A. G. Syrykh. A neutron-diffraction study of the influence of ions on phospholipid membrane interactions. *Biochimica et Biophysica Acta*, 1070:143–151, 1991.

[49] M. Dishon, O. Zohar, and U. Sivan. From repulsion to attraction and back to repulsion: The effect of NaCl, KCl, and CsCl on the force between silica surfaces in aqueous solution. *Langmuir*, 25:2831–2836, 2009.

[50] D.C. Rau and V.A. Parsegian. Direct measurement of the intermolecular forces between counterion-condensed DNA double helices. Evidence for long range attractive hydration forces. *Biophysical Journal*, 61:246 – 259, 1992.

[51] N. A. M. Besseling. Theory of hydration forces between surfaces. *Langmuir*, 13:2113–2122, 1997.

[52] R. P. Rand, N. Fuller, V. A. Parsegian, and D. C. Rau. Variation in hydration forces between neutral phospholipid-bilayers - evidence for hydration attraction. *Biochemistry*, 27:7711–7722, 1988.

[53] H. Hauser and G. G. Shipley. Interactions of divalent-cations with phosphatidylserine bilayer-membranes. *Biochemistry*, 23:34–41, 1984.

[54] G. W. Feigenson. Calcium-ion binding between lipid bilayers - the 4-component system of phosphatidylserine, phosphatidylcholine, calcium-chloride, and water. *Biochemistry*, 28:1270–1278, 1989.

[55] S. J. Singer and G. L. Nicolson. Fluid mosaic model of structure of cell-membranes. *Science*, 175:720–&, 1972.

[56] S. Semrau and T. Schmidt. Membrane heterogeneity - from lipid domains to curvature effects. *Soft Matter*, 5:3174–3186, 2009.

[57] S. May. Stability of macroion-decorated lipid membranes. *Journal of Physics - Condensed Matter*, 17:R833–R850, 2005.

[58] K. Kastl, M. Menke, E. Luthgens, S. Faiss, V. Gerke, A. Janshoff, and C. Steinem. Partially reversible adsorption of annexin A1 on POPC/POPS bilayers investigated by QCM measurements, SFM, and DMC simulations. *ChemBioChem*, 7:106–115, 2006.

[59] P. I. Kuzmin, S. A. Akimov, Y. A. Chizmadzhev, J. Zimmerberg, and F. S. Cohen. Line tension and interaction energies of membrane rafts calculated from lipid splay and tilt. *Biophysical Journal*, 88:1120–1133, 2005.

[60] E. L. Elson, E. Fried, J. E. Dolbow, and G. M. Genin. Phase separation in biological membranes: Integration of theory and experiment. In *Annual Review of Biophysics, Vol. 39*, pages 207–226. 2010.

[61] T. S. Ursell, W. S. Klug, and R. Phillips. Morphology and interaction between lipid domains. *Proceedings of the National Academy of Sciences of the United States of America*, 106:13301–13306, 2009.

[62] W. H. Cho and R. V. Stahelin. Membrane-protein interactions in cell signaling and membrane trafficking. *Annual Review of Biophysics and Biomolecular Structure*, 34:119–151, 2005.

[63] V. Gerke, C. E. Creutz, and S. E. Moss. Annexins: Linking Ca_2^+ signalling to membrane dynamics. *Nature Reviews Molecular Cell Biology*, 6:449–461, 2005.

[64] A. Mulgrew-Nesbitt, K. Diraviyam, J. Wang, S. Singh, P. Murray, Z. Li, L. Rogers, N. Mirkovic, and D. Murray. The role of electrostatics in protein-membrane interactions. *Biochimica et Biophysica Acta - Molecular and Cell Biology of Lipids*, 1761:812–826, 2006.

[65] J. Fan, M. Sammalkorpi, and M. Haataja. Formation and regulation of lipid microdomains in cell membranes: Theory, modeling, and speculation. *FEBS Letters*, 584:1678–1684, 2010.

[66] L. G. Magal, Y. Yaffe, J. Shepshelovich, F. J. Aranda, M. del Carmen de Marco, K. Gaus, A. M. Alonso, and K. Hirschberg. Clustering and lateral concentration of raft lipids by the MAL protein. *Molecular Biology of the Cell*, 20:3751–3762, 2009.

[67] L. J. Pike. Rafts defined: a report on the keystone symposium on lipid rafts and cell function. *Journal of Lipid Research*, 47:1597–1598, 2006.

[68] S. May, D. Harries, and A. Ben-Shaul. Lipid demixing and protein-protein interactions in the adsorption of charged proteins on mixed membranes. *Biophysical Journal*, 79:1747–1760, 2000.

[69] M. Menke, M. Ross, V. Gerke, and C. Steinem. The molecular arrangement of membrane-bound annexin A2-S100A10 tetramer as revealed by scanning force microscopy. *ChemBioChem*, 5:1003–1006, 2004.

[70] M. A. Swairjo, N. O. Concha, M. A Kaetzel, J. R. Dedman, and B. A. Seaton. Ca^{2+}-bridging mechanism and phospholipid head group recognition in the membrane-binding protein annexin V. *Nature Structural Biology*, 2:968–974, 1995.

[71] PDB ID: 2H0K
A. Brisson, A. T. Granier, B. Langlois D'Estaintot, B. Gallois, B. Tessier. Identification of the residues involved in the formation of annexin V trimers within 2D and 3D Crystals.

[72] M. Jost, K. Weber, and V. Gerke. Annexin II contains two types of Ca^{2+}-binding sites. *Biochemical Journal*, 298:553–559, 1994.

[73] S. Réty, J. Sopkova, M. Renourd, S. Tabares, D. Osterloh, V. Gerke, F. Russo-Marie, and A. Lewit-Bentley. A crystal structure of a complex of p11 with the annexin II N-terminal peptide. *Nature Structural Biology*, 6:89–95, 1999.

[74] A. Burger, R. Berendes, S. Liemann, J. Benz, A. Hofmann, P. Göttig, R. Huber, V. Gerke, C. Thiel, J. Römisch, and K. Weber. The crystal structure and ion channel activity of human annexin II, a peripheral membrane protein. *Journal of Molecular Biology*, 257:839–847, 1996.

[75] A. Rosengarth and H. Luecke. Annexin A2 - does it induce membrane aggregation by a new multimeric state of the protein? *Annexins*, 1:129–136, 2004.

[76] J. Sopkova-de Oliveira Santos, F. K. Oling, S. Réty, A. Brisson, J. C. Smith, and A. Lewit-Bentley. S100 protein-annexin interactions: a model of the $(\mathrm{Anx2} - \mathrm{p11})_2$ heterotetramer complex. *Biochimica et Biophysica Acta - Molecular Cell Research*, 1498:181 – 191, 2000.

[77] A. Lewit-Bentley, S. Réty, J. Sopkova-de Oliveira Santos, and V. Gerke. S100-annexin complexes: Some insights from structural studies. *Cell Biology International*, 24:799–802, 2000.

[78] D. M. Schulz, S. Kalkhof, A. Schmidt, C. Ihling, C. Stingl, K. Mechtler, O. Zschoernig, and A. Sinz. Annexin A2/P11 interaction: New insights into annexin A2 tetramer structure by chemical crosslinking, high-resolution mass spectrometry, and computational modeling. *Proteins - Structure and Function and Bioinformatics*, 69:254–269, 2007.

[79] O. Lambert, V. Gerke, M. F. Bader, F. Porte, and A. Brisson. Structural analysis of junctions formed between lipid membranes and several annexins by cryo-electron microscopy. *Journal of Molecular Biology*, 272:42–55, 1997.

[80] T. Nakata, K. Sobue, and N. Hirokawa. Conformational change and localization of calpactin I complex involved in exocytosis as revealed by quick-freeze, deep-etch electron microscopy and immunocytochemistry. *Journal of Cell Biology*, 110:13–25, 1990.

[81] O. Lambert, N. Cavusoglu, J. Gallay, M. Vincent, J. L. Rigaud, J. P. Henry, and J. Ayala-Sanmartin. Novel organization and properties of annexin 2-membrane complexes. *Journal of Biological Chemistry*, 279:10872–10882, 2004.

[82] W. L. C. Vaz, F. Goodsaidzalduondo, and K. Jacobson. Lateral diffusion of lipids and proteins in bilayer-membranes. *FEBS Letters*, 174:199–207, 1984.

[83] S. Nir and W. D. Stein. 2 modes of diffusion in liquids. *Journal of Chemical Physics*, 55:1598–&, 1971.

[84] R. J. Pace and S. I. Chan. Molecular motions in lipid bilayers. III. Lateral and transverse diffusion in bilayers. *Journal of Chemical Physics*, 76:4241–4247, 1982.

[85] J. E. MacCarthy and J. J. Kozak. Lateral diffusion in fluid systems. *Journal of Chemical Physics*, 77:2214–2216, 1982.

[86] P. F. F. Almeida and W. L. C. Vaz. *Handbook of Biological Physics*, volume 1A, chapter Structure and dynamics of membranes: Lateral diffusion in membranes. Elsevier Science B.V., 1995.

[87] P. F. F. Almeida, W. L. C. Vaz, and T. E. Thompson. Lateral diffusion and percolation in 2-phase, 2-component lipid bilayers - topology of the solid-phase domains inplane and across the lipid bilayer. *Biochemistry*, 31:7198–7210, 1992.

[88] P. F. F. Almeida, W. L. C. Vaz, and T. E. Thompson. Lateral diffusion in the liquid-phases of dimyristoylphosphatidylcholine cholesterol lipid bilayers - a free-volume analysis. *Biochemistry*, 31:6739–6747, 1992.

[89] R. Machan and M. Hof. Lipid diffusion in planar membranes investigated by fluorescence correlation spectroscopy. *Biochimica et Biophysica Acta - Biomembranes*, 1798:1377–1391, 2010.

[90] J. F. Tocanne, L. Dupou-Czanne, A. Lopez, and J. F. Tournier. Lipid lateral diffusion and membrane organization. *FEBS Letters*, 257:10 – 16, 1989.

[91] E. Yechiel and M. Edidin. Micrometer-scale domains in fibroblast plasma-membranes. *Journal of Cell Biology*, 105:755–760, 1987.

[92] Y. Chen, B. C. Lagerholm, B. Yang, and K. Jacobson. Methods to measure the lateral diffusion of membrane lipids and proteins. *Methods*, 39:147 – 153, 2006.

[93] G. Rayan, J. E. Guet, N. Taulier, F. Pincet, and W. Urbach. Recent applications of fluorescence recovery after photobleaching (FRAP) to membrane biomacromolecules. *Sensors*, 10:5927–5948, 2010.

[94] P. Jonsson, M. P. Jonsson, J. O. Tegenfeldt, and F. Hook. A method improving the accuracy of fluorescence recovery after photobleaching analysis. *Biophysical Journal*, 95:5334–5348, 2008.

[95] L. Guo, J. Y. Har, J. Sankaran, Y. Hong, B. Kannan, and T. Wohland. Molecular diffusion measurement in lipid bilayers over wide concentration ranges: A comparative study. *ChemPhysChem*, 9:721–728, 2008.

[96] A. Kusumi, H. Ike, C. Nakada, K. Murase, and T. Fujiwara. Single-molecule tracking of membrane molecules: plasma membrane compartmentalization and dynamic assembly of raft-philic signaling molecules. *Seminars in Immunology*, 17:3–21, 2005.

[97] C. A. Day and A. K. Kenworthy. Tracking microdomain dynamics in cell membranes. *Biochimica et Biophysica Acta - Biomembranes*, 1788:245–253, 2009.

[98] P. Schwille, J. Korlach, and W. W. Webb. Fluorescence correlation spectroscopy with single-molecule sensitivity on cell and model membranes. *Cytometry*, 36:176–182, 1999.

[99] A. J. Garcia-Saez and P. Schwille. Fluorescence correlation spectroscopy for the study of membrane dynamics and protein/lipid interactions. *Methods*, 46:116–122, 2008.

[100] A. Horner, Y. N. Antonenko, and P. Pohl. Coupled diffusion of peripherally bound peptides along the outer and inner membrane leaflets. *Biophysical Journal*, 96:2689–2695, 2009.

[101] R. Machan, A. Miszta, W. Hermens, and M. Hof. Real-time monitoring of melittin-induced pore and tubule formation from supported lipid bilayers and its physiological relevance. *Chemistry and Physics of Lipids*, 163:200–206, 2010.

[102] R. Machan and M. Hof. Recent developments in fluorescence correlation spectroscopy for diffusion measurements in planar lipid membranes. *International Journal of Molecular Sciences*, 11:427–457, 2010.

[103] C. Dietrich, R. Merkel, and R. Tampe. Diffusion measurement of fluorescence-labeled amphiphilic molecules with a standard fluorescence microscope. *Biophysical Journal*, 72:1701–1710, 1997.

[104] H. P. Wacklin and R. K. Thomas. Spontaneous formation of asymmetric lipid bilayers by adsorption of vesicles. *Langmuir*, 23:7644–7651, 2007.

[105] P. Callow, A. Sukhodub, J. E. Taylor, and G. G. Kneale. Shape and subunit organisation of the DNA Methyltransferase M.AhdI by small-angle neutron scattering. *Journal of Molecular Biology*, 369:177–185, 2007.

[106] J. Penfold and Thomas R. K. The application of the specular reflection of neutrons to the study of surfaces and interfaces. *Journal of Physics - Condensed Matter*, 2:1369–1412, 1990.

[107] A Nelson. Co-refinement of multiple-contrast neutron/x-ray reflectivity data using *motofit*. *Journal of Applied Crystallography*, 39:273–276, 2006.

[108] M. Gupta, T. Gutberlet, J. Stahn, P. Keller, and D. Clemens. AMOR - the time-of-flight neutron reflectometer at SINQ/PSI. *Pramana - Journal of Physics*, 63:57–63, 2004.

[109] C. Reich, M. B. Hochrein, B. Krause, and B. Nickel. A microfluidic setup for studies of solid-liquid interfaces using x-ray reflectivity and fluorescence microscopy. *Review of Scientific Instruments*, 76, 2005.

[110] J. Mattai, H. Hauser, R. A. Demel, and G. G. Shipley. Interactions of metal-ions with phosphatidylserine bilayer-membranes - effect of hydrocarbon chain unsaturation. *Biochemistry*, 28:2322–2330, 1989.

[111] C. Reich, M. R. Horton, B. Krause, A. P. Gast, J. O. Rädler, and B. Nickel. Asymmetric structural features in single supported lipid bilayers containing cholesterol and GM1 resolved with synchrotron x-ray reflectivity. *Biophysical Journal*, 95:657–668, 2008.

[112] C. Daniel, K. E. Sohn, T. E. Mates, E. J. Kramer, J. O. Rädler, E. Sackmann, B. Nickel, and L. Andruzzi. Structural characterization of an elevated lipid bilayer obtained by stepwise functionalization of a self-assembled alkenyl silane film. *Biointerphases*, 2:109–118, 2007.

[113] E. Novakova, K. Giewekemeyer, and T. Salditt. Structure of two-component lipid membranes on solid support: An x-ray reflectivity study. *Physical Review E*, 74, 2006.

[114] R. S. Armen, O. D. Uitto, and S. E. Feller. Phospholipid component volumes: Determination and application to bilayer structure calculations. *Biophysical Journal*, 75:734–744, 1998.

[115] T. J. Mcintosh and P. W. Holloway. Determination of the depth of bromine atoms in bilayers formed from bromolipid probes. *Biochemistry*, 26:1783–1788, 1987.

[116] N. Kucerka, S. Tristram-Nagle, and J. F. Nagle. Structure of fully hydrated fluid phase lipid bilayers with monounsaturated chains. *Journal of Membrane Biology*, 208:193–202, 2006.

[117] N. Kucerka, J. F. Nagle, J. N. Sachs, S. E. Feller, J. Pencer, A. Jackson, and J. Katsaras. Lipid bilayer structure determined by the simultaneous analysis of neutron and x-ray scattering data. *Biophysical Journal*, 95:2356–2367, 2008.

[118] G. Fritz, C. Koller, K. Burdack, L. Tetsch, I. Haneburger, K. Jung, and U. Gerland. Induction kinetics of a conditional pH stress response system in *Escherichia coli*. *Jornal of Moelcular Biology*, 393:272–286, 2009.

[119] E. Gasteiger, A. Gattiker, C. Hoogland, I. Ivanyi, R. D. Appel, and A. Bairoch. Expasy: the proteomics server for in-depth protein knowledge and analysis. *Nucleic Acids Research*, 31:3784–3788, 2003.

[120] H. Fischer, I. Polikarpov, and A. F. Craievich. Average protein density is a molecular-weight-dependent function. *Protein Science*, 13:2825–2828, 2004.

[121] D. E. Leckband, C. A. Helm, and J Israelachvili. Role of calcium in the adhesion and fusion of bilayers. *Biochemistry*, 32:1127–1140, 1993.

[122] J. T. Hautala, S. K. Wiedmer, and M. L. Riekkola. Anionic liposomes in capillary electrophoresis: Effect of calcium on 1-palmitoyl-2-oleyl-sn-glycero-3-phosphatidylcholine/phosphatidylserine- coating in silica capillaries. *Analytical and Bioananytical Chemistry*, 378:1769–1776, 2004.

[123] H. Binder and O. Zschornig. The effect of metal cations on the phase behavior and hydration characteristics of phospholipid membranes. *Chemistry and Physics of Lipids*, 115:39–61, 2002.

[124] E. Reimhult, F. Hook, and B. Kasemo. Intact vesicle adsorption and supported biomembrane formation from vesicles in solution: Influence of surface chemistry, vesicle size, temperature, and osmotic pressure. *Langmuir*, 19:1681–1691, 2003.

[125] A. W. Roszak, A. T. Gardiner, N. W. Isaacs, and R. J. Cogdell. Brominated lipids identify lipid binding sites on the surface of the reaction center from Rhodobacter sphaeroides. *Biochemistry*, 46:2909–2916, 2007.

[126] M. Vogel, C. Munster, W. Fenzl, and T. Salditt. Thermal unbinding of highly oriented phospholipid membranes. *Physical Review Letters*, 84:390–393, 2000.

[127] U. Seifert. Dynamics of a bound membrane. *Physical Review E*, 49:3124–3127, 1994.

[128] N. Kucerka, M. Nieh, J. Pencer, T. Harroun, and J. Katsaras. The study of liposomes, lamellae and membranes using neutrons and x-rays. *Current Opinion in Colloid & Interface Science*, 12:17–22, 2007.

[129] J. B. Klauda, N. Kucerka, B. R. Brooks, R. W. Pastor, and J. F. Nagle. Simulation-based methods for interpreting x-ray data from lipid bilayers. *Biophysical Journal*, 90:2796 – 2807, 2006.

[130] K. Hristova and S. H. White. Determination of the hydrocarbon core structure of fluid dioleoylphosphocholine (DOPC) bilayers by x-ray diffraction using specific bromination of the double-bonds: Effect of hydration. *Biophysical Journal*, 74:2419–2433, 1998.

[131] I. Reviakine and A. Brisson. Formation of supported phospholipid bilayers from unilamellar vesicles investigated by atomic force microscopy. *Langmuir*, 16:1806–1815, 2000.

[132] H. L. Casal, A. Martin, H. H. Mantsch, F. Paltauf, and H. Hauser. Infrared studies of fully hydrated unsaturated phosphatidylserine bilayers. effect of Li^+ and Ca_2^+. *Biochemistry*, 26:7395–7401, 1987.

[133] P. T. Vernier, M. J. Ziegler, and R. Dimova. Calcium binding and head group dipole angle in phosphatidylserine-phosphatidylcholine bilayers. *Langmuir*, 25:1020–1027, 2009.

[134] W. H. Press, S. A. Teukolsky, W. T. Vetterling, and B. P. Flannery. *Numerical Recipes in C: The art of scientific computing.* Cambridge University Press, 1992.

[135] S. Ladha, A. R. Mackie, L. J. Harvey, D. C. Clark, E. J. A. Lea, M. Brullemans, and H. Duclohier. Lateral diffusion in planar lipid bilayers: A fluorescence recovery after photobleaching investigation of its modulation by lipid composition, cholesterol, or alamethicin content and divalent cations. *Biophysical Journal*, 71:1364–1373, 1996.

[136] L. F. Zhang and S. Granick. Lipid diffusion compared in outer and inner leaflets of planar supported bilayers. *Journal of Chemical Physics*, 123, 2005.

[137] C. Scomparin, S. Lecuyer, M. Ferreira, T. Charitat, and B. Tinland. Diffusion in supported lipid bilayers: Influence of substrate and preparation technique on the internal dynamics. *European Physical Journal E*, 28:211–220, 2009.

[138] J. R. Howse, E. Manzanares-Papayanopoulos, I. A. McLure, J. Bowers, R. Steitz, and G. H. Findenegg. Critical adsorption and boundary layer structure of 2-butoxyethanol + D_2O mixtures at a hydrophilic silica surface. *The Journal of Chemical Physics*, 116:7177–7188, 2002.

[139] H. P. Wacklin, F. Tiberg, G. Fragneto, and R. K. Thomas. Distribution of reaction products in phospholipase A(2) hydrolysis. *Biochimica et Biophysica Acta - Biomembranes*, 1768:1036–1049, 2007.

[140] T. Gutberlet, R. Steitz, G. Fragneto, and B. Klosgen. Phospholipid bilayer formation at a bare Si surface: A time-resolved neutron reflectivity study. *Journal of Physics - Condensed Matter*, 16:S2469–S2476, 2004.

[141] F. J. Wu, C. R. Flach, B. A. Seaton, T. R. Mealy, and R. Mendelsohn. Stability of annexin Vin ternary complexes with Ca_2^+ and anionic phospholipids: IR studies of monolayer and bulk phases. *Biochemistry*, 38:792–799, 1999.

[142] H. P. Vacklin, F. Tiberg, and R. K. Thomas. Formation of supported phospholipid bilayers via co-adsorption with β-D-dodecyl maltoside. *Biochimica et Biophysica Acta - Biomembranes*, 1668:17–24, 2005.

[143] D. H. Mengistu and S. May. Debye-Hückel theory of mixed charged-zwitterionic lipid layers. *European Physical Journal E*, 26:251–260, 2008.

[144] H. Y. Jing, D. H. Hong, B. D. Kwak, D. J. Choi, K. Shin, C. Y. Yu, J. W. Kim, D. Y. Noh, and Y. S. Seo. X-ray reflectivity study on the structure and phase stability of mixed phospholipid multilayers. *Langmuir*, 25:4198–4202, 2009.

[145] M. C. Wiener and S. H. White. Transbilayer distribution of bromine in fluid bilayers containing a specifically brominated analog of dioleoylphosphatidylcholine. *Biochemistry*, 30:6997–7008, 1991.

[146] R. Tero, H. Watanabe, and T. Urisu. Supported phospholipid bilayer formation on hydrophilicity-controlled silicon dioxide surfaces. *Physical Chemistry Chemical Physics*, 8:3885–3894, 2006.

[147] Y. Duval, J. A. Mielczarski, O. S. Pokrovsky, E. Mielczarski, and J. J. Ehrhardt. Evidence of the existence of three types of species at the quartz-aqueous solution interface at pH 0-10: XPS surface group quantification and surface complexation modeling. *Journal of Physical Chemistry B*, 106:2937–2945, 2002.

[148] F. Illien, S. Finet, O. Lambert, and J. Ayala-Sanmartin. Different molecular arrangements of the tetrameric annexin 2 modulate the size and dynamics of membrane aggregation. *Biochimica et Biophysica Acta - Biomembranes*, 1798:1790–1796, 2010.

[149] D. M. Waisman. Annexin II tetramer: Structure and function. *Molecular and Cellular Biochemistry*, 149:301–322, 1995.

[150] M. Schalke, P. Kruger, M. Weygand, and M. Losche. Submolecular organization of DMPA in surface monolayers: Beyond the two-layer model. *Biochimica et Biophysica Acta - Biomembranes*, 1464:113–126, 2000.

[151] E. B. Watkins, C. E. Miller, D. J. Mulder, T. L. Kuhl, and J. Majewski. Structure and orientational texture of self-organizing lipid bilayers. *Physical Review Letters*, 102, 2009.

[152] W. C. Lin, C. D. Blanchette, T. V. Ratto, and M. L. Longo. Lipid asymmetry in DLPC/DSPC-supported lipid bilayers: A combined AFM and fluorescence microscopy study. *Biophysical Journal*, 90:228–237, 2006.

[153] S. F. Fenz, R. Merkel, and K. Sengupta. Diffusion and intermembrane distance: Case study of avidin and E-cadherin mediated adhesion. *Langmuir*, 25:1074–1085, 2009.

[154] R. Gilmanshin, C. E. Creutz, and L. K. Tamm. Annexin IV reduces the rate of lateral lipid diffusion and changes the fluid phase structure of the lipid bilayer when it binds to negatively charged membranes in the presence of calcium. *Biochemistry*, 33:8225–8232, 1994.

[155] T. Heimburg, B. Angerstein, and D. Marsh. Binding of peripheral proteins to mixed lipid membranes: Effect of lipid demixing upon binding. *Biophysical Journal*, 76:2575–2586, 1999.

[156] S. Esteban-Martin, H. J. Risselada, J. Salgado, and S. J. Marrink. Stability of asymmetric lipid bilayers assessed by molecular dynamics simulations. *Journal of the American Chemical Society*, 131:15194–15202, 2009.

[157] E. J. Wallace, N. M. Hooper, and P. D. Olmsted. The kinetics of phase separation in asymmetric membranes. *Biophysical Journal*, 88:4072–4083, 2005.

Publications

[1] K. Fritz, G. Fritz, B. Windschiegl, C. Steinem and B. Nickel. Arrangement of Annexin A2 tetramer and its impact on the structure and diffusivity of supported lipid bilayers, *Soft Matter*, 6:4084–4094, 2010.

List of Tables

List of Figures

Vielen Dank an ...

Privatdozent Dr. Bert Nickel für das spannende Thema, die experimentelle Freiheit, die gute Betreuung dieser Arbeit, und die vielen Diskussionen über physikalische Fragestellungen, die mich als Ingenieurin immer wieder für das Eintauchen in die "Welt der Physiker" motivierten und begeisterten.

Prof. Dr. Joachim Rädler für den erfolgreichen Kampf um meine Anerkennung als Doktorandin, die prompte Hilfe in scheinbar aussichtslosen Situationen und das angenehme Arbeitsklima am Lehrstuhl.

Prof. Dr. Claudia Steinem für die informativen Diskussionen über Annexin und die gute Zusammenarbeit.

Prof. Erich Sackmann für sein beeindruckendes Wissen der Biophysik, das oft die zündenden Ideen lieferte.

Barbara Windschiegl für die Extraktion des Proteins.

Georg Fritz für das gemeinsame Entwickeln des Continous Bleaching Programmes, die fruchtbare wissenschaftliche Kooperation, die Hilfe bei theoretischen Fragestellungen, das Korrekturlesen, und dafür dass Du mein ruhender Pol und der beste Vater und Ehemann der Welt bist.

Thorsten Neubert für den Bau der Neutronenzelle und das Fräsen der Röntgenkammern.

Dr. Susi Kempter und Gerlinde Schwake für den täglichen Kampf gegen das Chaos im Labor.

Dr. Thomas Gutberlet für eine spannende und erfolgreiche Messzeit am PSI und die wissenschaftlichen Diskussionen über Neutronenmessungen.

Dr. Christian Daniel für kreative Strahlzeiten, den Irrsinn in den durchwachten Nächten am Synchrotron, die eine oder andere Blubberfoliendiskussion, die gemeinsame Bürozeit bei E22, seine Arbeitsweise bei der nie der Spass und die Liebe zur Wissenschaft verloren ging und seine Freundschaft und Unterstützung.

Samira Hertrich und Stefan Stanglmeier für die Unterstützung im Labor während meiner Schwangerschaften, und die entspannte Bürogemeinschaft.

Dr. Martin Huth für entspannte Messzeiten und die gute Zusammenarbeit.

Simon Youssef und Börn Meier für das Lösen von Computerproblemen.

Dr. Madeleine Leisner, Dr. Marion Hochrein, Dr. Judith Megerle und Dr. Hanna Engelke für zahlreiche Mädelsabende und Gespräche über das Leben an sich.

Margarete Meixner für die Organisation des Lehrstuhls.

den gesamten Lehrstuhl Rädler für die nette Arbeitsatmosphäre und die vielen gemeinsamen Kuchenschlachten und Mittagessen.

meine Freunde für Berg, Kletter, Skitour, Surf Abenteuer und Busurlaube und dafür dass man immer auf Euch zählen kann.

Christian von Lübke für das Korrekturlesen.

Winni und Eva Werner für spontane Babysitter Einsätze.

Angelika Fritz und Uwe von Trotha für die liebevolle Unterstützung in allen Lebenslagen.

meine Eltern, die mich zu dem gemacht haben was ich bin, dass sie immer an mich geglaubt haben und sie immer für mich da sind.

meine Oma, die mich durch Ihre Neugier und Ihrem Drang den Dingen auf den Grund zu gehen zum Forschen inspiriert.